Computational Evaluation of Aerodynamic Performance of Isuzu Midi Bus Body

By

Natnael Bekele Kidane

A Thesis Submitted to

Mechanical System and Vehicle Engineering Program

School of Mechanical, Chemical and Materials Engineering

Presented in partial fulfillment of the requirement for the degree of

Master of Science in Automotive Engineering

Office of Graduate Studies

Adama Science and Technology University

Adama, Ethiopia

September 2019

Computational Evaluation of Aerodynamic Performance of Isuzu Midi Bus Body

By

Natnael Bekele Kidane

Advisor: Dr. Gezahegn Habtamu

A Thesis Submitted to

Mechanical System and Vehicle Engineering Program

School of Mechanical, Chemical and Materials Engineering

Presented in partial fulfillment of the requirement for the degree of

Master of Science in Automotive Engineering

Office of Graduate Studies

Adama Science and Technology University

Adama, Ethiopia

September 2019

APPROVAL OF BOARD OF EXAMINERS

We, the undersigned, members of the Board of Examiners of the final open defense by Natnael Bekele Kidane have read and evaluated his thesis entitled “Computational Evaluation of Aerodynamic Performance of Isuzu Midi Bus Body” and examined the candidate. This is, therefore, to certify that the thesis has been accepted in partial fulfillment of the requirement of the Degree of Master of Science in Automotive Engineering.

______________________________	____________________	________________
Chairperson	Signature	Date
______________________________	____________________	________________
Internal Examiner	Signature	Date
______________________________	____________________	________________
External Examiner	Signature	Date

CANDIDATE’S DECLARATION

I hereby declare that this MSc Thesis is my original work and has not been presented for a degree in any other university, and all sources of material used for this thesis have been duly acknowledged.

Name: Natnael Bekele Kidane

Signature: ____________

This MSc Thesis has been submitted for examination with my approval as a thesis Advisor.

Name: Dr. Gezahegn Habtamu

Signature: ____________

Date of submission: __________________

ADVISOR’S APPROVAL SHEET

To: SoMCM Engineering Automotive Engineering Department

Subject: Thesis Submission

This is to certify that the thesis entitled “**Computational Evaluation of Aerodynamic Performance of Isuzu Midi Bus Body**” submitted in partial fulfillment of the requirements for the degree of Master’s in Automotive Engineering, the graduate program of the department of Automotive Engineering, and has been carried out by Natnael Bekele Kidane Id.No. A/PR15460/10 under my supervision. Therefore, I recommend that the student has fulfilled the requirements and hence hereby he can submit the thesis to the department.

______________________	______________	______________
Advisor	Signature	Date

ACKNOWLEDGEMENT

First of all, I would like to thank the almighty God, for giving me the knowledge and wisdom and providing me the resources to acquire education. I would also like to thank my mother and siblings for their support. I would like to thank my teachers N. Ramesh Babu (Ass. Professor) and Mekonen Liben (Asst. Prof) for their academic support. I would like to express my sincere gratitude for my thesis advisor Dr. Gezahegn Habtamu for his excellent guidance, moral support, and constructive criticism, corrections and helps. Finally, I would like to thank my friends and Defence University Engineering College, Aeronautics Department laboratory assistants for their support.

ABSTRACT

The aerodynamic drag reduction problem is a major topic in the automotive industry because of its close link with reduction of fuel consumption and exhaust emission. Many buses travel large distances at higher speeds. The significant increase in road transport combined with the increasing environmental issues and fuel prices has renewed the interest in bus design. Reducing the aerodynamic drag has a large positive influence on the fuel economy and the reduction of harmful exhaust gases. There are many buses available in Ethiopia most of these buses have poor aerodynamic shape which seems rectangular blunt, which has high drag resistance force these leads to increased fuel consumption. Isuzu Midi Bus is one of the most available buses in Ethiopia, its outer exterior body is built locally with poor aerodynamic shape. The main objective of this study was to improve the outer body shape of the existing Isuzu Midi Bus aerodynamically in order to reduce the overall aerodynamic drag force which in turn results in reduction of fuel consumption and carbon dioxide emission. The analyses were performed both numerically using Computational Fluid Dynamic /ANSYS Fluent, and experimentally for validation using Wind Tunnel. A baseline model of the bus modeled with SolidWorks with scale of 1:20 was analyzed at various speeds and the coefficient of drag was found. Later modifications and addition of rear spoiler were made to this base design in order to reduce the coefficient of drag and lift. Four models such as model I, model II, model III, and model IV were prepared. The coefficient of drag was later converted into quantifiable performance parameters such as fuel efficiency and CO_2 emissions. The aerodynamic shape improvement in model IV reduced the drag coefficient by 54.35% which has resulted in the percentage reduction in fuel consumption of 32.61% and exhaust gas emission 9.7%. This reduction of exhaust emission has a significant effect in the environment.

Keywords: Aerodynamics, CFD, Drag coefficient, Wind tunnel

TABLE OF CONTENTS

CONTENTS **PAGE**

LIST OF FIGURES

FIGURES **PAGE**

LIST OF TABLES

TABLES **PAGE**

ACRONYMS

AFC…………………………………………….…Active Flow Control

ANSYS…………………………………………Analysis System

CAD……………………………………………. Computer-Aided Design

CFD……………………………………………. Computational Fluid Dynamics

DNS……………………………………………. Direct Numerical Simulation

GHG…………………………………………… Greenhouse Gas

KMPL…………………………………………. Kilometer Per Litre

LDA……………………………………….…... Laser Doppler Anemometry

LES……………………………………………. Large Eddy Simulation

MPG……………………………………………Miles Per Gallon

NVH…………………………………….......... Noise, Vibration, and Harshness

PDE…………………………………………... Partial Differential Equations

PIV……………………………………………. Particle Image Velocimetry

PLA………………………………………….....Polyacetide

RANS…………………………………….…… Reynolds Averaged Naiver-Stokes

RNG…………………………………………... Renormalization Group

SST.………………………………………….... Shear Stress Transport

URANS……………………………………….. Unsteady Reynolds-Averaged Navier-Stokes

NOMENCLATURE

C_d………………..…. Drag Coefficient

C_p………………..…. Pressure Drag

F_f …………………... Friction Drag (N)

F_l……………..…..…. Lift Force (N)

F_d ……………......…. Drag Force (N)

P_s………………..……Static Pressure (Pa)

P_d…………………..…... Dynamic Pressure (Pa)

P……………………. Pressure (Pa)

T……………………. Temperature (K)

V……………………. Speed (m/s)

g……………….……. Gravity (m/s^2)

K………………….… Coefficient of Thermal Conductivity (W/m K)

GREEK LETTERS

ρ……………………. Density (kg/m^3)

ε……………………. Epsilon

Φ……………………Viscous Dissipation Function

μ…………….....……. Viscosity (m^2/s)

SUBSCRIPTS

d……………………. Drag

p……………………. Pressure

f……………….……. Friction

l………….…………. Lift

1. INTRODUCTION

1.1 Background of the Study

During the first years of the automotive industry, vehicle aerodynamics was only taken into consideration when designing racing cars. The major activity to serious attempts at drags reduction for mass-produced vehicles came in 1973 when a group of oil-exporting countries formed a cartel, drastically increasing the price of crude oil, and simultaneously cutting production (Barnard, 2009). The shortage of fuel in the market at that time frightened the automotive industry. Automakers had to invest in the production of cars with lower fuel consumption. A moving vehicle causes the displacement of the surrounding air and generates a resultant resistive force called drag which accounts for the major parts of the total resistance to the motion of the vehicle.

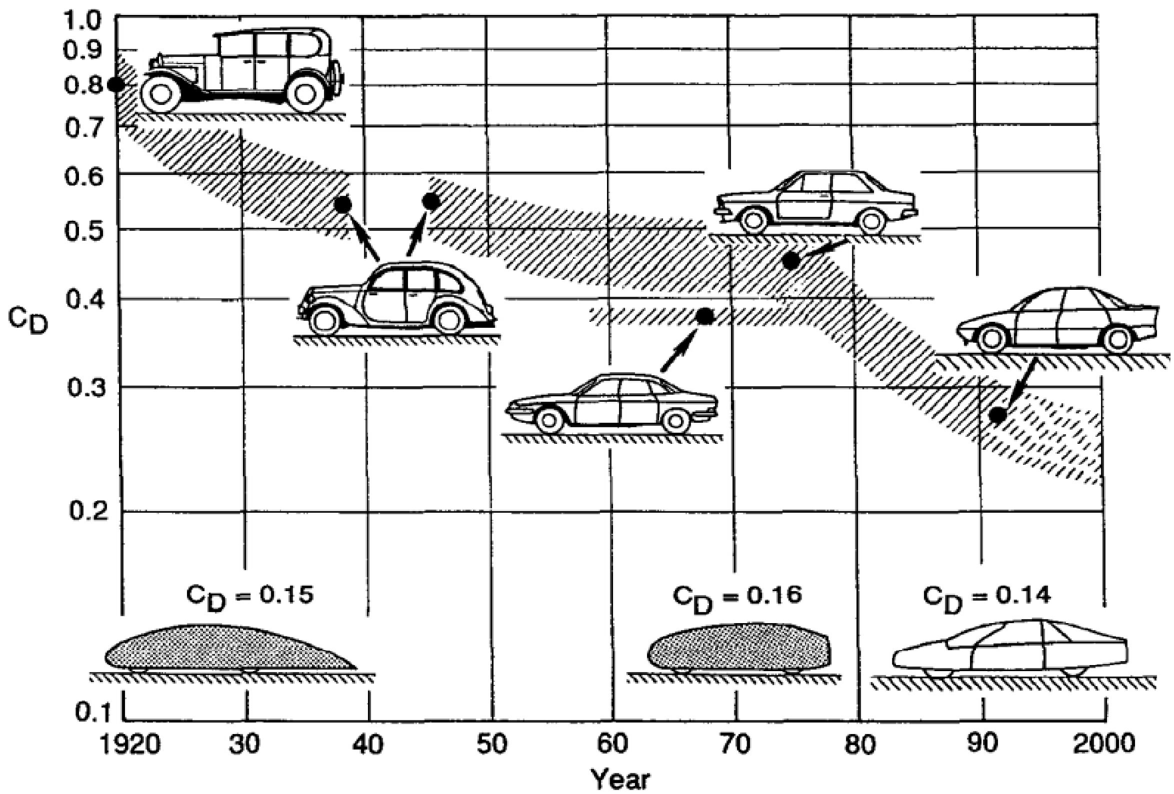

Figure 1. 1: History of drag coefficients for passenger vehicles (Hucho and Sovran, 1998)

"Aerodynamics" is the branch of fluid dynamics concerned with studying the motion of air, particularly when it interacts with moving objects. Aerodynamics and its analysis are basically divided into two major sub-categories, namely the external and internal aerodynamics. External aerodynamics is the study of flow around solid objects of various shapes. In the automotive industry, aerodynamic analysis can be carried out, principally, in two ways: Experimental research and Computational Fluid Dynamics (CFD). A major objective of the aerodynamic design of vehicles is to minimize drag and preventing undesired lift forces at high speeds. The most effective approach to drag reduction is concentrating on the body surfaces that make up the largest percentage of the overall drag. Recent developments in streamlining the external bodies of vehicles, including drag reduction attachments for commercial vehicles, have achieved a considerable reduction in drag (Hucho and Sovran, 1998) as shown in Figure 1.1. The drag coefficients have come down dramatically from earlier to recent vehicles. This has been a major contributor to the large improvements in fuel economy that have been realized. The redesign and modification of car bodies help to reduce the overall aerodynamic drag. Moreover, the drag force can be reduced by using add-on devices. In the process of car design, the aerodynamics must be seriously considered (Bansal and Sharma, 2014).

Figure 1. 2: Existing Isuzu light truck ()

Due to the environmental effect, more efficient road vehicles are being developed and improved, aerodynamics is needed for the design of optimal body shapes (Muthuvel et al., 2013). Today’s car companies are now basing their vehicles on being more aerodynamically fit with the main goal to develop clean, efficient and sustainable vehicles for urban transport. Moreover, the performance, handling, safety, and comfort of a passenger car are significantly affected by its aerodynamic properties. Getting high power under normal conditions is not enough to judge the performance of the car. Aerodynamic properties must be considered for the purpose of studying the drag and stability performance of a car (Reddy and Lokanadham, 2017).

There are many motor vehicles available in Ethiopia most of them are imported from foreign countries but some of those vehicles are locally fabricated (body) without the engine compartments and chassis layout. Most of the vehicle bodybuilding companies are not considering aerodynamic aspects when designed the outer body shape of the vehicles.

Figure 1. 3: Existing Isuzu Midi Bus during assembly at Kemal bus bodybuilding company

The Light Truck Isuzu (Figure 1.2) is the most commonly available truck's in Ethiopia which is imported from a Japanese commercial vehicle and diesel engine manufacturing company found in

Japan. However, the outer body of the Light Truck Isuzu is modified to Midi Bus without changing the chassis layout at different bus bodybuilding companies and garages as shown in Figure 1.3. This study focuses on the vehicle's aerodynamics, especially to reduce the overall aerodynamic drag force of the existing Isuzu Midi Bus that influences directly the fuel consumption. Modifying the outside body design and using drag reduction devices were the main ways of reducing the drag force of this bus. Extra parts are added to the bus body to direct the airflow in a different way and offer greater drag reduction to the bus and at the same time enhance the stability. This extra device called "Rear Spoiler", which is an aerodynamic device that is designed to spoil unfavorable air movement across a car body to decrease the overall drag, and at the same time increase downward force. The main fixing location is at rear end of the bus. The aerodynamic drag of a bus is responsible for a large part of the vehicle's fuel consumption and contributes up to 50% of the total vehicle fuel consumption at speed above 60 kmph (Barnard, 2001).

1.2 Statement of the Problem

Isuzu Motors is a Japanese commercial vehicle and diesel engine manufacturing company headquartered in Tokyo. The Light Truck Isuzu imported from Japan used for loading materials but it's modified to an Isuzu Midi Bus by changing the body without chassis here in Ethiopia at different bus bodybuilding companies and garages. An Isuzu Midi Buses are the most popular bus in Ethiopia; many public means of transport in urban and rural areas of Ethiopia are using this bus. However, the bus body building companies prioritize the exterior looks of the bus and ignore the aerodynamic aspect. The bus has a poor aerodynamic shape which is almost rectangular blunt, which has a high drag resistance force these leads to increased fuel consumption. The aerodynamic drag is the most important factor, responsible for resistance to motion, especially at high speeds. With increased resistance to motion the vehicle must produce additional power by utilizing more fuel to overcome the drag which results in increased emission. Drag reduction in buses is generally obtained by rounding off the sharp edges. However, drag can be reduced to lower levels by making the boxy shape of the bus into a more streamlined one (Siva and Loganathan, 2016).

1.3 Objectives

1.3.1 General Objective

The general objective of this study is to improve the outer body shape of the existing Isuzu Midi Bus aerodynamically in order to reduce the overall aerodynamic drag force which in turn results in the reduction of fuel consumption and carbon dioxide emission.

1.3.2 Specific Objectives

The specific objectives are:

- ❖ To prepare a simplified geometrical model of a locally fabricated Isuzu Midi Bus body shape as a baseline model, other aerodynamically improved models and Rear Spoiler using SolidWorks.
- ❖ To perform the flow analysis on the prepared models by modifying windshield angle, front and rear surface geometry using ANSYS Fluent for various speeds.
- ❖ To estimate the aerodynamic drag and lift coefficients of all the prepared models as well as to visualize the flow pattern using ANSYS Fluent software.
- ❖ To prepare the experimental model of the baseline in the 3D printer and validate the computational result of drag and lift coefficients of the baseline model experimentally on the wind tunnel as well as investigate fuel consumption and emission of the model.

1.4 Scope of the Study

This study delimited only on reducing the aerodynamic drag coefficient of an Isuzu Midi Bus by modifying the outer body shape and using the rear spoiler as well as analyze the airflow around the bus using CFD and validate the obtained computational results experimentally using wind tunnel test.

1.5 Significance of the Study

The final outcome of this study would give a better contribution to an Isuzu Midi Bus manufacturers especially during the body styling process, which leads to improving the aerodynamic performance, fuel economy and engine performance. Performance, handling, safety, and comfort of a passenger car are significantly affected by vehicle aerodynamic properties. It is also expected to give a better understanding of the flow field over the bus, turbulent structure of the bus wake, and emphasizes more on how to implement an aerodynamic experiment. Whereas the result of this thesis can be useful as a reference for individuals, researchers, and manufacturers who are engaged in bus body design, to reduce the drag and lift forces, which will result in reducing fuel consumption and emission.

1.6 Limitations

In the automotive industry, aerodynamic analysis carried out, principally, in two ways: Experimentally (Wind-tunnel test) and Numerically using ANSYS Fluent software. To perform the numerical analysis, it's necessary to use a high-performance computer to obtain accurate results. Moreover, there are no large-sized powerful Wind-tunnels and high cost of preparing a 3D model of an Isuzu Midi Bus are the main limitations. The study also focus on a simplified 3D model of Isuzu Midi Bus body aerodynamic performance excluding parts such as side-view mirrors, windscreen wipers, mudflaps and roof rack while designing the models.

1.7 Structure of the Thesis

This Thesis consists of six chapters. The first chapter is an introduction to the study. It includes the background of the study, statement of the problem, objectives, scopes, significant of the study, limitation, and structure of the thesis. Chapter two focuses on different kinds of literature that emphasize on study of bus aerodynamics and computational fluid dynamics analysis. Chapter three describes CFD analysis of aerodynamic performance of the bus and methodology used to complete this work. Also, deals with bus model concepts geometry development and simulation setup. Chapter four presented experimental validation of the computational analysis. Chapter five depicted results and discussions of computational analysis and experimental validation. The drag and lift coefficients are presented in form of tables and graphics for quantitative and qualitative discussions. The final chapter of this thesis consists of conclusions and recommendations.

2. LITERATURE REVIEW

In recent years, a number of researchers have reported the aerodynamic study of the vehicle body using CFD. Some studies are carried out in the aerodynamics of road vehicle domains related to add-on devices, optimizing vehicle body, reduction of drag force and performance of vehicle have been conducted in order to obtain a better understanding of the work carried out previously. The studies that have been the most helpful in addressing various aspects related to this study are summed up in this section. At the end of this chapter, the research gap is pointed out.

2.1 Previous Investigations

Watkins, (1999) compared the modern car with old cars. Modern cars are rounder and more streamlined compared to cars in the ’60s and ’70s. The styling changed due to the assimilation of road vehicles to planes and race cars. Low aerodynamic drag is preferred and this requires cars to be rounder and curvier. To reduce pressure drag, it is important to reduce the flow separations from the car surfaces. As much as possible, airflow on the boundary needs to be maintained its course without sudden deviation that can cause vortex and hence fluctuation in static pressure. The increase in drag is a drawback as it is directly linked to fuel consumption. This performance is important because the emission from automobiles is accounting for about 10% of global carbon dioxide emissions, a major contributor to the greenhouse effect (Metz, 2001).

Siva and Loganathan, (2016) considered the external design of Toyota Fortuner and it was modeled by using SOLIDWORKS to reduce the drag of the car by modifying the car shape, while the interior of the vehicle was not modeled. Then external flow analyses for the modified and existing car models were carried out using ANSYS Fluent to determine the aerodynamic characteristics like pressure, drag and lift forces for various speed. The results obtained showed that the optimized model has a better aerodynamic performance than the existing model. So, due to the exterior design modification, the drag will be reduced by increasing the car performance.

Sonawane et al., (2011) studied on car body by changing the slant angle of the car body to reduce fuel consumption. The simulation was performed for different slant angles and concluded that with a change in the slant angle of the car body from 30 degrees to 20 degrees there is a reduction of 8% in drag force which leads to 1.5 to 5.0% of the decrease in fuel consumption. The result showed that fuel consumption can be significantly reduced by appropriate change in slant angle for the car body. Fuel consumption is directly dependent on the drag force resistance acting over the car body. The drag is directly dependent on the slant angle of the body. The larger the slant angle more pressure difference of the front and back surfaces generates more drag but less slant angle allows more surface of the body to be in contact with the fluid and more skin friction results

Wang et al. (2017) analyzed the aerodynamic performance of the Model S vehicle of Tesla by using STAR-CCM+ software at different working conditions for ground-clearance, tire rotation, tread pattern and so on. The drag coefficient and local flow field data of the vehicle in different working conditions are simulated and the mechanism of flow is analyzed. Then, the drag and lift coefficients in different working conditions are obtained and checked the contribution of each part of the vehicle to the overall coefficient of air drag. The simulation results showed that the contribution of different parts of the outer surfaces to the overall coefficient of drag of the vehicle. The greatest contribution to air drag is from the face parts in the front of the vehicle.

Vipul and Chopade, (2018) studied external fluid dynamics of the racing cars to improve the aerodynamic performance. Also, discussed the methods to stabilize the vehicle at high speed and while taking corners during racing by using different accessories which are very useful in the handling of the vehicle and reducing fuel consumption as well. Race cars are aerodynamically designed to reduce drag force or decrease vehicle's resistance and enhance downforce. Drag forces limit maximum speed and affect fuel consumption although downforce is used to provide stability when driving around corners.

In the automotive industry, according to Hucho and Sovran, (1998) the "concept" of any car is influenced by a variety of requirements such as traffic policy, technology level, fashion, government regulations and etc. as shown in Figure 2.1 which, collectively summarized by the term "market". However, the long-known potential for reducing drag (which relates to one of these factors) is now being exploited more and more. How far this trend will go depends on the future course of fuel prices and emissions regulation. Fuel economy and, increasingly global warming are the current key arguments for low drag worldwide. A careful balance between them is required by the market.

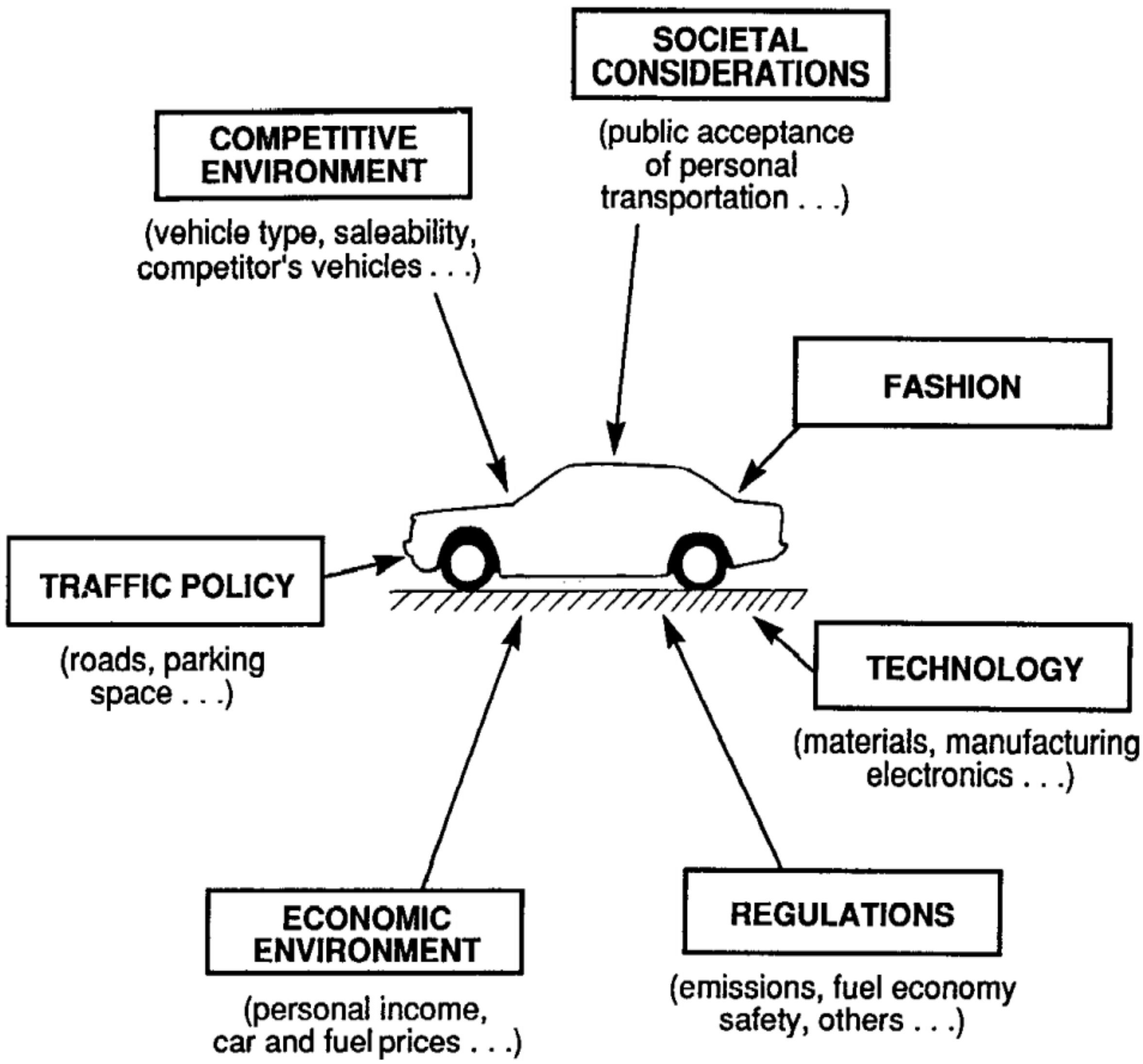

Figure 2. 1: The concept of a car is influenced by many requirements of a very different nature (Hucho and Sovran, 1998).

2.2 Air Flow Over the Car

Figure 2.2 shows the streamline of an external flow around a stationary vehicle. When the vehicle is moving at an undistributed velocity, the viscous effects in the fluid are restricted to a thin layer called boundary layer. Outside the boundary layer is the inviscid flow. This fluid flow imposes pressure force on the boundary layer. When the air reaches the rear part of the vehicle, the fluid gets detached. Within the boundary layer, the movement of the fluid is totally governed by the viscous effects of the fluid.

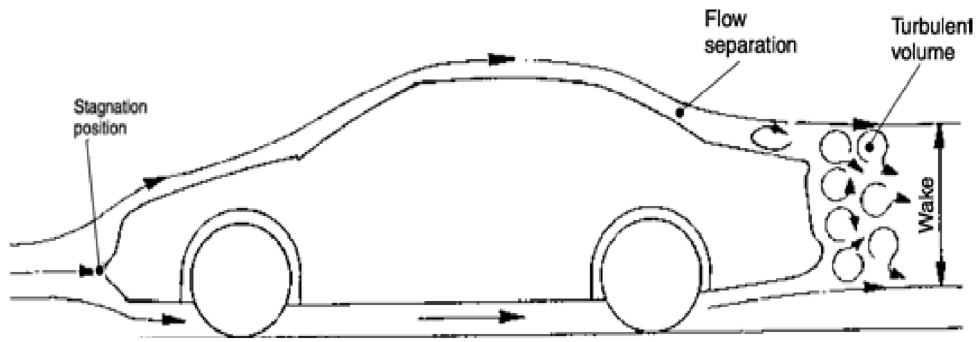

Figure 2. 2: External flow field over the car body (Taherian and Bhave, 2014)

The boundary does not exist for the Reynolds Number which is lower than 10^4. The Reynolds number is dependent on the characteristic length of the vehicle, the kinematic viscosity and the speed of the vehicle. Apparently, the fluid moving around the vehicle is dependent on the shape of the vehicle and the Reynolds number. There is another important phenomenon that affects the flow of the car and the performance of the vehicle. This phenomenon is commonly known as 'Wake' of the vehicle. When the air moving over the vehicle is separated at the rear end, it leaves a large low-pressure turbulent region behind the vehicle known as the wake. This wake contributes to the formation of pressure drag, which eventually reduces vehicle performance (Selvaraju et al., 2015).

Pravin and Hiwase, (2014) argued that the most aerodynamic shape is the teardrop, which has a theoretical C_d of 0.05 which is very low. Due to the smooth curve at the front of the teardrop and the long gradual slope of the tail the airflow stays attached to the surface of the teardrop. The air around it is deflected away very gently, limiting the amount of turbulent flow as the air rejoins at the tail of the teardrop. The air becomes detached from the surface when a sudden change in the shape occurs, for example when there is a sudden steep incline or sharp edge the flow detaches and can become turbulent. It is, however, not practical to shape a car like a teardrop as there is a need for enough space for multiple occupants and a sizable luggage compartment.

2.3 Drag Reduction Methods

In these techniques, many attempts have been made since the early years in the automotive industry to reduce aerodynamic drag in order to improve the aerodynamic effect as well as improving fuel efficiency.

Maji et al. (2007) developed a highly streamlined concept vehicle using only aerofoils. A single piece shell body was developed by placing selected aerofoils at their appropriate locations. Guo et al. (2011) performed aerodynamic analysis of different two-dimensional car geometries using CFD. In the first part of the study, the influence of the front body shape was studied. Two models were used; one with sharp edges and the other with smooth rounded edges. Larger stagnation areas were observed on the sharp-edged geometry as compared to smooth and rounded-edged geometry. Smooth edged geometry also showed reduced pressure areas at bottom of the front end. In the second part of the study, different rear geometries with different backlight angle were studied.

Rakibul et al. (2014) considered some design aspects while designing a car for higher speed and lower drag of any bluff should keep the flow attached to the body as much as possible i.e. maintaining streamline shape, reducing surface roughness, fewer joints of the body or avoiding sharp fillets, controlling lift force, air or exhaust gas flow towards the low-pressure zone at the rear portion of the car, etc.

2.4 Factors Contributing to Flow Field Around Vehicle

Aerodynamic drag consists mainly two-components skin friction drag and pressure drag. Pressure drag account most of the total aerodynamic drag which depends on external geometry due to boundary layer flow separation from rear window surface and wake region behind the vehicle. The location of the separation point determines the size of wake region and consequently it determines the value of drag coefficient. Flow separation control of car is major interest in fundamental fluid dynamics as well as in various engineering applications (Desai and Molvi, 2017). The major factors which affect flow field around vehicle are the boundary layers, separation of flow field, and drag force.

2.4.1 Boundary Layer

The basic concept of Boundary Layer and its understanding on a flat plate is important as prerequisite for the study of vehicle aerodynamics. An important feature of the flow past a vehicle is that the air appears to stick to the surface. The thin layer where the velocity gradient is significant is known as the boundary layer (also known as the non-slip condition), it increases from zero velocity at the surface to the velocity at the free stream (Barnard, 2009). The boundary layer thickness increases away from the surface as it progresses from the front to the rear of the body. The larger boundary layer at the rear of the body means the stagnation pressure is less towards the rear than the front, this effective pressure drop along the length of the body causes the drag force. Despite the thinness of the boundary layer near the wall, it has a strong influence on the flow field around the body. Fluid flow within the boundary layer is categorized into two main groups; laminar and turbulent. In the front most part of the boundary layer the flow is steady and almost parallel to the wall which is known as laminar flow. Further down the body the boundary layer increases in size away from the wall due to the increase in kinematic viscosity, this is known as the turbulent part of the boundary layer (Cogan, 2016).

The transition between the two states of flow is governed by the Reynolds number. Reynolds number is a dimensionless parameter that characterizes the transition from laminar to turbulent flow in a viscous fluid. It gives a ratio of internal forces to viscous forces for a specific length, however, it is also possible for the fluid flow to transition from laminar to turbulent from disturbances such as surface roughness.

2.4.2 Flow Separation

During the air flows over the surface of the vehicle, there is a point when the change in velocity comes to stall and the fluid starts flowing in reverse direction. This phenomenon is called Flow Separation of the fluid flow. This usually occurs at the rear part of the vehicle as shown in Figure 2.3. This separation is highly dependent on the pressure distribution which is imposed by the outer layer of the flow.

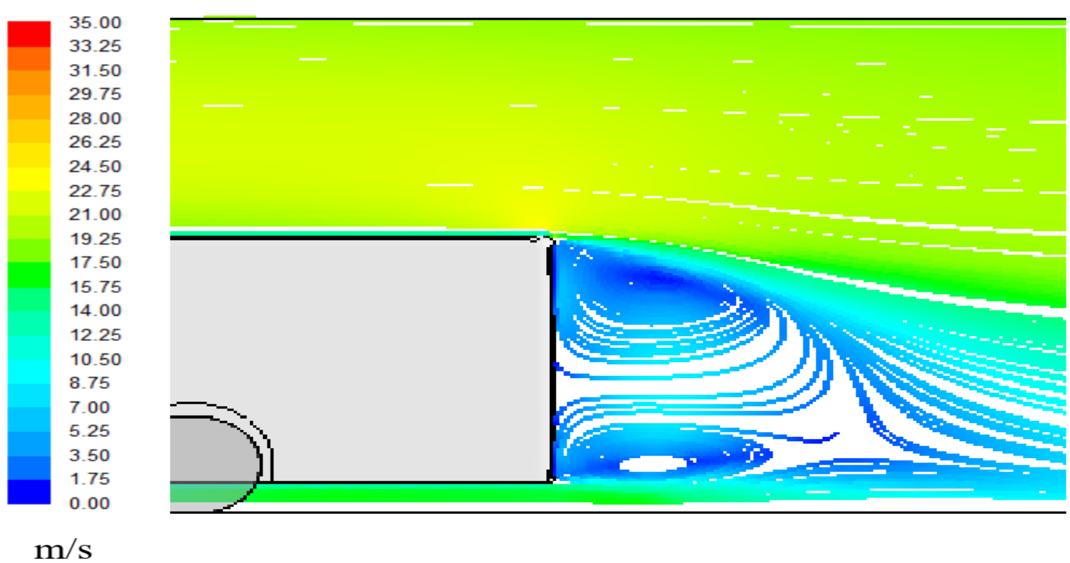

Figure 2. 3: Velocity streamlines showing flow separation at the rear of the bus (Taherian and Bhave, 2014)

In a turbulent boundary layer, the flow is still streamlined in the sense that it follows the contour of the body. The turbulent motions are of very small scales. A separated flow does not follow the contours of the body (Barnard, 2009).

Flow separation is bad because it leads to a larger wake and less pressure on the rear surface which reducing pressure recovery. To avoid bad flow separation, the transitions of the airflows from the roof to the rear window need to be smoothed (Roumeas et al., 2008). The bad separation also can create more drag. The aerodynamic will be more effective if the flows working in laminar flow. By improving the aerodynamics of the car can reduce the boundary layer thickness thus avoids worst flow separations.

2.5 Flow Control

Flow control is one of the promising fields of fluid dynamics which is helpful in drag reduction by controlling the location of the separation or keeping the flow attached to the wall as further possible or help to reattach. If these conditions are fulfilled the drag coefficient will be smaller, and the aerodynamic performance becomes more effective. Based on whether the methods consume energy to control the flow or not, they are categorized into active or passive control systems (Wassen and Thiele, 2010). Many researchers carried out a number of researches with regard to active and passive flow control methods on vehicle and their effect on aerodynamic drag.

2.5.1 Passive Flow Control

The passive control systems consist of the use of more or less discrete obstacles (attaching add-on devices), added around or on the roof of the vehicle to reduce the aerodynamic drag. They can be declined in two groups according to their influence on the flow control. The first group consists of obstacles positioned on the surface of the geometry. The second group consists of the obstacles positioned upstream or downstream of the geometry to be controlled (Kourta and Gillieron, 2009). Also, this approach includes shape modification on the vehicle body.

Effect of Spoiler on Aerodynamic Performance

The drag force is produced by relative motion between air and vehicle and about 60 % of total drag at the rear end. A spoiler can be divided into the front spoilers (air dam) and rear spoilers which is a device used to minimize unfavorable air movement around the vehicle to improve aerodynamic performance. A front spoiler connected with the bumper mainly used to direct airflow away from the tires to the underbody, which generally reduces aerodynamic lift and drag. A rear spoiler (Rear wing) is commonly installed at rear end of a vehicle, which diffuses the airflow passing a vehicle, which minimizes the turbulence at the rear of the vehicle, adds more downward pressure to the back end and reduces lift acted on the rear trunk. The goal of many spoilers used in passenger vehicles is to reduce drag and increase fuel efficiency (Zakem, 2008). The rear spoilers contribute to the major aerodynamic stability of the car (Hu and Wong, 2011).

Hu and Wong, (2011) investigated the flow around a simplified passenger car with a rear-spoiler and without a rear-spoiler at high speed by using a standard k-ε model that was selected as a turbulence model for numerically simulate the external flow field of the simplified Camry model. Through an analysis of the simulation results, the high-speed passenger car with rear spoiler shows that the aerodynamic drag is reduced by 1.7% and also it increases negative lift. This leads to the vehicle's less fuel consumption on the road. Also using rear spoiler would result in improving tires capability to produce cornering force, braking performance, and stability with better traction.

Ganesh, (2015) investigated aerodynamic characteristics of a Honda civic car 2009 with and without rear end spoiler at a different location with the help of AUTODESK flow design software. When the rear end spoiler applied to the Honda Civic car model, which helps to reduce the flow separation. Reducing flow separation decreases drag, which increases fuel economy. Through analysis with AUTODESK results, the drag coefficient of a car model with spoiler and without spoiler was 0.21 and 0.28, respectively. Therefore, the aerodynamic drag reduced up to 25%, which results improving the performance of Honda Civic car model.

2.5.2 Active Flow Control

Active flow control aims at alternating a natural flow or developing the flow into a more desired path. Active flow control basically involves the addition of auxiliary power into the flow for external devices introduced. It is performed by using actuators that require a power generally taken on the principal generator of energy of the vehicle. The visible part of these systems includes mobile walls, circular holes or slots distributed on the vehicle surface where the flow must be controlled. Their use requires mechanical, electromagnetic, electric, piezoelectric or acoustic systems placed in the hollow parts of the vehicle. Their weights and their overall dimensions must be smallest as possible to reduce their impacts on consumption and habitable volume. Several control solutions have been identified, tested and analyzed for aeronautics. It has been the same for the hydrodynamic and aerodynamic of the road vehicles. The adopted solutions generally consist of suction or blowing systems through circular or rectangular slots (Kourta and Gilliéron, 2009).

2.6 Bus Aerodynamics

Buses play a vital role in mass transportation around the globe. As bus body is not designed aerodynamically, therefore, coefficient of drag is high. Nowadays rising of fuel price and strict government regulations makes road transport uneconomical. In recent times, due to better road, the buses cover large distances on highways at speeds of over 100 kmph. At these speeds the drag force exceeds the power spent on overcoming the rolling resistance.

The bus body building companies' precedences are the outer surface and structure of the bus and ignore the aerodynamic aspect. But these buses have a poor aerodynamic exterior design. Therefore, to get a better aerodynamic performance the forebody, underbody, roof and trailing end of the bus has to be modified. The teardrop shape is an ideal aerodynamic shape that is largely used in submarine hull and aircraft body designs to reduce the drag. Body modification is the passive technique to enhance aerodynamic drag reduction which helps to reduce fuel consumption. Body modification includes vehicle body outline, front and rear part; underbody geometry of the vehicle.

In a bus, the resistance due to the aerodynamics plays a vital role at higher speeds. When the design of the bus body is very flat the resistance is more. It is said that about 60-70 percent of the total wind-averaged drag of a bus is attributed to pressure loads acting on the vehicle fore-body making it the principal area for drag reduction (Patten et al., 2012). The power required to overcome the resistance is very high, hence it is sure that aerodynamics is an important factor to be considered. From many reviews, it is clear using add on components would reduce the drag force. (Raveendran et al., 2009) worked on his research changing the body design by lowering the body of the bus and reduced the drag coefficient up to 0.29 from 0.53.

Saravanan et al. (2016) performed experimental analysis using CFD/ Ansys fluent software by modeling two different models, the first model was an existing model of Tata Star 54 bus and the later model was the model with modification in front and rear end. The result showed that there has been a 40% reduction in drag coefficient from the existing bus to the new concept and up to 5 to 6 liters of fuel consumed for every 100 kms is saved. This improvement in fuel efficiency will have a high impact on the reduction of annual fuel consumption, which will greatly influence the Government regulations, making road transport more efficient.

Muthuvel et al. (2013) fabricated four different prototypes for performing experimental and numerical analysis using wind tunnel and CFD software to prove the effectiveness of the new concept design. The first bus model is the existing model, the second is the existing model with the rear end modified, the third bus is the existing bus with the front end modified and the fourth model is the model with modification at the front and rear end. All four models were separately tested for optimizing how each modification is contributing towards the drag force. It was found that the least drag force was acting on the fourth bus model. The test result showed that there is a considerable reduction in drag force of about 30-34% from the existing bus to the new concept and 6 to 7 liters of fuel is consumed for every 100 km. This improvement in fuel efficiency will have a high impact on the reduction of global warming.

Gawad and Aziz, (2006) investigated experimentally and numerically the effect of the front shape of buses on the characteristics of the flow field and heat transfer from the rear of the bus in driving tunnels by prepared three bus models with flat-, inclined-, and curved-front shapes. The result found that the front shape with a curved surface has lower drag coefficient than other models. Also, they stated that the cooling of the inclined- and curved-front vehicles is better than the cooling of the flat-front bus by about 20%.

Mohamed et al. (2014) attempted to reduce the gas emissions from buses by reducing the aerodynamic drag. Several ideas were applied to achieve this goal including slight modification of the outer shape of the bus. A computational model was developed to conduct the study. It was found that the reduction in aerodynamic drag up to 14% can be reached, which corresponds to an 8.4 % reduction in fuel consumption.

Raveendran et al. (2009) analyzed operating an intercity bus for body styling and aerodynamic performance by redesigning the outer body of the bus. Fluent, a commercial CFD code was used to evaluate the aerodynamic performance. The results of the redesigned exterior body showed a reduction of C_d from 0.53 to 0.29 and overall aerodynamic drag reduction by 60% due to combined effect of reduced C_d and frontal area.

Kim, (2011) concentrated on fine-tuning the front leading-edge radii of the bus. An optimum front edge radius of 150 mm was reported, and a further increase in the radius was found to have the least influence on the coefficient of drag of the bus as shown in Figure 2.4. It also proposed a new design for the frontal shape of the bus for the reduced coefficient of drag (with value of 0.34) as shown in Figure 2.4.

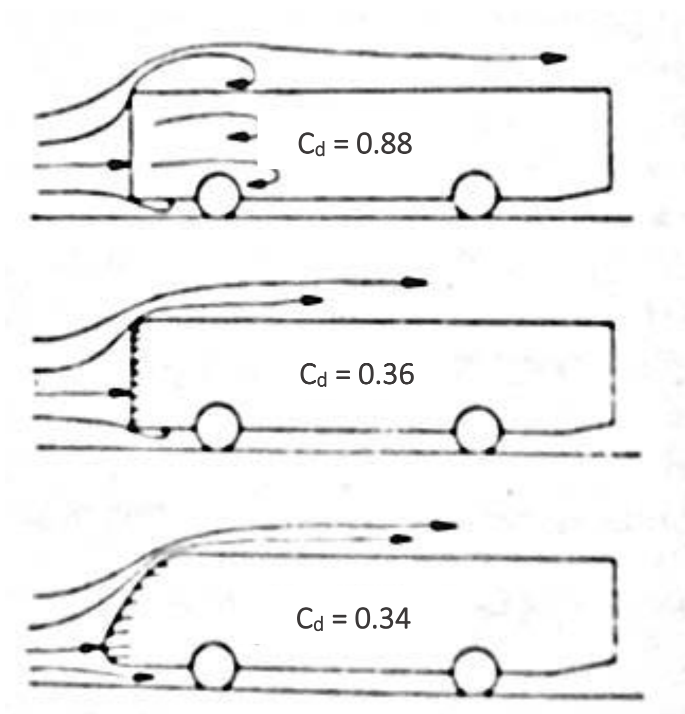

Figure 2. 4: Frontal shape design for the reduction in C_d (Kim, 2011)

Patil et al. (2012) examined the flow structure around a bus model using the CFD method. They developed three models to reduce the drag force of the bus model. In their study, they determined the drag coefficient of the base model bus as 0.53. They reduced the drag coefficient to 0.49 by modifying the front and rear surface of the bus. They have achieved to reduce the drag coefficient to 0.39 by adding the side panel, 0.40 by the rear spoiler. Thus, they achieved an aerodynamic improvement as 6.57, 25.82, and 24.42%, respectively. They optimized one of the conventional bus models and reduced drag by adding spoilers and panels at rear portion along with front face modification. The results showed that drag can be decreased without altering the internal passenger space and by least investment.

Cheng and Mansor, (2017) investigated the effect of rear-roof spoiler on the aerodynamic drag performance of a simple hatchback model (Figure 2.5) for a range of spoiler pitch angles using RANS based CFD method. The results showed that the simple strip-type spoiler could have a beneficial influence from 0 to 5° pitch angle. Beyond this range, the C_d increases with a larger pitch angle. The spoiler relies on two main mechanisms to reduce aerodynamic drag. First, by preventing the airflow from accelerating at the leading edge of the slant section. Second, by preventing the formation of longitudinal vortices at the side edge of the slant section.

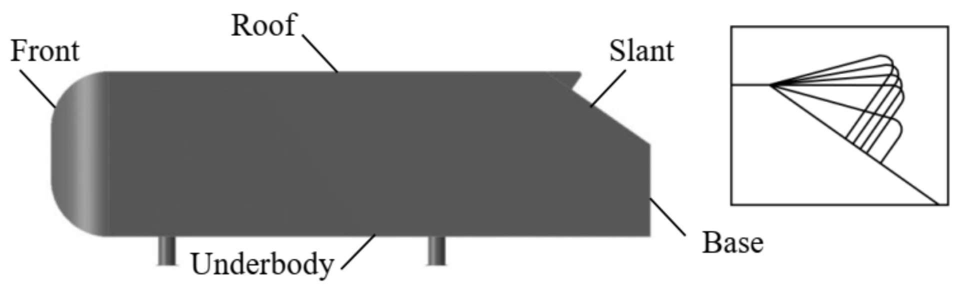

Figure 2. 5: Side view of Ahmed model fitted with a rear-roof spoiler (left), and the spoiler configurations (right), (Cheng and Mansor, 2017).

Kim et al. (2002) performed numerical simulation on the drag reduction of large size buses using rear-spoiler at the end of the upper body. The simulation was carried out using the CFD tool Fluent. The simulation resulted in 12% reduction in lift and 0.08% reduction in drag coefficient. Also, negative lift force worked in direction of ground enhancing the driving stability at high cruising speed.

2.7 Impact of Aerodynamic Drag on Fuel Consumption

The rapidly increasing fuel prices and the regulation of greenhouse gases to control global warming give tremendous pressure on design engineers to enhance the current designs of the vehicle using the concepts of aerodynamics to enhance the efficiency of vehicles (Krishnani, 2009). Fuel consumption due to aerodynamic drag consums more than half of the vehicle’s energy. Thus, the drag reduction program is one of the most interesting approaches to cater this matter.

Aerodynamic drag consists of two main components: skin friction drag and pressure drag. Pressure drag accounts for more than 80% of the total drag and it is highly dependent on vehicle geometry due to boundary layer separation from rear end surface and formation of wake region behind the vehicle. The location of separation determines the size of wake region and consequently, it determines the value of aerodynamic drag. According to Hucho and Sovran, (1998) aerodynamic drag of a road vehicle is responsible for a large part of the vehicle's fuel consumption and contributes up to 50% of the total vehicle fuel consumption at highway speeds. Reducing the aerodynamic drag offers an inexpensive solution to improve fuel efficiency and thus shape optimization for low drag becomes an essential part of the overall vehicle design process.

The ineffective aerodynamic shape results in excessive drag which leads to increased fuel consumption rates. Reducing aerodynamic drag is significant for the fuel consumption efficiency. In the United States, the ground vehicles consumed about 77% of all (domestic and imported) petroleum. It has been estimated that a 1% increase in fuel economy can save 245 million gallons of fuel per year. Additionally, the fuel consumption by ground vehicles accounts for over 30% of CO_2 and other greenhouse gas (GHG) emissions. Moreover, most of the usable energy from the engine goes into overcoming the aerodynamic drag (53%) and rolling resistance (32%); only 9% is required for auxiliary equipment and 6% is used by the drive-train. 15% reduction in aerodynamic drag at highway speed of 55 Mph can result in about 5–7% in fuel-saving (Bellman et al., 2010).

2.8 Automotive Reference Models

There are different reference models in the Automotive industry to study the airflow around a vehicle. All of them are considered as Bluff bodies. Every vehicle reference model has particular geometric shapes to study the fluid flow behavior around the models, under some defined conditions. The comprehension of that behavior on simple shapes helps to understand what will happen with more complex shapes. The most important reference model is the Ahmed model.

2.8.1 Bluff Body

Bluff bodies refer to bodies with blunt bases that cause leading-edge flow separation and the formation of recirculation regions in the near wake of the bluff body (Cooper, 2006). This results in lower pressure on the back surface of the body and sets up a large difference between the relatively high pressure acting on the front of the bluff body and the lower base pressure. Automotive bodies are considered as bluff bodies moving in close proximity to the ground. It has been established that the pressure drag is a direct consequence of flow separation which occurs primarily at the rear end of the body (Ahmed et al., 1984). More recently, (Desai and Molvi, 2017) mentioned that pressure drag account most of the total aerodynamic drag which depends on external geometry due to boundary layer flow separation from rear window surface and wake region behind the vehicle.

2.8.2 Ahmed Body

The generic Ahmed Body reference model (Figure 2.6) has been chosen as the benchmark for carrying out computations for studying the aerodynamic parameters, which consists of three parts: forebody, mid-section and rear body. The edges of the forebody are rounded to avoid flow separation, the midsection is a rectangle with sharp edges and rear end has interchangeable geometry which can be used to study the effect of different geometric configurations on aerodynamic drag and pressure distribution. The body was first proposed by (Ahmed et al., 1984).

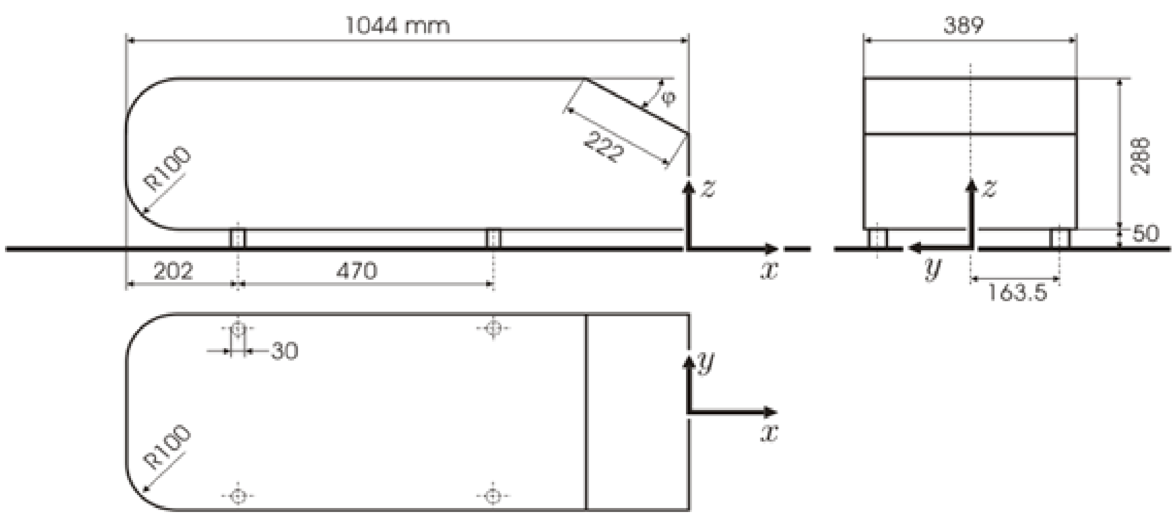

Figure 2. 6: Schematic of the Ahmed body (Ahmed et al., 1984)

The Ahmed body is a very simple bluff body which has a simple shape to allow accurate flow simulation but retains some important practical features relevant to automobile bodies. (Palande and Ashwini, 2016) the principal objective to study such a simplified car body is to tackle the flow processes involved in drag production. Through perceiving the mechanisms involved in creating drag one can be able to design a car to minimize drag and therefore reducing fuel consumption and maximize vehicle performance.

Ahmed et al. (1984) analyzed time-averaged wake structure around the Ahmed body at a Reynolds number equal to 4.29×10^{6}, detailed pressure measurements, wake survey and force measurements were done in a wind tunnel by manipulating the rear slant angle in the range of 0-40º in increments of 5º. Almost 85% of total aerodynamic drag is contributed by pressure drag and most of this resistance is generated at the rear end.

Thacker et al. (2012) analyzed the effect of canceling the separation on the rear slant of an Ahmed body (inclined at 25º) on the different structures developing in the wake as shown in Figure 2.7. In order to analyze the effect of suppression of the separation on the rear slant, two distinct models were used: the first one having a sharp edge at the connection between the roof and the rear slant and the second one with a rounded edge preventing flow separation on the rear slant as shown in Figure 2.8.

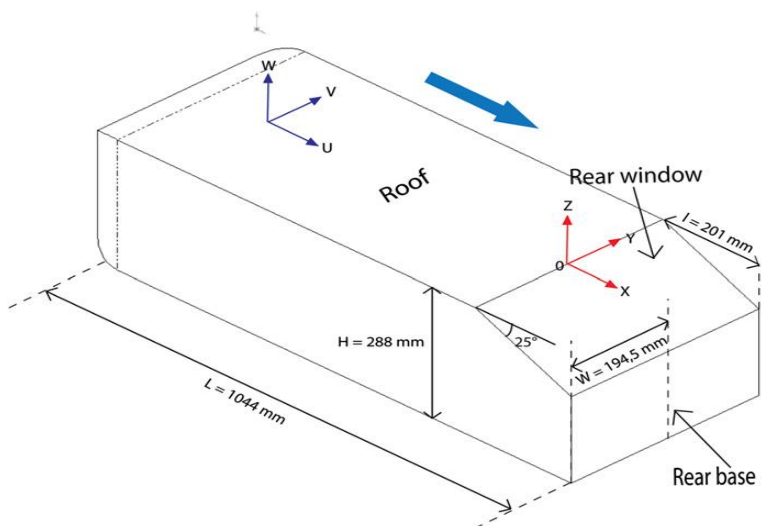

Figure 2. 7: Ahmed body model with a slant angle of 25º at a geometric scale of 1:1 (Thacker et al., 2012)

Aerodynamic loads, wall pressure distribution, friction line visualizations, and PIV velocity fields have been performed to compare the two flow configurations. The comparison between the two configurations showed a drag variation of 10% while the lift level remains unchanged. The absence of the separation bubble on the rear window mainly affects the near rear wake that strongly contributes to the weaker drag level.

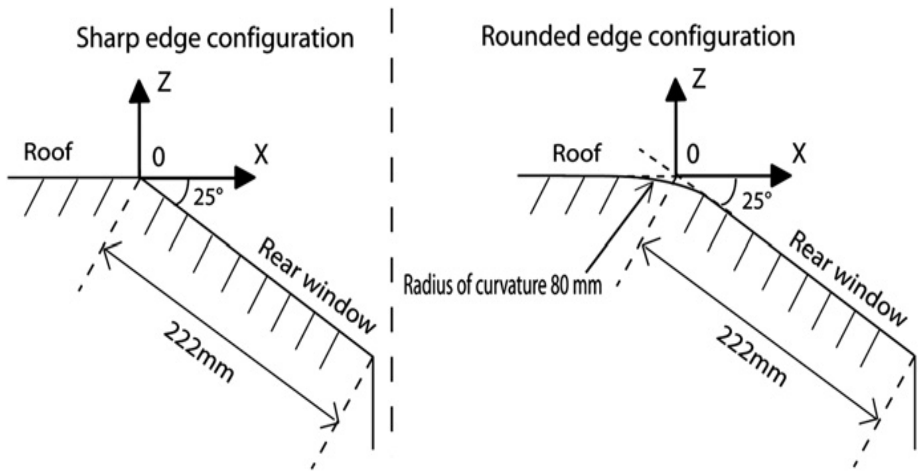

Figure 2. 8: Sharp- and rounded-edge configurations between the roof and the rear window (Thacker et al., 2012)

Banga et al. (2015) analyzed a solution to reduce road vehicle inefficiencies and losses due to aerodynamic drag and lift, accomplished by investigating the variation of the rear slant angle of the Ahmed body and its effect on the drag and lift coefficients and determine the optimum angle for least drag through numerical simulation. The minimum coefficient of drag 0.2346 is obtained with configuration of Ahmed Body with 7.5º rear slant angle. The drag increases as the rear slant angle are reduced and increased from 7.5º down to 0º and up to 30º, respectively.

2.9 Computational Fluid Dynamics (CFD)

Computational Fluid Dynamic (CFD) is the branch of fluid dynamics providing a cost-effective mean of simulating real flows by the numerical solution of the governing equation. The governing equations for Newtonian fluid dynamics, namely the Navier-Stoke equation. The differential equation governing the system is converted to a set of the algebraic equation at discrete points and then solved using digital computer. For such a complex interaction, CFD analysis is probably the only efficient tool in order to assess specific design parameterization of a generic car shape. Aerodynamic evaluation of airflow over an object can be performed using analytical method or CFD approach. On one hand the analytical method of solving airflow over an object can be done only for simple flows over simple geometries like laminar flow over a flat plate. If airflow gets complex as inflows over a bluff body, the flow becomes turbulent and it is impossible to solve Navier-Stokes and continuity equations analytically, in that case CFD is useful (Vipul and Chopade, 2018).

The CFD (Computational Fluid Dynamics) analysis is used to find the parameter in the automobile industry. This analysis is used to understand the fuel consumption, stability of the vehicle and passenger comfort. The airflow over ground vehicle is analyzed and coefficient of drag is calculated using CFD/ Ansys Fluent (Rehan and Sudhakar, 2014). With the increase in computational power, CFD has become a valuable tool for performing the different cases in vehicle motion simulation and predicting the drag coefficients.

CFD simulation is an efficient tool in automotive industry extensively used for design. This allows the designers to obtain a quick and proper analysis before the go-ahead to the final step. Recently, CFD approach has been adopted effectively within the automotive industry, with several new methods for car design (Smith, 2008) as well as to the determination of the applied forces and that of the vehicles' wake during moving. CFD also is used to analyze the effect of wake on the vehicle's efficiency and capability in comparison with other cars (Thabet and Thabit, 2018).

Palande and Ashwini, (2016) predicted the drag approach with the help of Reynolds Averaged Naiver Stokes (RANS) formulation with a two-equation model of K-Epsilon turbulence model using CFD produced results that were comparable to the experimental data.

Manimaran, (2015) investigated the airflow over Ahmed's body using the open-source software, Open FOAM to understand the flow pattern on the road during the acceleration and overtaking the vehicle to the right. Also compared the aerodynamic characteristics such as drag and lift coefficients. Computational Fluid Dynamics (CFD) simulations predict the on-road conditions are validated with the experimental results in the wind tunnel. The maximum drag and lift for an Ahmed body vehicle are at higher speeds.

2.10 Wind Tunnel Testing

Wind tunnel testing has the big advantage that once the vehicle model is produced and rigged in the wind tunnel test section, it can quickly provide highly accurate data. Data for different boundary conditions, such as different wind speeds and yaw angles, can be acquired quickly. If similar changes in conditions are done on a computer model, the whole simulation has to be run over again for each case (Selvaraju et al., 2015).

On the other hand, wind tunnel testing can be both highly costly and time-consuming. The wind tunnel itself is a huge investment, and the production of prototypes can be very expensive. Small changes in design will take much more time to implement on a physical prototype than on a computer model. The accuracy of the wind tunnel measurements is affected by several factors, including blockage, scaling effects and the moving road problem, and the reliability and the validity of the data need to be evaluated in each case.

The wind tunnel is used for solving the problem of aeronautical, space, automobile and civil engineering structures, which are best obtained rapidly, economically and accurately by testing the scaled models, and sometimes actual structure in wind tunnels. The size, speed and other environmental conditions of tunnel are determined by actual users, the speed determines the type of the tunnel namely subsonic, near-sonic, transonic, supersonic and hypersonic. While the speeds of these tunnels are obliviously named with reference to the sonic, velocity, the low-speed tunnel which is below 300 mph. An alternative definition of the low-speed tunnel would be the tunnel where the compressibility of air is negligible.

2.11 Turbulence Modeling

Flow fields around bluff bodies, such as the buses can be considered to have extremely turbulent flow patterns. Separation bubbles, boundary layers, and wakes present on bluff bodies are examples of turbulence within a flow field. Reynolds-Averaged Navier–Stokes (RANS) equations combined with turbulence modeling provide an adequate model of turbulent flow effects. The choice of turbulence model will depend on considerations such as the physics encompassed in the flow, the established practice for a specific class of problem, the level of accuracy required, the available computational resources, and the amount of time available for the simulation (Wilcox, 2003).

There are mainly three categories of turbulence models such as Classical Turbulence Models (also known as Reynolds Averaged Navier-Stokes), Direct Numerical Simulation (DNS) and the Large Eddy Simulation (LES). Algebraic (Zero-Equation) Models, One-Equation Models (for example Spalart-Allmaras), Two-Equation Models (k-epsilon, k-omega, SST, etc.) and Second-Order Closure Models all these four types of models are referred to as RANS turbulence models (Wilcox, 2003). Each turbulence models have their own advantage and disadvantage. Understanding their strengths and weaknesses is of paramount importance in order to achieve accurate results from CFD simulations. In this study, the two-equation k-epsilon turbulence model has been chosen for reasons that are explained in the following section.

K-Epsilon Turbulence Model

The K-Ɛ model is the most common turbulence model approach used in the engineering field due to its robustness and accuracy applicable to a wide range of flow at a low computational cost. In this model two transport equations are used to obtain kinetic energy K and dissipation rate Ɛ. ANSYS Fluent offers three turbulence models based on this approach. The Standard K-Ɛ was the first to be introduced and its formulation was based on original work presented by Launder and Spalding (Cable, 2009) following this the RNG K-Ɛ and Realizable K-Ɛ were then introduced. The last two versions aimed at improving the performance of the Standard K-Ɛ.

K-Ɛ Model is able to handle various fluid flow conditions. As it has a simple format, strong performance, and also widely validate. In this model, various improvisations have been conducted which results in better performance also make it more capable to handle various problem with simplicity (Mishra and Aharwal, 2018).

Standard K-Epsilon Turbulence Model

The simplest complete models of turbulence are two-equation models in which the solution of two separate transport equations allows the turbulent velocity and length scales to be independently determined. The standard k-Ɛ model in Fluent falls within this class of turbulence model and has become the workhorse of practical engineering flow calculations in the time since it was proposed by Launder and Spalding (Cable, 2009).

RNG K-Epsilon Turbulence Model

The RNG k-epsilon model was derived using a rigorous statistical technique (called renormalization group theory). It is similar in form to the standard k-Ɛ model, but includes the following refinements (Snegirjov, 2009):

- The RNG model has an additional term in its Ɛ equation that significantly improves the accuracy of rapidly strained flows.
- The effect of swirl on turbulence is included in the RNG model, enhancing accuracy for swirling flows.
- The RNG theory provides an analytical formula for turbulent Prandtl numbers, while the standard K-Ɛ model uses user-specified, constant values.
- While the standard K-Ɛ model is a high-Reynolds-number model, the RNG theory provides an analytically-derived differential formula for effective viscosity that accounts for low Reynolds-number effects. Effective use of this feature does, however, depend on the appropriate treatment of the near-wall region (Yakhot and Orszag, 1986).

Realizable K-Epsilon Turbulence Model

The term realizable means that the model satisfies certain mathematical constraints on the Reynolds stresses, consistent with the physics of turbulent flows. Neither the standard k- Ɛ model nor the RNG k- Ɛ model is realizable. The realizable k- Ɛ model is a relatively recent development and differs from the standard k- Ɛ model in two important ways (Shih et al., 1995):

- The realizable k- Ɛ model contains a new formulation for the turbulent viscosity.
- A new transport equation for the dissipation rate, Ɛ, has been derived from an exact equation for the transport of the mean-square vorticity fluctuation.

Both the realizable and RNG k- Ɛ models have shown substantial improvements over the standard k- Ɛ model where the flow features include strong streamline curvature, vortices, and rotation. Since the model is still relatively new, it is not clear in exactly which instances the realizable k-Ɛ model consistently outperforms the RNG model. However, initial studies have shown that the realizable model provides the best performance of all the k-Ɛ model versions for several validations of separated flows and flows with complex secondary flow features.

K-Omega Turbulence Model

The k-ω model was first proposed by (Wilcox, 2008) and is also a widely implemented turbulence model. Similar to the k-Ɛ model, this is a two-equation model and attempts to predict turbulence by solving PDEs for the kinetic energy k and the specific turbulence dissipation rate ω. It is highly similar to the K-Ɛ model but the small differences lead to a large effect on the difference between turbulence prediction. Compared to the K-Ɛ model, this model gives superior results for boundary layer flows and for flows with higher pressure gradients and where separation occurs. However, its performance for free shear flows is rather poor.

Standard K-Omega Turbulence Model

The standard K-ω model in Fluent is based on the Wilcox K-ω model (Wilcox, 2008) which incorporates modifications for low-Reynolds-number effects, compressibility, and shear flow spreading. The Wilcox model predicts free shear flow spreading rates that are in close agreement with measurements for far wakes, mixing layers, and plane, round, and radial jets, and is thus applicable to wall-bounded flows and free shear flows. A variation of the standard k-ω model called the SST K-ω model is also available in Fluent, and as described below.

SST K-Omega Turbulence Model

This is a two-equation turbulence model developed by (Menter, 1994) with the aim to combine the accuracy of the K-ω model in near-wall condition with the behavior of the K-Ɛ in the far-field. In practice, this is achieved thanks to a blending function that allows the model to work as K-ω close to the wall region and then switch to a modified K-Ɛ model far from the wall region. SST stands for Shear Stress Transport which means that the transport of turbulent shear stress is taken into account when defining the turbulent viscosity.

As has been mentioned the K-Ɛ approach is using wall function while the k-ω needs a refined boundary layer. This phenomenon is called the near-wall approach. The models separately have different grid refinement in order to perform efficiently. The K-Ɛ model doesn’t need too refined mesh only. SST K-ω model is used to predict flow near wall boundaries as it produces good results in such cases. (SST) K-ω model is equivalent to K-Ɛ model in for various flow conditions and produce almost similar results (Mishra and Aharwal, 2018).

2.12 Conclusion from Literature Review

Analysis to reduce the drag coefficient for various vehicles with body modification and different types of add on devices has been carried out using ANSYS Fluent. Most of the literature cited in this work focused mainly on sedans and buses. It is better to conclude that using CFD analysis as design tool at early stage of vehicle body design; tremendous improvement can be done in bus aerodynamics performance, which is still unexplored area. The work uniquely proves the possibility of refining of exterior of a bus for simultaneous improvement in aerodynamics and aesthetics from the point of view of product design. The goal of reducing the aerodynamic drag of bus is a worthy one. It is economically and environmentally valuable because of the reduction of fuel consumption and carbon dioxide emission, respectively.

2.13 Research Gaps

It is found that lot of work had done to reduce drag of race cars, sedans but very little work had done for buses. This study aims to fill this gap by exploring the effect of rear spoiler on aerodynamic drag of the bus.

3. CFD ANALYSIS OF AERODYNAMIC PERFORMANCE OF THE BUS

3.1 Introduction

Aerodynamics analysis mainly carried mainly in two ways such as Computational Fluid Dynamics (CFD) and Experimental analysis by wind tunnel testing. This chapter focused mainly on CFD analysis which was done using ANSYS Fluent and the methodologies employed. A scaled-down model of an Isuzu Midi Bus was designed and constructed, using Computer-Aided Design (CAD) software, SolidWorks was employed for this study. Once the CAD models of the bus, were designed they were imported into the Computational Fluid Dynamics (CFD) ANSYS Fluent. ANSYS Fluent was utilized to perform external fluid flow simulations, predicting the drag coefficient of each bus model. To further reduce computational time required for each simulation the CAD model was scaled down to a 1/20th scaled model. The Reynolds-Averaged Navier-Stokes (RANS) approach was used. The turbulence model was the widely used two-equation model, namely, k-epsilon realizable model with enhanced wall treatment. The steady, pressure-based solver was utilized to achieve steady-state simulations. The process that was taken, for both SolidWorks and Fluent, is outlined in this section. Also, this study involves an investigation of aerodynamic characteristics and optimization of existing Isuzu Midi Bus using CFD methods. Aerodynamic study on this bus was carried out by improving the outer body shape aerodynamically.

3.2. Materials

The materials used in this study were

- Experimental scaled Isuzu Midi Bus model: This is used as a model to investigate the drag force on the wind tunnel.
- Wind Tunnel: Used to validate the obtained computational results experimentally.

The software's used in this study were

- SOLIDWORKS: Used to construct the baseline model of an Isuzu Midi Bus, three modified models and spoiler.

- ANSYS Fluent: Used to simulate the flow around the bus models as well as calculate the drag and lift coefficients.
- Microsoft Excel: Used to draw a graph using the ANSYS calibration corresponding to the input value.

3.3 Existing and Modified CAD Models

3.3.1 Data Collection for Existing Model

Data were gathered to analyze the shape and dimension of Isuzu Midi Bus from Bus bodybuilding companies to construct the SOLIDWORK models with actual dimensions scaled to 1:20. These models can be used in the CFD software to analyze the external shape of the vehicle for the study. A primary factor of aerodynamic drag is due to the frontal area perpendicular to the wind direction. The bus dimensions are mentioned in Table 3.1.

Table 3. 1: Basic Dimension of Isuzu Midi Bus

Parameters	Actual Dimension	Scaled-down 1/20th Dimension
Length	6900 mm	345 mm
Width	2200 mm	110 mm
Height	2970 mm	148.5 mm
Wheelbase	3350 mm	117.5 mm
Minimum Ground Clearance	420 mm	21 mm

The existing Isuzu light truck 2012 model specifications are depicted in Table 3.2, that is the same as the engine, transmission, axle and chassis frame specification of Isuzu Midi Bus.

3.3.2 Bench Marking the Baseline Model

As the existing Isuzu Midi Bus has a flat front it has more resistance to air and hence the drag force is very high and the stability is also very low at a higher speed. In order to overcome these problems, this work comes up with exterior body design keeping the existing model as a benchmark.

Figure 3. 1: Existing Isuzu Midi Bus

From the given data in Table 3.1, the baseline model of an Isuzu midi bus 1/20 scaled-down model was generated using SolidWorks as shown in Figure 3.2. The model was designed with a smooth underbody, enclosed wheel wells, with no side-view mirrors and without openings for cooling airflow.

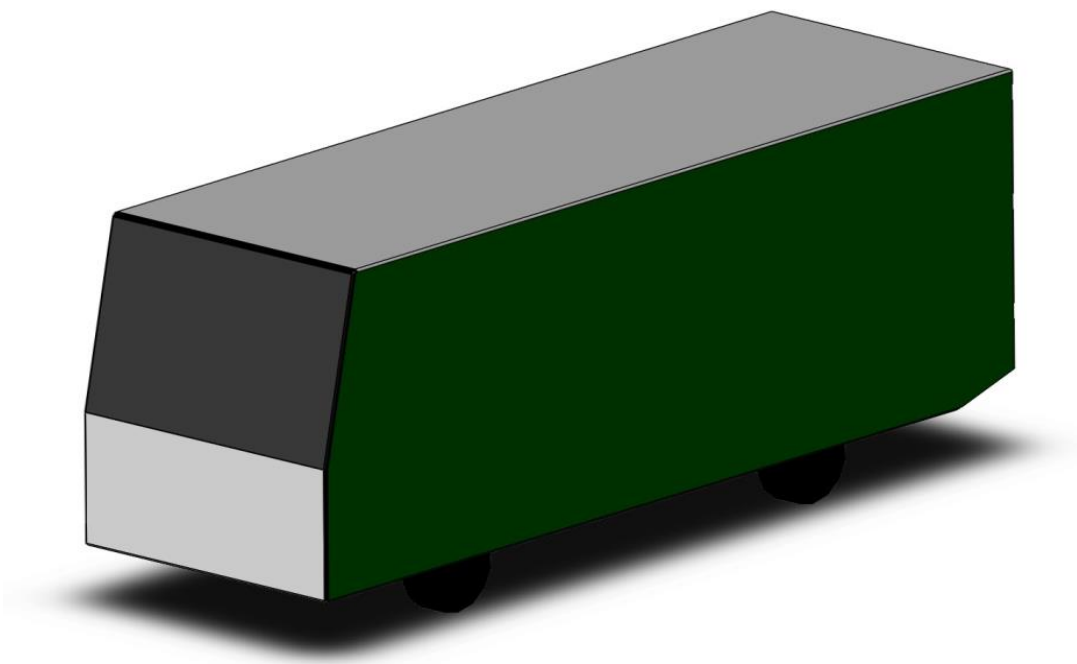

Figure 3. 2: Baseline model of an Isuzu midi bus 1/20 scaled down

Table 3. 2: Isuzu light truck specifications 2012 Model

Engine and Driveline Specifications: ▪ Type: 4 Cylinder 16 valve SOHC ▪ Displacement: 5,193 cc ▪ Bore x Stroke: 115mm x 125mm ▪ Compression ratio: 17.5:1 ▪ Max power: 157 kW (211 HP) @ 2,600 RPM ▪ Max torque: 659 Nm (486 lb. ft) @ 1,600 RPM ▪ Fuel injection: Direct injection high pressure common rail system.	**Axles**: Front: Isuzu F041 ▪ Reverse Elliot I-beam. 4,100 kg capacity. Rear: Isuzu R077 ▪ Full floating Banjo type. 7,700 kg capacity. ▪ Drive ratio: 5.125:1 **Fuel Tank**: ▪ Frame mounted 200L steel fuel tank. ▪ Lockable fuel cap.
Transmission: ▪ Synchromesh on gears 2-6. Triple cone synchromesh on 2^{nd} and 3^{rd} gears. Integral oil pump provides full pressure lubrication. ▪ Gear ratios (:1) 1^{st} 6.615 2^{nd} 4.095 3^{rd} 2.358 4^{th} 1.531 5^{th} 1.000 6^{th} 0.722 Rev 6.615	**Chassis Frame:** ▪ Cold rivetted ladder frame with parallel side rails. HT540A high tensile weldable steel side members. Chassis Frame dimensions: - Side rail (mm): 225 x 70 x 6.0 - Rear frame width (mm): 840 **Standard model**: ▪ 6 speed, manual with air assisted shift.

Then the designed model is imported into the ANSYS Fluent to do the simulation of the coefficients of drag and lift in the wind tunnel which is generated in the design module of the ANSYS Fluent. Isuzu midi bus was chosen for this study, it should be noted that the SolidWorks model used was not an exact replica of the bus, but it is an approximate model.

Criteria for selecting an Isuzu midi bus (Baseline model)

- The light truck Isuzu imported from Japan but it's modified to an Isuzu midi bus by changing the vehicle's outer body without chassis layout here in Ethiopia at different Bus bodybuilding companies and Garages.
- The Bus bodybuilding companies prioritize the exterior looks of the bus and ignore the aerodynamic aspect. The bus has a poor aerodynamic shape which is almost rectangular blunt, which has high drag resistance force these leads to increased fuel consumption.
- It is the most popular bus in Ethiopia, many public means of transport on urban and rural areas of Ethiopia are using this bus; these vehicles make many trips to different parts of the country.

3.3.3 Modified CAD Models

This study prepared four modified bus models, each having different exterior body styling and appearance. The baseline model (Figure 3.2) is the standard model that has a flat front surface and sharp corners. Hence, it has more resistance to air which raises the drag force which leads to more fuel consumption and emission. The first bus model "Model one" (Figure 3.3) designed with its front surface tapering more towards the rear end. The second bus model "Model two" (Figure 3.4) designed with a curved front surface and smooth rounded corners on front and rear end of the roof. The third bus model (Figure 3.5) designed with a more curved front surface and more smooth rounded corners on front and rear end of the roof. The fourth bus model designed with the same as the third bus model with rear spoiler at rear end of the roof as shown in Figure 3.6.

Model one (Figure 3.3) designed with its front surface tapering more towards the rear end. Also designed with smooth rounded corners instead of sharp corners. This model was similar to the baseline model but different in inclination angle of the windshield, the inclination angle of the baseline model was 11.31º whereas the inclination angle of model one was 15.64º, detailed drawing of the model depicted in Appendix A.

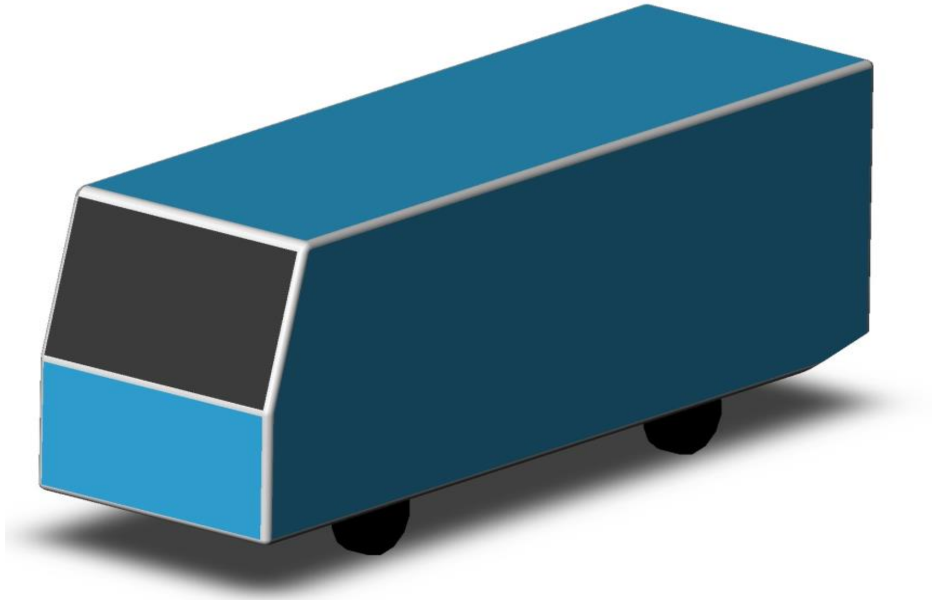

Figure 3. 3: Model I: CAD model of Isuzu midi bus with tapered front surface towards the rear.

Model two (Figure 3.4) designed with a curved front surface and smooth rounded corners on the front and rear end of the roof. Modification is done in the front and rear end of the roof based on the results from baseline model.

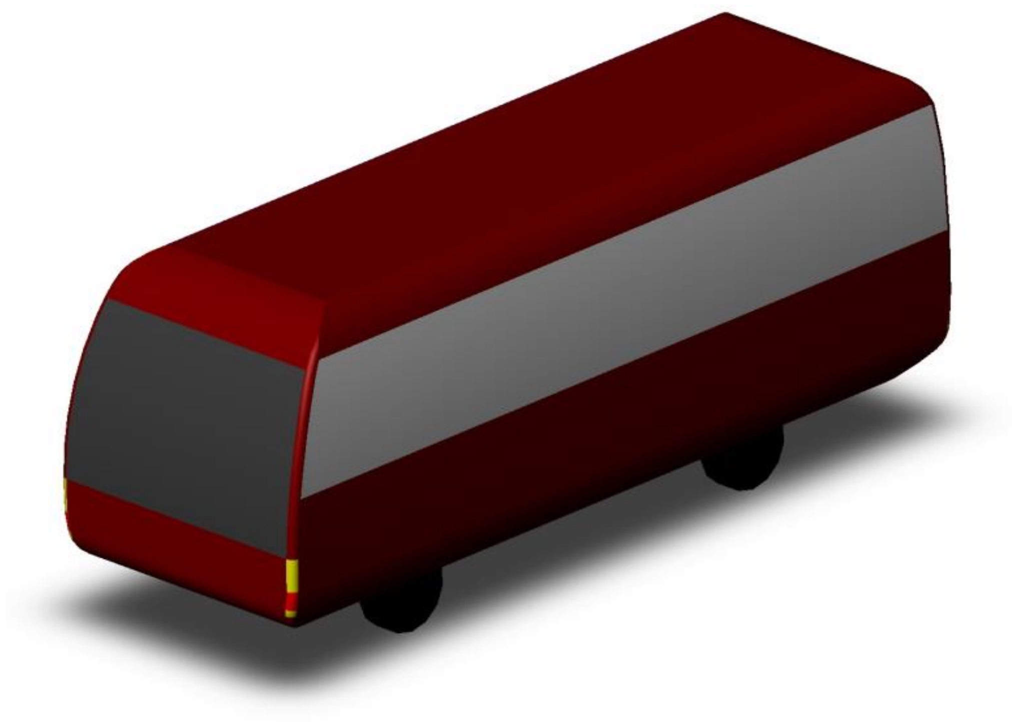

Figure 3. 4: Model II: CAD model of an Isuzu midi bus with a curved front surface and round corners on roof ends.

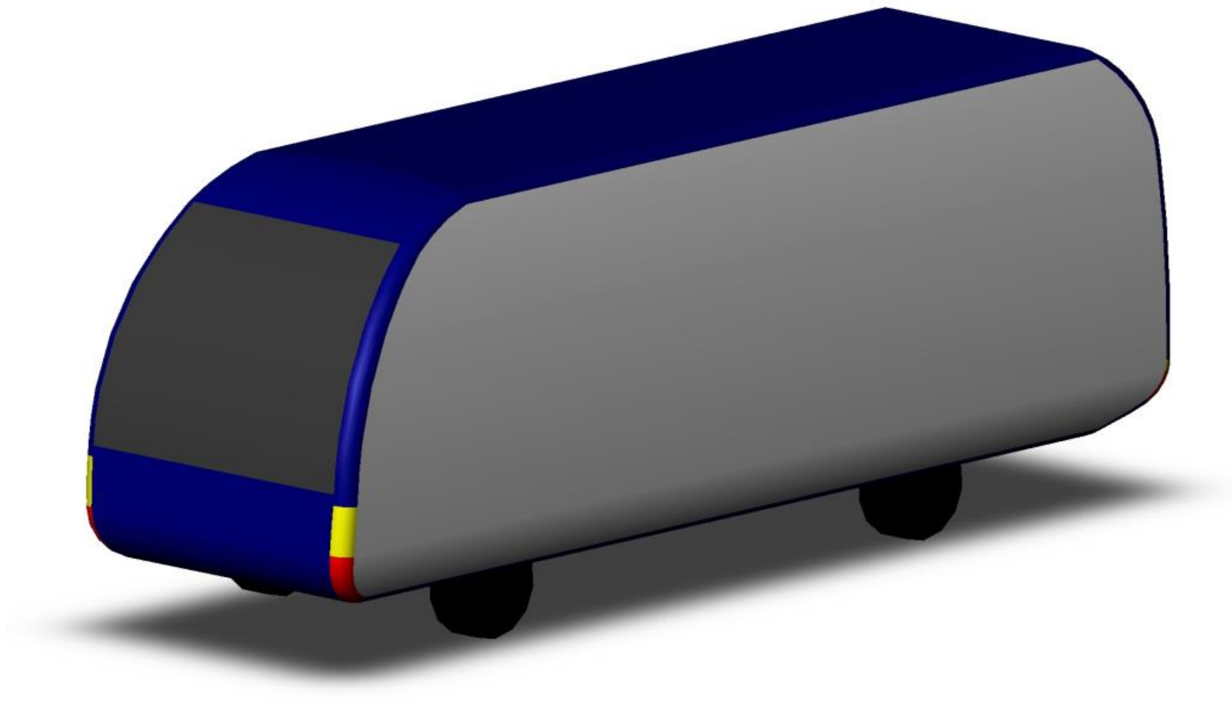

Figure 3. 5: Model III: CAD model with a more curved front surface and round corners.

Model three designed with a more curved front surface and more smooth rounded corners on the front and rear end of the roof than other models as shown in Figure 3.5.

3.3.4 Using Aerodynamic Drag Redaction Device

In this study rear spoiler used as a drag-reducing device which is added on model three at rear roof end and simulated using Ansys Fluent and the results are compared with other models. Rear spoiler which is externally attached to the rear end of the roof, is meant to push the flow separation a bit rearward and reduce the amount of drag by minimizing the wake region, and by throwing the turbulent air behind the bus. Multiview drawing of Model one, Model two, Model three and Rear Spoiler is depicted briefly in appendix A.

The spoiler airfoil shape was selected from NACA catalog. NACA 4412 airfoil was selected and the coordinates are imported to SolidWorks for modeling. Then to increase its length rectangular feature was added and connected with Model three. The main criteria for selecting NACA 4412 airfoil was, becomes it’s more efficient for practical application and has lower drag and lift coefficients (Muhammad et al., 2014).

Normally spoilers are designed for vehicle to reduce aerodynamic drag, to create localized force and aesthetics. Spoiler will be simplest type of modification as they can be attached to current models on-road vehicles.

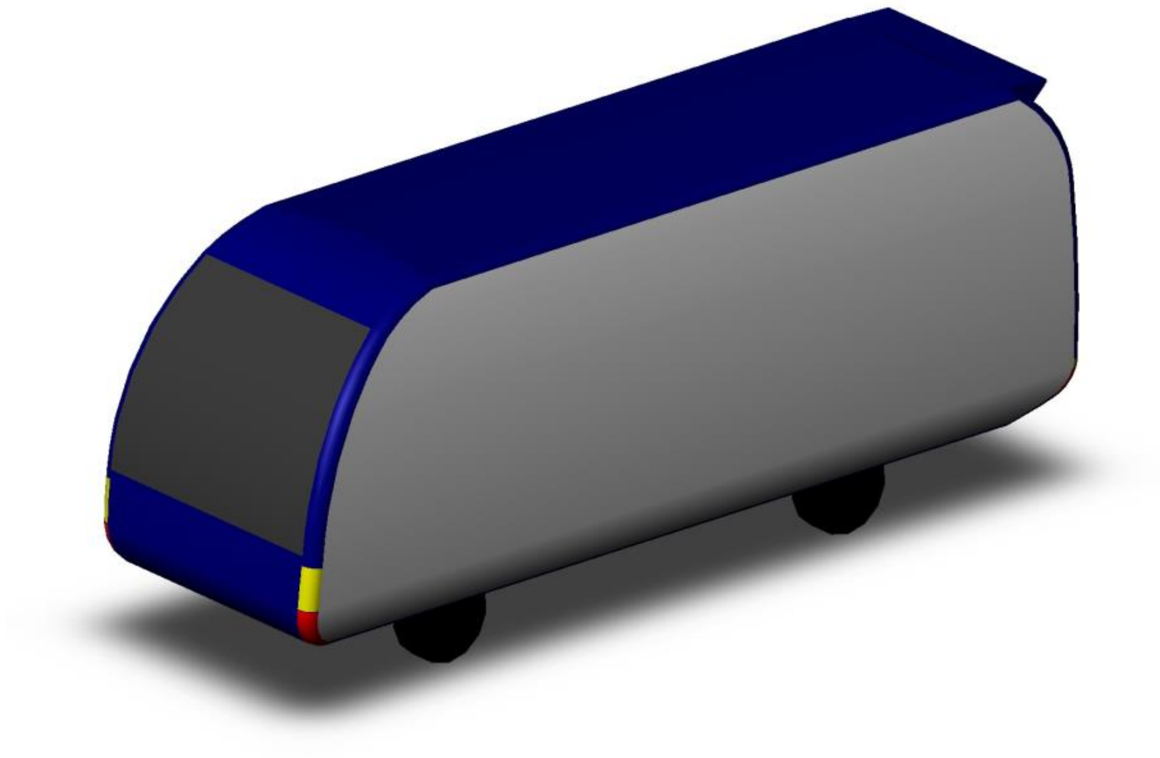

Figure 3. 6: Model IV: CAD Model III with rear spoiler.

3.4 Drag and Lift Forces

Drag is the most significant force that occurs when air motion around a solid body is studied. Drag is important in a way that it directly opposes the direction of the body and a great amount of energy and power is required to overcome it, causing it to be a highly undesirable force. Automotive manufacturers try to factor in this force when designing automobiles. Drag force affecting a body in motion is usually calculated and represented by using a value called the drag coefficient (C_d). The drag coefficient has no unit. Forces that affect drag include the air pressure against the face of the object, the friction along the sides of the object and the relatively negative pressure, or suction, on the back of the object. Usually, there are two types of drag that are commonly mentioned. They are pressure drag and skin friction drag.

Drag coefficient (C_d) is used to compare aerodynamic drag produced by vehicles and is dependent on the shape of the vehicle, the frontal projected area A, and the speed at which the vehicle is traveling V (Barnard, 2009). The relationship between drag and these factors can be expressed by:

$$C_d = \frac{2F_d}{\rho A V^2} \quad (3.1)$$

The perpendicular component of the acting load is the lift, which is basically generated by the pressure difference between the upper and lower surface of the body involved in the flow. Similarly to the drag, the lift can be expressed by a dimensionless coefficient (Barnard, 2009). The lift coefficient (C_l) is defined in a similar way to drag coefficient:

$$C_l = \frac{2F_l}{\rho A V^2} \quad (3.2)$$

Where A is the projected frontal area, ρ is the density of the air, V is the speed of the vehicle relative to the air and F_l is the lift force. The downforce is an essential property in the high-performance vehicles. Greater downforce increases the turning speed, acceleration, and stability conditions improve braking performance.

3.5 Fuel Economy Calculations

Specific fuel consumption (Siddhesh, 2017) was based on the torque delivered by the engine in respect to the fuel mass flow delivered to the engine. It's measured after all parasitic engine losses is brake specific fuel consumption (bsfc) and measuring specific fuel consumption based on the in-cylinder pressures (ability of the pressure to do work) is indicated specific fuel consumption (isfc).

$$bsfc = \frac{m_f'}{W_b'} \quad (3.3)$$

$$isfc = \frac{m_f'}{W_i'} \quad (3.4)$$

Where m_f' represents the fuel consumption in grams per minute, W_b' is brake power and W_i' denoted the indicated power.

The fuel economy of a vehicle can be related to the specific fuel consumption by the vehicle engine and the power required for the vehicle to move at a constant velocity V as follows:

$$Power = \frac{F_d \times V}{0.65} = \frac{0.5\,\rho V^2 A C_d \times V}{0.65} \quad \text{(3.5)}$$

To overcome the aerodynamic resistance at 100 kmph about 65% of power of vehicle is consumed. The specific fuel consumption is defined as the mass of fuel consumed per hour, in order to develop a brake power of one kilowatt.

bsfc is expressed in terms of gallons.

$$bsfc_v = {}^{bsfc}/_{\rho_{fuel}} \quad \text{(3.6)}$$

${}^{1}/_{bsfc_v}$, is the energy produced by the engine per one gallon of fuel and is related to the total power required and the fuel economy in MPG.

$$\frac{Power}{V} \times MPG = {}^{1}/_{bsfc_v} \quad \text{(3.7)}$$

MPG is expressed in terms of $bsfc_v$ and C_d:

$$MPG = \frac{1.3}{bsfc_v \times \rho V^2 A C_d} \quad \text{(3.8)}$$

The drag coefficients of a baseline model with other modified models are compared using equation:.

$$C_{d\,Modified} = (1 - RR) C_{d\,baseline} \quad \text{(3.9)}$$

Where, RR is the drag reduction of modified model from a baseline model.

3.6 Numerical Method

In the scope of this study, CFD simulations are performed in order to verify the simplified aerodynamic solver. CFD is extensively used for analysis and design of engineering applications and is a branch of fluid mechanics that numerically solves and analyzes problems involving fluid flows (Cengel and Cimbala, 2017). Some of these numerical methods are finite element, finite difference, and finite volume methods that are using spatial and time discretization. The goal of any CFD simulation is to study details of a particular fluid dynamics phenomenon in a controlled environment. In this section, the governing equations of fluid dynamics and turbulence modeling are presented.

3.6.1 Mathematical Model of Fluid Dynamics

The starting point of any numerical method is a mathematical model, i.e. the set of the governing equations of fluid dynamics along with the boundary conditions (Ferziger and Peric, 2002). These fundamental governing equations form the cornerstones of every CFD model. The Fluent program solves the general integral equations for continuity, momentum, energy, turbulence using the finite volume method. Continuity and momentum equations are used in solving the finite volumes with computational flow dynamics (CFD). In practice, it is difficult to solve these equations analytically. The governing equations that are used in fluid mechanics are the conservation equations known as Navier-Stokes equations. These basically represent the laws for mass, momentum and energy conservation. Using these equations, the solver calculates the velocity and the pressure distribution which is then used to calculate the drag and lift forces.

Depending on the type of flow in each specific case, these equations take a different form. In the case that is examined here the flow is turbulent, incompressible viscous flow of a Newtonian fluid (air). The general form of the Continuity equation and Navier-Stokes equations are discussed briefly below.

The continuity equation:

$$\frac{\partial}{\partial x}(\rho u) + \frac{\partial}{\partial y}(\rho v) + \frac{\partial}{\partial z}(\rho w) = 0 \quad \ldots\ldots\ldots\ldots\ldots\ldots\ldots\ldots\ldots\ldots (3.10)$$

Conservation of linear momentum (Navier-stokes) equation is Newton's second law of motion which relates pressure, momentum and viscous forces. This set of formulas are referred to as the incompressible Navier-Stokes equations which are non-linear partial differential equations:

x-component of the momentum equation:

$$\frac{\partial}{\partial t}(\rho u) + \frac{\partial}{\partial x}(\rho u u) + \frac{\partial}{\partial y}(\rho v u) + \frac{\partial}{\partial z}(\rho w u) = -\frac{\partial P}{\partial x} + \mu\left(\frac{\partial^2 u}{\partial x^2} + \frac{\partial^2 u}{\partial y^2} + \frac{\partial^2 u}{\partial z^2}\right) \ldots\ldots\ldots (3.11)$$

y-component of the momentum equation:

$$\frac{\partial}{\partial t}(\rho v) + \frac{\partial}{\partial x}(\rho u v) + \frac{\partial}{\partial y}(\rho v v) + \frac{\partial}{\partial z}(\rho w v) = -\frac{\partial P}{\partial y} + \mu\left(\frac{\partial^2 v}{\partial x^2} + \frac{\partial^2 v}{\partial y^2} + \frac{\partial^2 v}{\partial z^2}\right) - \rho g \beta (T_\infty - T) \quad \text{……… (3.12)}$$

z-component of the momentum equation:

$$\frac{\partial}{\partial t}(\rho w) + \frac{\partial}{\partial x}(\rho u w) + \frac{\partial}{\partial y}(\rho v w) + \frac{\partial}{\partial z}(\rho w w) = -\frac{\partial P}{\partial z} + \mu\left(\frac{\partial^2 w}{\partial x^2} + \frac{\partial^2 w}{\partial y^2} + \frac{\partial^2 w}{\partial z^2}\right) \text{……... (3.13)}$$

Where (u, v, w) is velocity component of in the x, y, and z-direction, respectively.
ρ density of the fluid, μ is the viscosity and β is the thermal expansion coefficient of air, t time, T is the temperature, P is the pressure, g is the gravitational acceleration and (x, y, z) is position of the fluid component.

Conservation of energy is the first law of thermodynamics stated that the total amount of energy within the system stays constant. The conservation of energy equation is:

$$\frac{\partial}{\partial t}(\rho C_p T) + \frac{\partial}{\partial x}(\rho u C_p T) + \frac{\partial}{\partial y}(\rho v C_p T) + \frac{\partial}{\partial z}(\rho w C_p T) = K\left(\frac{\partial^2 T}{\partial x^2} + \frac{\partial^2 T}{\partial y^2} + \frac{\partial^2 T}{\partial z^2}\right) + q''' \text{…. (3.14)}$$

Where C_p is the specific heat (J/kg K), and K is the conductivity (W/m K) of the fluid and q''' is the rate of internal heat generation per unit volume.

3.6.2 Turbulence Modeling

Aerodynamic evaluation of airflow over an object can be performed using an analytical method or CFD approach. On one hand, the analytical method of solving airflow over an object can be done only for simple flows over simple geometries like laminar flow over a flat plate. If airflow gets complex as inflows over a bluff body, the flow becomes turbulent and it is impossible to solve Navier-Stokes and continuity equations analytically. On the other hand, obtaining direct numerical solution of Navier-stoke equation is not yet possible even with modern-day computers. In order to come up with reasonable solution, a time-averaged Navier-Stokes equation is being used Reynolds Averaged Navier-Stokes Equations (RANS) together with turbulent models to resolve the issue involving Reynolds stress resulting from the time-averaging process. In this study Realizable k-ε Turbulence Model (RKE) described in section 2.11 was used. The solver used for the analysis was ANSYS 17.0 and it uses a control-volume method to solve the governing equations that can be solved numerically. The term “realizable” means that the model satisfies certain mathematical constraints on the Reynolds stresses, consistent with the physics of turbulent flows. Neither the standard k-ε model nor the RNG k-ε model is realizable.

ANSYS fluent solver based on pressure was used for this study. It was a steady analysis with absolute velocity formulation. Reynolds-Averaged Naiver-Stokes equations are solved for simulating an incompressible turbulent flow. The selection of a viscous model is tough in external flow analysis. A standard k-ε model is generally used due to its strength and easy convergence. Since it is not recommended for external geometry with flow separation (Siddhesh et al., 2017), the realizable k-ε model with non-equilibrium wall functions is used for this analysis. This k-ε turbulence model is very robust, having reasonable computational turnaround time, and widely used by the automotive industry. Also, the realizable model provides the best performance of all the k-ε model versions for several validations of separated flows and flows with complex secondary flow features (Bansal and Sharma, 2014).

In terms of the improved changes the transport equations become (Shih, 1995):

$$\frac{\partial}{\partial t}(\rho k) + \frac{\partial}{\partial x_j}(\rho k u_j) = \frac{\partial}{\partial x_j}\left[(\mu + \frac{\mu_t}{\sigma_k})\frac{\partial k}{\partial x_j}\right] + G_k + G_b - \rho\epsilon - Y_m + S_k \text{……… (3.15)}$$

$$\frac{\partial}{\partial t}(\rho\epsilon) + \frac{\partial}{\partial x_j}(\rho\varepsilon u_j) = \frac{\partial}{\partial x_j}\left[(\mu + \frac{\mu_t}{\sigma_\varepsilon})\frac{\partial \varepsilon}{\partial x_j}\right] + \rho S\varepsilon C_1 - \rho C_2\frac{\varepsilon}{k+\sqrt{v\varepsilon}} + C_{1\varepsilon}\frac{\varepsilon}{k}C_{3\varepsilon}G_b + S_\varepsilon \text{… (3.16)}$$

Where G_k represents the generation of turbulent kinetic energy the arises due to mean velocity gradients, G_b is the generation of turbulent kinetic energy the arises due to buoyancy, and Y_m represents the fluctuating dilation incompressible turbulence that contributes to the overall dissipation rate. S_ε and S_k are source terms defined by the user. $\alpha_k and\ \alpha_\varepsilon$ are the turbulent Prandtl numbers for the turbulent kinetic energy and its dissipation.

The turbulent viscosity is determined by the formula given below; however, it produces different results as C_μ is not constant.

$$\mu_t = \rho C_\mu \frac{k^2}{\varepsilon} \text{………………………………………… (3.17)}$$

Where C_μ is computed from

$$C_\mu = \frac{1}{A_0 + A_s \frac{KU^*}{\varepsilon}} \quad (3.18)$$

Where,

$$U^* = \sqrt{S_{ij}S_{ij} + \widetilde{\Omega_{ij}}\widetilde{\Omega_{ij}}} \text{ and } \widetilde{\Omega_{ij}} = \overline{\Omega_{ij}} - \varepsilon_{ijk}\omega_k - 2\varepsilon_{ijk}\omega_k \quad (3.19)$$

In the equation (3.10), $\overline{\Omega_{ij}}$ is the mean rate of rotation tensor viewed in a rotating reference frame with angular velocity ω_k. The constants A_0 *and* A_s are defined as;

$$A_0 = 4.04\,, A_s = \sqrt{6}cos\phi \quad (3.20)$$

Where

$$\phi = \frac{1}{3}cos^{-1}\left(\sqrt{6}\,\frac{S_{ij}S_{jk}S_{ki}}{\tilde{S}^3}\right), \tilde{S} = \sqrt{S_{ij}S_{ij}}\,, S_{ij} = \frac{1}{2}\left(\frac{\partial u_j}{\partial x_i} + \frac{\partial u_i}{\partial x_j}\right) \quad (3.21)$$

It has been shown that C_μ is a function of the mean strain and rotational rates, the angular velocity of the rotating system, and the turbulent kinetic energy and its dissipation rate. The standard value of C_μ =0.09 is found to be the solution of equation (3.9) for an inertial sub-layer in the equilibrium boundary layer.

The constants $C_{1\varepsilon}, C_2, \alpha_k and\ \alpha_\varepsilon$ have been determined by Shih, (1995) and are defined as follows.

$C_{1\varepsilon} = 1.44, C_2 = 1.9, \quad \alpha_k = 1.0 and\ \alpha_\varepsilon = 1.2.$

3.7 ANSYS Fluent Setup and Procedure

Computational fluid dynamics (CFD) is the branch of fluid dynamics providing a cost-effective means of simulating real flows by the numerical solution of the governing equations. ANSYS Fluent used as the CFD software, to simulate the fluid flow around the CAD models which were generated using SolidWorks. A CFD methodology followed in this study and each step of the procedure is shown in Figure 3.7. The simulation process was the same for all different SolidWorks models. There are three steps involved in a typical CFD simulation. The three steps are

- Pre-Processor Stage
- Solver Stage
- Post-Process Stage

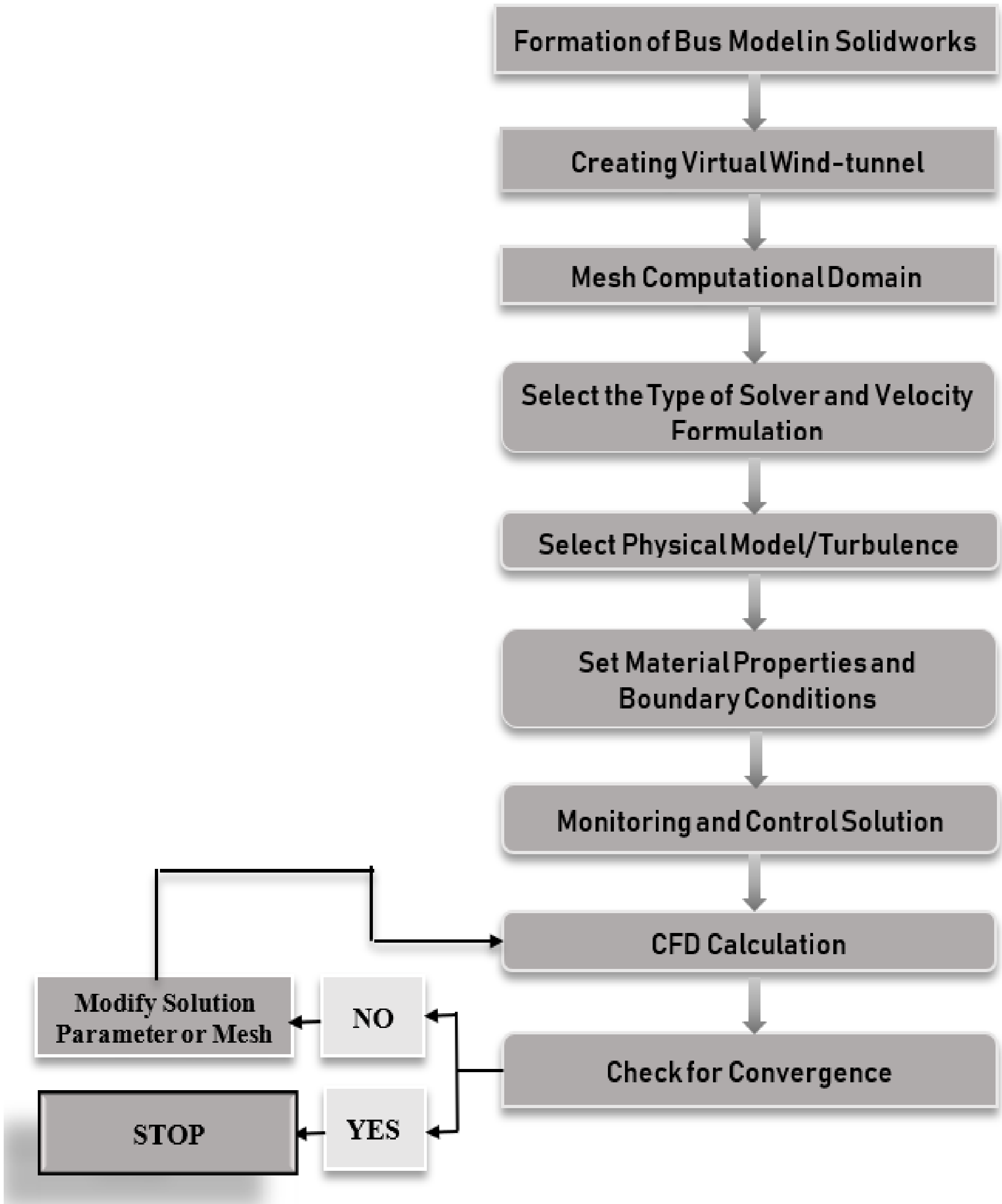

Figure 3. 7: An overview of the CFD solution procedure

3.7.1 Pre-Processor Stage

Pre-Processor consists of input of a flow problem by means of a user-friendly interface and subsequent transformation of this input into a form of suitable for the use by the solver. The pre-processor is the link between the user and the solver. In this stage, CFD users are needed to provide sufficient input to the computer in order to obtain the desired output. The pre-processing stage is divided into several steps such as Geometry generation, Boundary condition input, Mesh generation, Selecting flow type (Steady/Unsteady), Turbulence and Near wall model input.

3.7.1.1 Geometry Generation

The simplified baseline model of an Isuzu midi bus is designed in SolidWorks as shown in Figure 3.8. The sizes of the midi bus model are 345 mm long, 110 mm wide, 148.5 mm high and wheelbase of 117.5 mm. The main simplifications are eliminating small parts, wheel frames, small details and gaps in the vehicle body for the purpose of the analysis. Thereafter, this model has been analyzed for drag and lift coefficients under the ANSYS (Fluent).

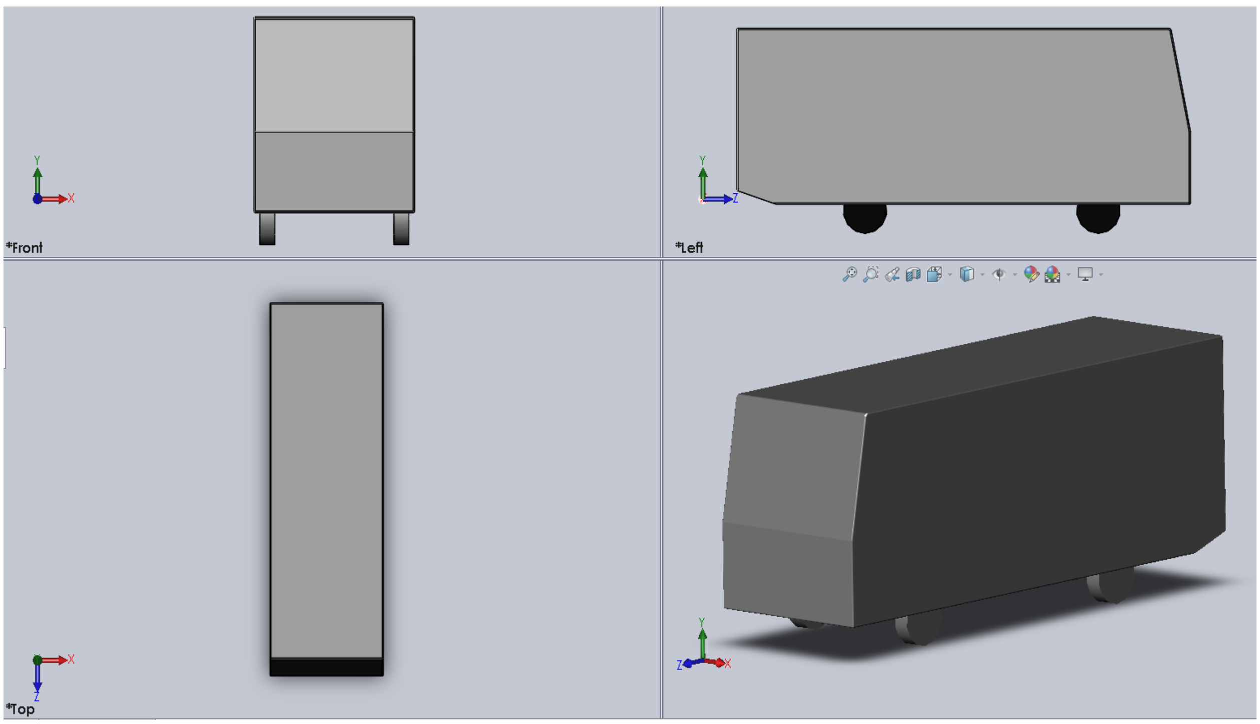

Figure 3. 8: An Existing model with simplification

3.7.1.2. Design of Virtual Wind Tunnel

After the vehicle model has been uploaded into the ANSYS environment an enclosure was generated surrounding it. For the experimental study, the enclosure was designed based on recommendation from Fluent for accurate results. A virtual air-box (Figure 3.9) has been created around the 3D CAD model which represents the wind tunnel in real life. The measurements of the tunnel are relational to the bus. A virtual wind tunnel contains an inlet, an outlet, wall, and a ground surface. The flow inlet plane was located three car lengths away from the front of the car body, whereas the outlet plane five car lengths from the rear.

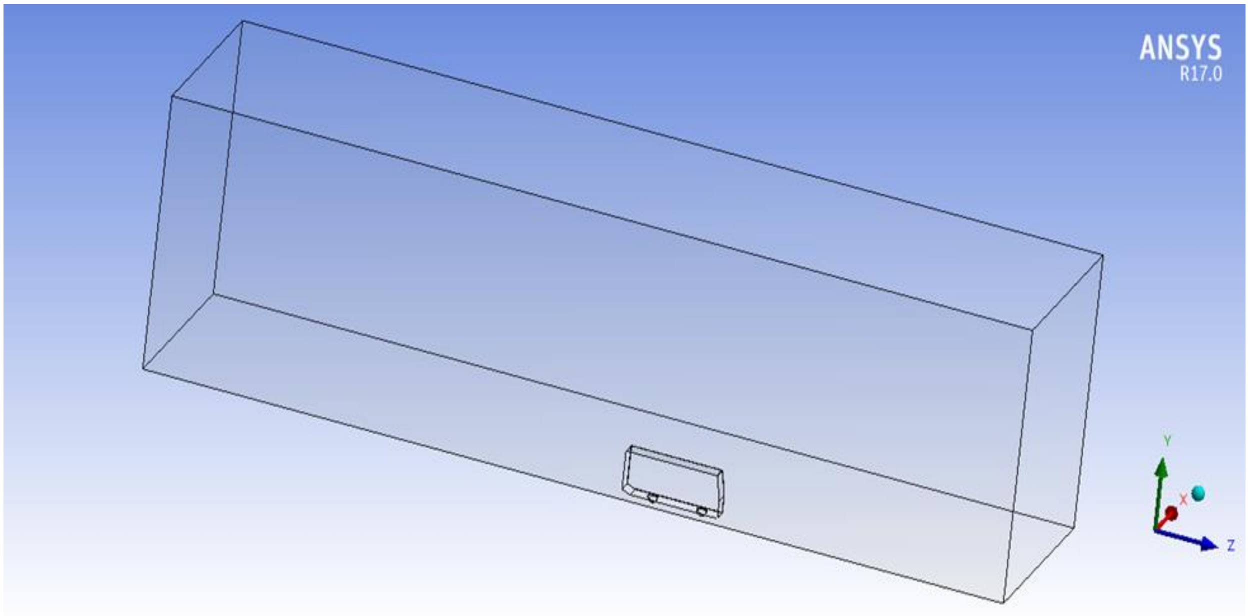

Figure 3. 9: Virtual wind tunnel targeted for CFD simulation.

The side plane was located sufficiently far from the car body side surface (about two car lengths), providing a vast simulation domain. The height of the domain was set to two times the length of the car body (Abdulkareem et al, 2018). Dimensions used for the enclosure are given in Table 3.3. The ground was located at the distance 0.0001 m from the car body bottom surface. The rear side of vehicle is more interested because, which is the place where the "wake of vehicle" phenomenon occurs, more space has been left in the rear side of the vehicle model to capture the flow behavior mostly behind the vehicle.

Due to the complexity of the simulation with limited computer resources and time, the complete domain was divided into half using a symmetry plane (YZ plane), which means, the simulation would be calculated for just the one side of the vehicle model. Since the other side is symmetric and the YZ plane has been defined as symmetric boundary in the solver to make the boundary condition as "a slip wall with zero shear forces"; the simulation results would be valid for full model as well.

The assumptions made in the present simulation have the airflow steady state with constant velocity at inlet and with zero-degree yaw angle, constant pressure outlet, no-slip wall boundary conditions at the vehicle surfaces, and inviscid flow wall boundary condition on the top, sidewalls, and ground face of the virtual wind tunnel.

Table 3. 3: Dimension for wind tunnel enclosure

Upstream length	Downstream length	Width	Height
1035 mm	1725 mm	690 mm	690 mm

After the wind tunnel enclosure was constructed the Boolean feature was employed to subtract the volume of the bus from the volume of an enclosure to create a new volume that represented only the air that surrounded the bus.

3.7.1.3 Mesh Generation

Mesh generation constitutes one of the most important steps during the preprocessing stage after the definition of the domain geometry. The mesh is produced on the design of the bus and on the surface of the domain as shown in Figure 3.10 and 3.11. The type of mesh used to discretize the computational domain as tetrahedrons. The mesh established for the surface bodies had as base format the triangular mesh.

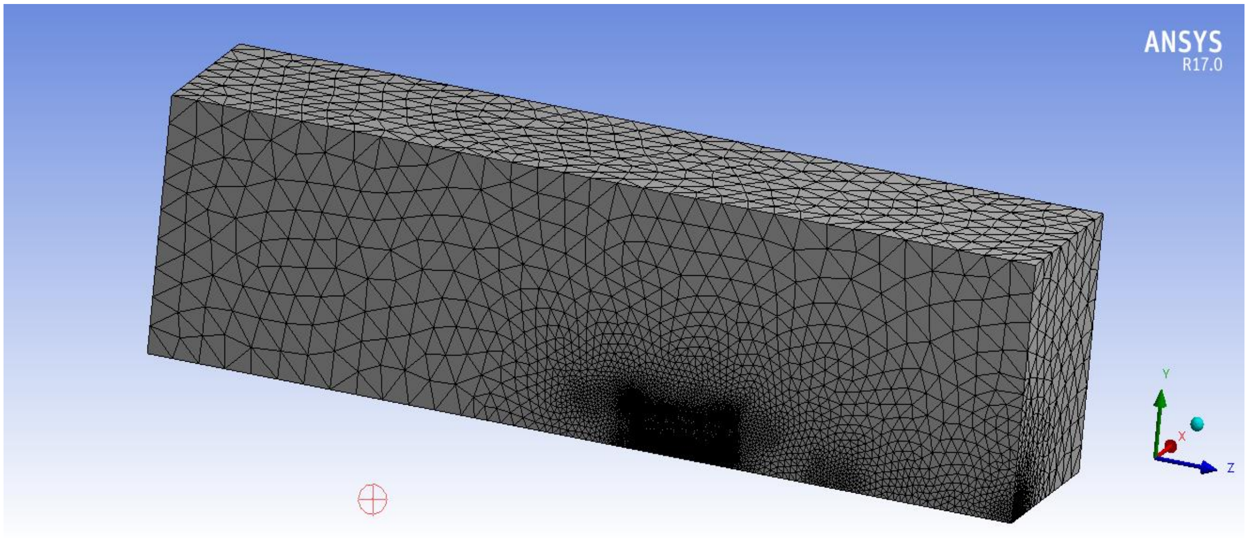

Figure 3. 10: Mesh after surface sizing (Baseline model)

A fine mesh is necessary in order to have a converging simulation. The fineness of the entire mesh is described by relevance used. The relevance of 100 means high accuracy and low speed of processing, while a relevance of -100 means low accuracy and higher speed of processing. For this study zero relevance with fine relevance, the center was used. The advanced size function is proximity and curvature, used for the progression from minimum size elements, near and around the curvature of the vehicle to maximum size elements far away from the vehicle toward the walls of the wind tunnel box.

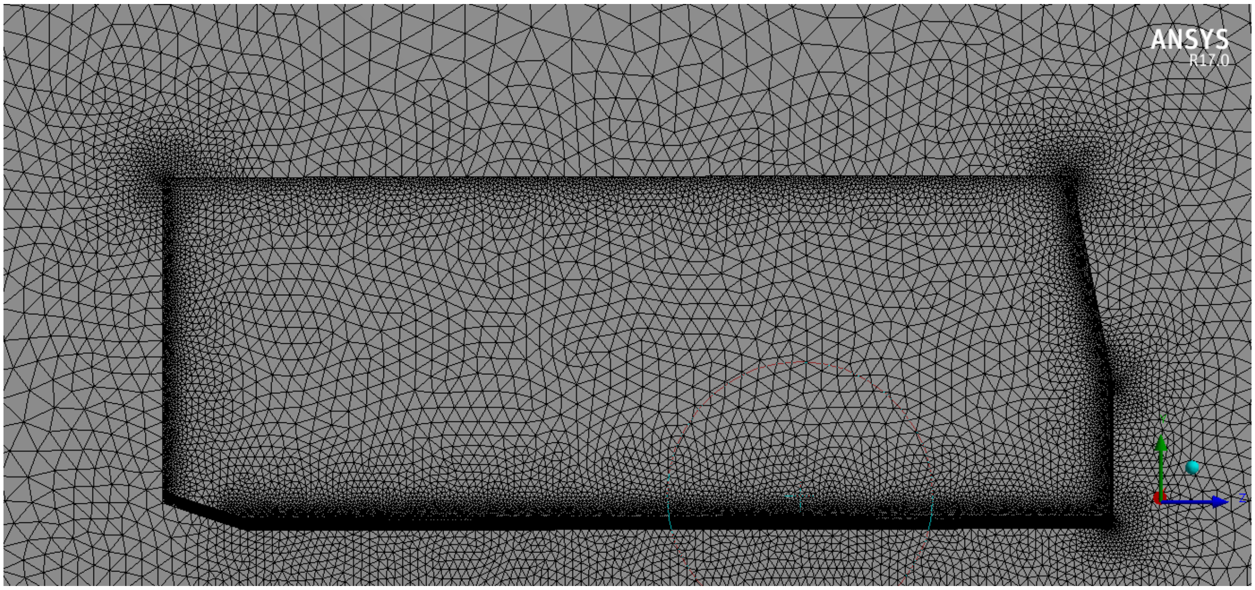

Figure 3. 11: Zoom of the mesh after surface sizing (Baseline model)

High smoothing which increases the number of smoothing iterations and improving element quality by moving nodes and elements in the vicinity was used. Detailed meshing inputs are mentioned in Appendix C.

Named sections were created to differentiate among the faces, which is also used to establish the properties of each face. The plane in front of the vehicle was the velocity inlet while the plane behind was the pressure outlet. The side attached to the vehicle is the symmetry whereas the side far from the vehicle was named symmetry-side. The top face was named symmetry-top and the bottom face road. Since the symmetry top and symmetry side surfaces of the car-box were far away from the vehicle and have no influence on the vehicle at all, which was for not because they were symmetric but to give them the same boundary conditions as symmetric surface (which is slip wall with zero shear forces).

The ground surface and the car surfaces are specified to be included in the inflation creation. The inflation on the mesh is the creation of a mesh layer for the boundary layer simulation on the surfaces of the car and the ground as shown in Figure 3.12 and 3.13. It will create triangular prism elements along with the boundary layer and will keep the rest of the control volume with the tetrahedron elements. The inflation applied is program-controlled and the default values proposed by Seibert et al., (2002) are good enough to perform the simulations. The maximum layer thickness is 5 mm, the growth factor of 20% and one maximum of 5 levels**.**

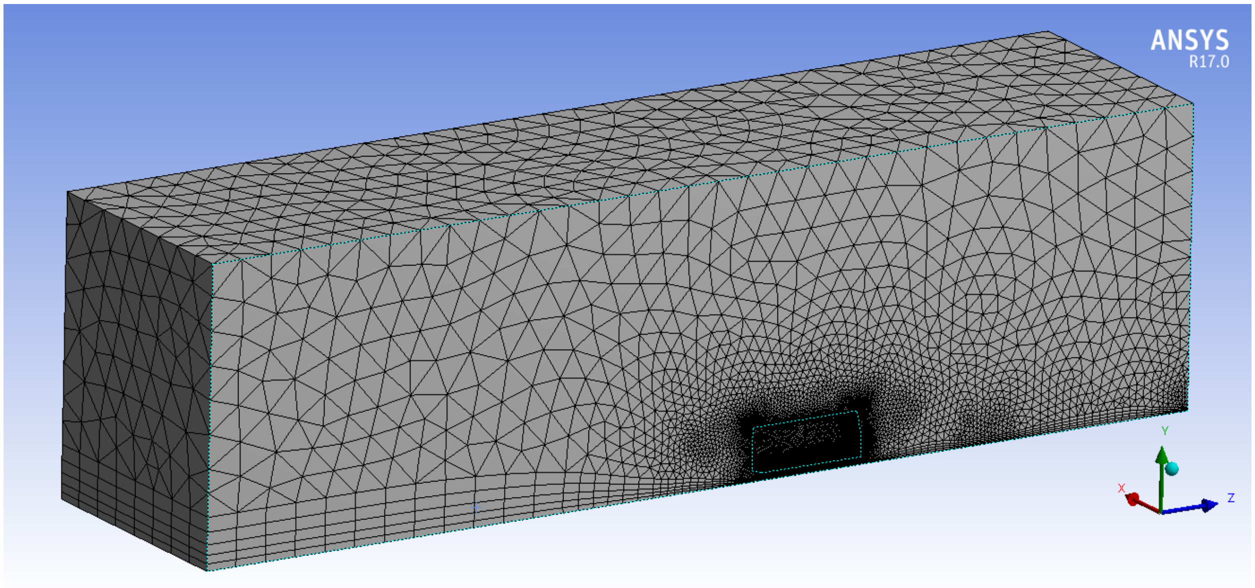

Figure 3. 12: Mesh after inflation of the baseline model

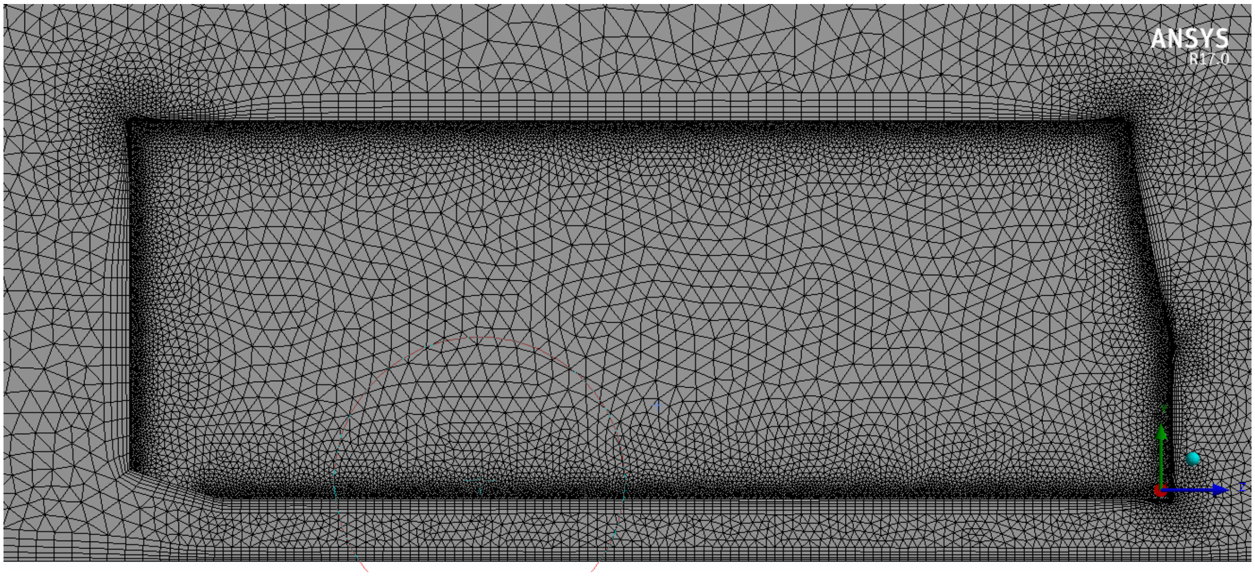

Figure 3. 13: Zoom of the mesh after inflation of the baseline model

Now it's time for mesh refinement. The purpose of mesh refining is to modify the density of elements inside the control volume. The objective is to have more accuracy on the calculations (and hence more density of elements) on the areas where the fluid flow is in contact with the car body relevant surfaces. It's not interesting to have a great resolution in the far-field for example Velocity inlet and Pressure outlet areas. The strategy for mesh refining chosen for this work is based on internal boxes created around the vehicle and in the wake region to explicitly control mesh size. This approach is more time consuming than other strategies but is very accurate. The boxes are created in the Preprocessing tool. A constant size of surface elements is applied to the box walls. The boxes are used as meshing domains, in which cell size can be controlled in a very comfortable way. For mesh refining, three boxes have been done to increase the mesh density in the areas of interest.

First box, called car-box. It refines the control volume on the surroundings of all the car surfaces in 0.5L on the front of the car, 1L on the rear of the car and 0.5L on the top of the car, where L is the car length as shown below in Figure 3.14.

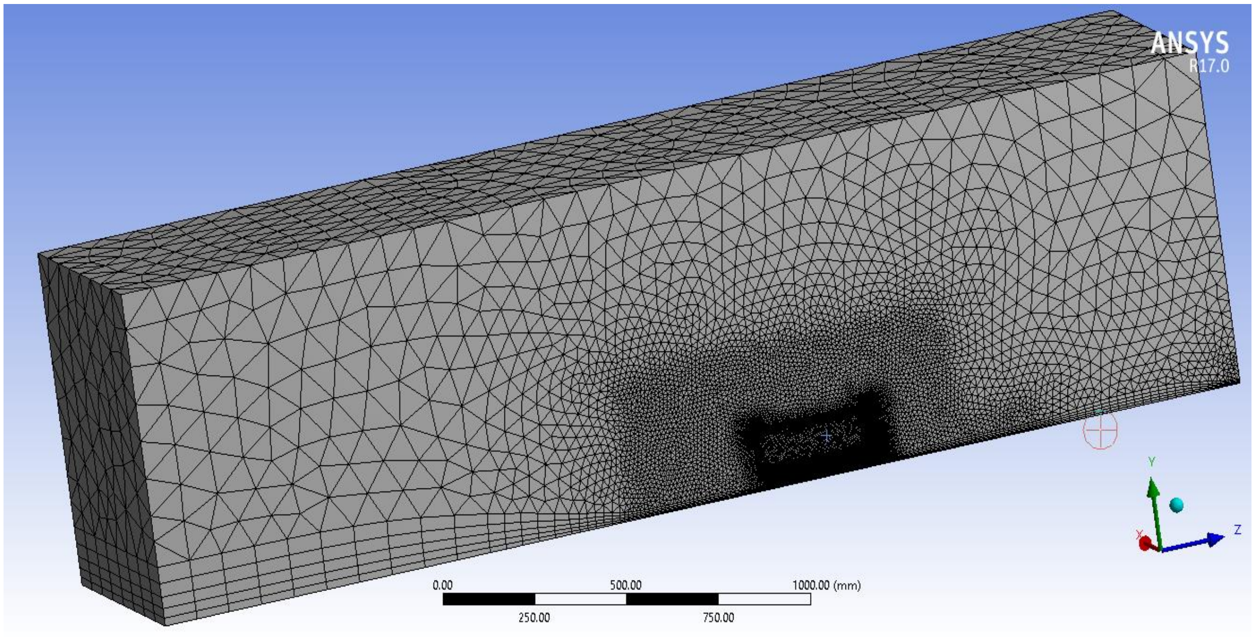

Figure 3. 14: Car-box influence on the mesh

The second box, called underbody. It refines the control volume between the ground and the underbody of the car surfaces. It has a length of 1.5L and a height of ground clearance. The third box, called wake-box. It refines the wake region on the rear of the car body (Figure 3.15). It has a length of 0.75L, a height of 0.5L and 0.4L profundity.

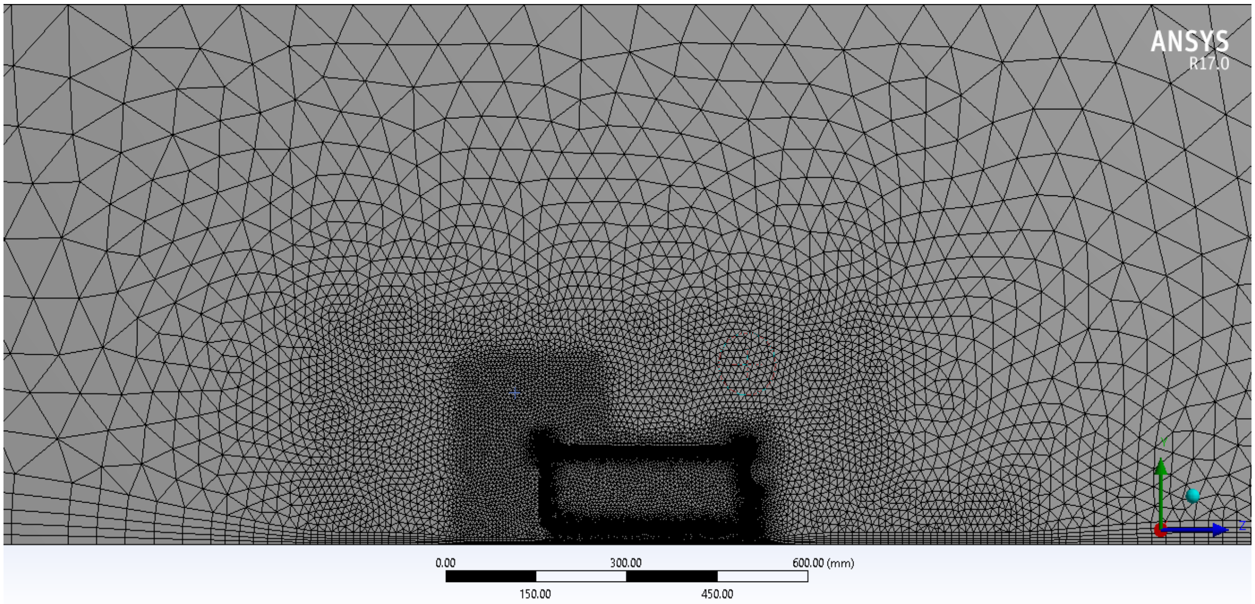

Figure 3. 15: Wake-box influence on the mesh

To ensure the good quality of the results, a few mesh densities were proposed, on the basis of which, the most satisfactory was chosen for further simulations. In order to check the quality of the generated mesh, parameters such as aspect ratio, skewness were verified.

3.7.2 Solver Stage

After the mesh has been imported in Ansys Fluent, a check has been performed to be sure that there are no negative volumes on the mesh. Then the solver settings to be completed before starting the simulations. The solver setting includes the type of solver (3D or 2D), the viscous model, boundary conditions and solution controls. The inlet of the wind tunnel was indicated by the term "velocity inlet", while the outlet of the wind tunnel was termed as "pressure-outlet". The realizable k-ε model was employed in the fluent simulations for all models. The simulations were run with a velocity of 80 kmph, 100 kmph, and 120 kmph. In the simulation the airflow from the velocity-inlet towards the pressure-outlet with a selected amount of velocity. The turbulence intensity for the velocity inlet was reduced to 1%. Turbulence intensity can be defined as the root-mean-square of the velocity fluctuations over the mean flow velocity. A turbulence intensity of 1% is relatively low meaning steady airflow and the velocity introduced to the simulation had very low fluctuations and therefore very little turbulence (assuming that the flow is quite laminar at the inlet of the control volume). The area of each specific model was found using the Fluent project area feature and was utilized in determining the drag coefficient of the vehicle model from the force that was calculated during the simulation.

The bus body is considered stationary for study. Constant velocity inlet condition is applied at the inlet and at the outlet zero-gauge pressure is applied with operating pressure as atmospheric pressure. The flow is considered to be incompressible and steady in nature and the equations are solved using both first and second-order upwind method. A coupled scheme was chosen for the pressure-velocity coupling with Least squares cell-based gradient. It offers more robust and efficient single-phase solutions for Steady flows, which brings the benefit to achieve convergence running fewer iterations if compared with the other pressure-based schemes such as Simple, Simplec or PISO. While employing a coupled scheme the flow courant number was set to 50 while both the explicit relaxation factors for momentum and pressure were 0.25. The flow Courant number is the ratio between the computational distance step and the distance a disturbance travels in one-time step. Reducing this value improves the accuracy and steadiness of the simulation. The reduction in the explicit relaxation factors allowed for a more skewed mesh to be converged easier. They represent the percent of the solution being used from iteration to iteration throughout the simulation. The turbulent viscosity relaxation factor was set to 0.8 during first upwind and changed to 0.95 for second upwind. In order to monitor the calculations and simulations a monitor was created for drag, lift and scaled residuals on the vehicle. Once the monitor was created it could be used to set the convergence criterion for the simulation. The convergence was set to none.

The numerical computation was first started with the first-order scheme to ensure numerical stability. In the first stage, first-order equations were used for the first 100 iterations so as to prevent the solution from diverging. Once sufficient convergence was achieved, the equation order was raised to second order for the rest of the iteration (1000 iterations), so as to get a negligible and accurate drag coefficient.

Most of the scaled residuals and the global aerodynamic quantities such as the drag and the lift coefficients converged to 10^{-5} long way before the 1000 iteration. Once this convergence was met the simulation was complete and stopped. The convergence criteria for the monitors is 10^{-5}. It means that the solution will be considered converged when the change on the values on the residual of continuity between two consecutive iterations is equal or smaller than 0.00001. These facts are considered for providing good accuracy and convergence.

3.7.3 Post-Process Stage

CFD allows users to graphically view the results of a CFD calculation at the end of computational simulation. The majority of ways that the CFD results are emphasized graphically can be classified in different categories. The different ways of representation are X-Y Plots, Vector plots, Contour plots, and Data reports.

3.8 Grid Independence Study

Grid convergence study has been made to verify the CFD model and prove the mesh independence. The first concern for the quality of the solution is the influence of the surface mesh on the solution since the boundary is interpolated onto the solution grid. The approximation of the surface mesh as a representation of the geometry can cause errors if not refined enough. In order to evaluate the goodness of this approximation the surface mesh is rearranged in both finer and coarse spacing between elements. Simulation of the baseline model is selected for the test; similar fluid grid used were computed with finer and coarse surface mesh, which showed that the solution is independent of the surface mesh; as can be seen in Figure 5.74 and 5.75. In general, the surface mesh need to be refined, but the surface used for the first simulation is accurate enough to capture the most important flow features in the present thesis. These results show that the solution is independent of the surface mesh presented in Appendix C.

Table 3. 4: Grid independence study

Mesh Name	Element Size (mm)	No. of Elements	Drag Coefficient	Lift Coefficient
Mesh-1	12	1,146,716	0.72748	-0.29485
Mesh-2	11	1,245,052	0.72931	-0.30014
Mesh-3	10	1,403,239	0.72877	-0.30106
Mesh-4	9	1,673,645	0.72846	-0.29772
Mesh-5	8	2,003,496	0.72889	-0.30082

4. EXPERIMENTAL VALIDATION OF NUMERICAL ANALYSIS

4.1 Introduction

The numerical analysis by Computational Fluid Dynamics (CFD) performed using ANSYS Fluent were discussed on chapter three. The validation of the numerical results is mostly done by comparison with results obtained through direct measurements from experiment. The most reliable information about physical phenomena is usually given by measurements but in certain situations, an experimental investigation which involve full scale model or equipment are either very expensive or difficult to perform or not possible at all. An alternative solution is to perform the experiment on a small-scale model and extrapolate the results obtained to the full scale.

This chapter focused mainly on the experimental validation using wind tunnel to validate the numerical analysis of the baseline model. Experimentation is particularly important in applications such as fluid mechanics, where the behavior of the system is difficult to model analytically. Wind-tunnel testing is thus the preferred method for measuring the aerodynamic effects of fluid flowing past a body. The key flow characteristics such as lift and drag can then be deduced from these experiments. The nature of fluid flow allows engineers to create scale models of the body in order to assess the behavior of fluid flow around it.

4.2 3D Model Preparation

The modern automotive industry uses the advantages of 3D printing to a significant degree. As the wind tunnel testing is essential for the aerodynamic development. The 3D model of an Isuzu Midi Bus was printed in Addis Ababa American Center laboratory with a 1:3 scale (comparing to the model that was simulated in ANSYS Fluent). The printer is shown in Figure 4.1.

This printer used plastic material of Polyacetide (PLA), which is supplied to the printer in a form of filament (1.75 mm diameter) and then melted in a hot-end at high temperature. The printer head distributes the material layer by layer, basing on the input code.

Figure 4. 1: IIIP 3D Printer

The positioning of model on the printer table determines the amount of supports, which need to be manually removed once the printing process is finished. This process demands a careful approach, as it is relatively easy to damage the printed object itself. Afterwards, the printing surface needs to be smoothened and all irregularities must be removed this can be done by sandpaper.

Figure 4. 2: The prototype of Isuzu midi bus for wind tunnel test

4.3 Experimental Set up

The HM 170 Educational wind tunnel (Figure 4.3), is a subsonic, open wind tunnel with a square measurement section profile was developed for experimentation of Isuzu midi bus baseline model. This wind tunnel was used to determine the lift and drag forces on the baseline model.

Figure 4. 3: Defense University (Bishoftu, Ethiopia) Educational Wind Tunnel.

The air is drawn in from the atmosphere via the streamlined funnel (1). Any transverse flow components are filtered out in the flow straightener (2). It is made of a tubular honeycomb structure. The air exits from the flow straightener as a parallel flow and is accelerated to roughly 3.3 times its original velocity in the jet (3). The static pressure (4) is measured downstream of the jet at the entrance to the measurement section. Based on the assumption of virtually loss free flow, the flow velocity can be determined from the pressure difference with respect to ambient pressure (total pressure at zero velocity). The air then flows through the measurement section (5) which has a constant cross-section as shown in Figure 4.4. After the measurement section the flow is decelerated in a diffuser (6) and part of the pressure drop required to accelerate the air in the jet is recovered. The diffuser angle is designed in a way to prevent flow separation. An axial fan (7) with downstream guide (8) draws the air out of the diffuser and conveys it into the open. A guard

(9) in front of the fan prevents damage caused by foreign matter or models, whereas the guard (10) behind the fan prevents contact with the fan when it is in operation.

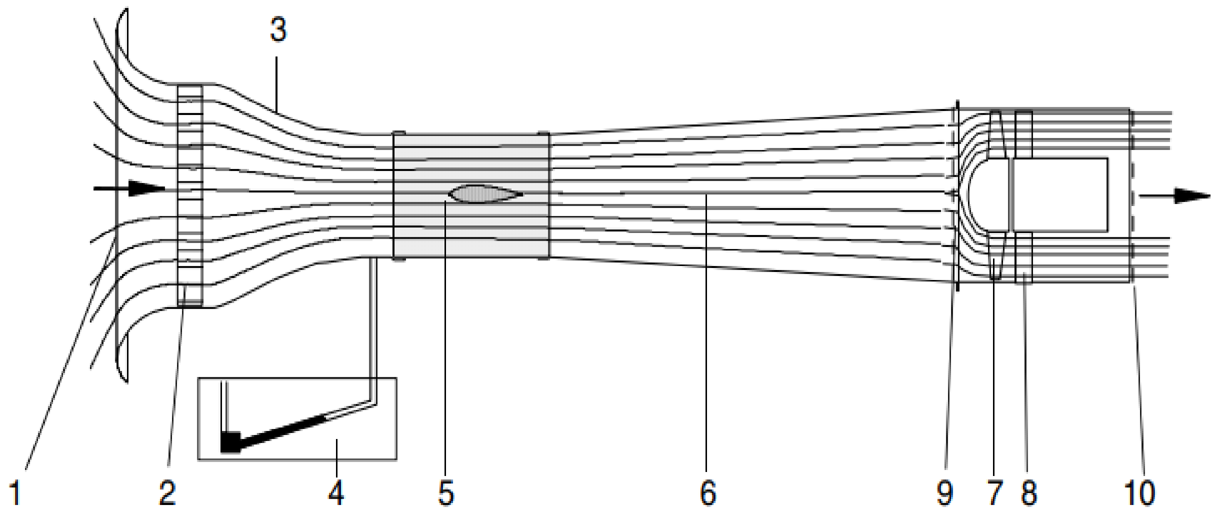

Figure 4. 4: Schematic drawing of HM 170 Educational wind tunnel (Garatebau and Barsbuttes, 2010)

4.4 Testing procedure

The steps that were followed in order to conduct the wind tunnel tests include securing the baseline model of bus in the wind tunnel (Figure 4.5), zeroing the measuring equipment (Figure 4.6), starting the test at a low speed and working up to faster speeds, taking measurements at each speed increment and repeating the test three times to establish more accurate results. Securing the models was done with the use of model holder. The model holder was attached to the flat rod, which is attached to the equipment that measures the lift and drag forces acting on the model.

In order to zero the measuring instrumentation two radial dials were adjusted until the values of the lift and drag displays were as close as possible to zero. The dials are very sensitive and it was therefore quite hard to have the readout on the displays show exactly zero. Before starting the wind tunnel's motor, the enclosure lid was closed to avoid injury to the operator or damage to the enclosure. Once the motor had been started the wind tunnel's speed was adjusted to a reasonably slow speed. For each test the wind tunnel was adjusted to four speeds and the lift and drag force readings were written down. The test was conducted three times with a baseline model to obtain a reasonable amount of data for analysis allowing for an averaged value to be obtained. Obtaining an average value ensures a good result as it accounts for variables that affect each of the runs.

Figure 4. 5: Securing the prototype of Isuzu midi bus in the wind tunnel

The prototype was tested at different speeds with values of 12 to 28 m/s in an increment of 5 m/s at zero-degree angle of attack. The values of the normal and axial forces were obtained.

Figure 4. 6: Zeroing the measuring equipment

Figure 4. 7: Prototype of Isuzu midi bus mounted in the wind-tunnel

5. RESULTS AND DISCUSSIONS

This chapter presented the results of both the Computational Fluid Dynamics (CFD) analysis and experimental validation then discussed these results. The CFD analysis was performed using ANSYS FLUENT and the Experimental validation was performed using Wind-tunnel to validate the Computational analysis. The results and discussions of Computational analysis presented in section 5.1, then the results and discussions of experimental validation presented in section 5.3.

5.1 Results and Discussions of CFD Analysis

A 3D steady-state, incompressible solution of the Navier-Stokes equations was performed using ANSYS FLUENT. Turbulence modeling was done with the realizable k-ε model using non-equilibrium wall functions. The computational results of different models are presented and discussed. All the results for different cases were obtained with the same meshing resolution, the same k - ε turbulence model, and also the same boundary conditions. For the first 100 iterations, a first-order upwind discretization was used to accelerate the convergence then after 100 iterations second-order upwind scheme has been applied and iterations have continued until it reached to the convergence criteria. The convergence criteria were having all residuals below 10^{-5}.

5.1.1 Baseline Model Results

To determine the reduction in the drag coefficient from different models of the bus with modifications, the drag coefficient and flow field of a baseline model examined first. These simulations give the base drag coefficient for the study. After simulating the baseline model, the modified models were simulated next. After the simulation, all models were compared to the flow field, drag and lift coefficient of the baseline model. To determine the percent reduction of the drag coefficient due to the outer body modifications were compared.

Analyzing the residual trends is one of the most fundamental measures in determining whether a solution is converged or not. It directly quantifies the error in the solution of the system of equations. The residuals and the values for the coefficients of lift and drag were monitored during all numerical analyses. The convergence criteria were satisfied when all the values of monitored residuals dropped below 10^{-5}, which is two orders of magnitude lower than standard convergence criteria (10^{-3}), and the computed values of lift and drag coefficients stabilized over subsequent iterations.

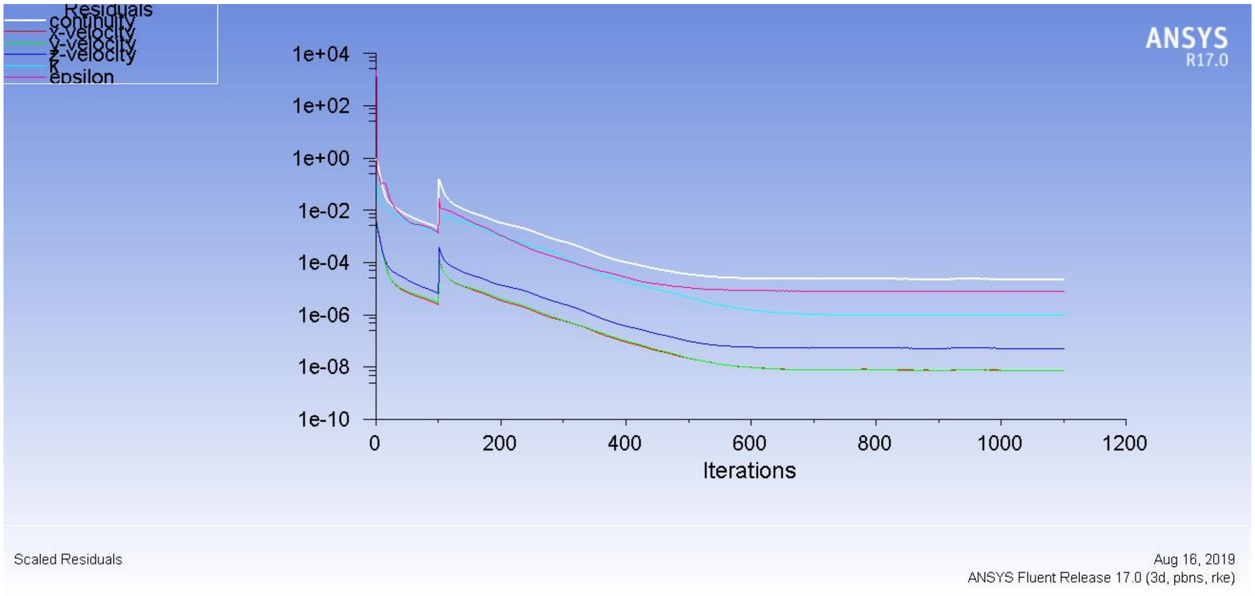

Figure 5. 1: Scaled residuals of the baseline model

The scaled residual for baseline model at 80 kmph, 100 kmph, and 120 kmph shows how the parameters converge with each iteration. It is evident that the convergence for this case was already achieved after 600 iterations. Figure 5.1 shows residuals are jumped off at the 101st iteration because the scheme has been changed from first-order upwind to second-order upwind in order to reach convergence much faster.

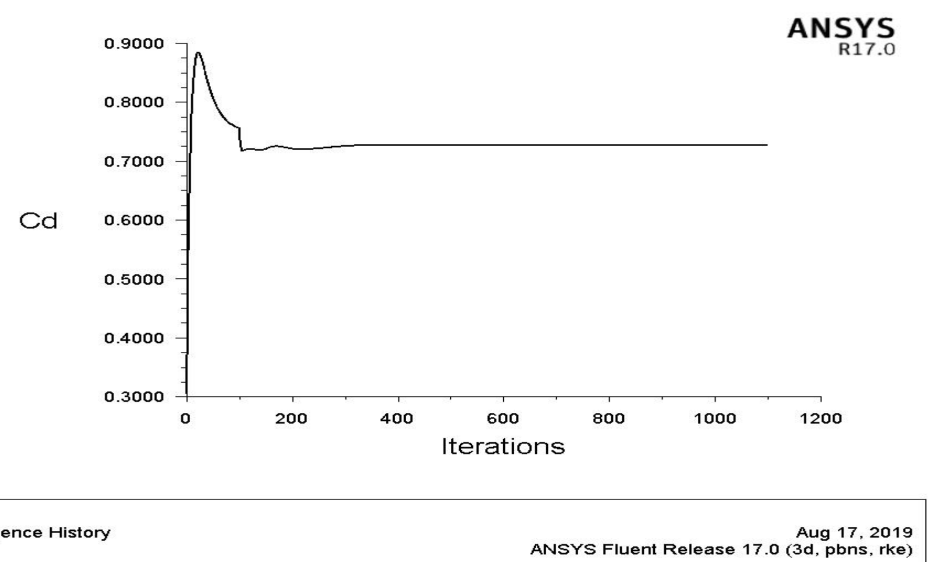

Figure 5. 2: Drag coefficient of baseline model at 80 kmph

Result of scaled residuals (Figure 5.1), drag and lift coefficient, pressure and velocity contour at speed of 80kmph, 100kmph and 120kmph of baseline model are presented.

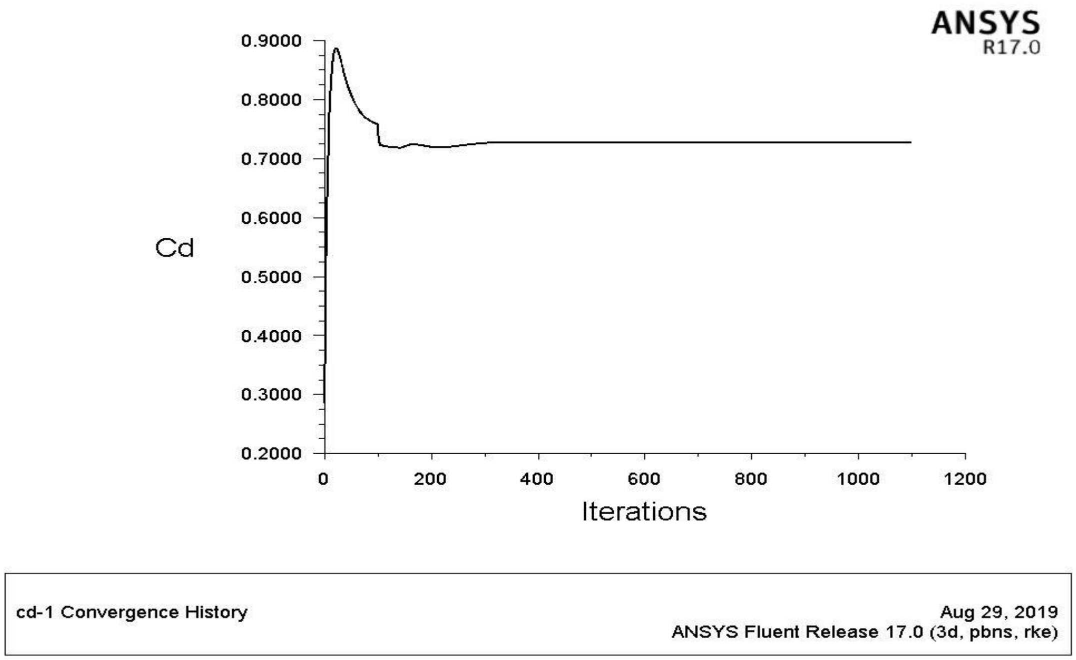

Figure 5. 3: Drag coefficient of baseline model at 100 kmph

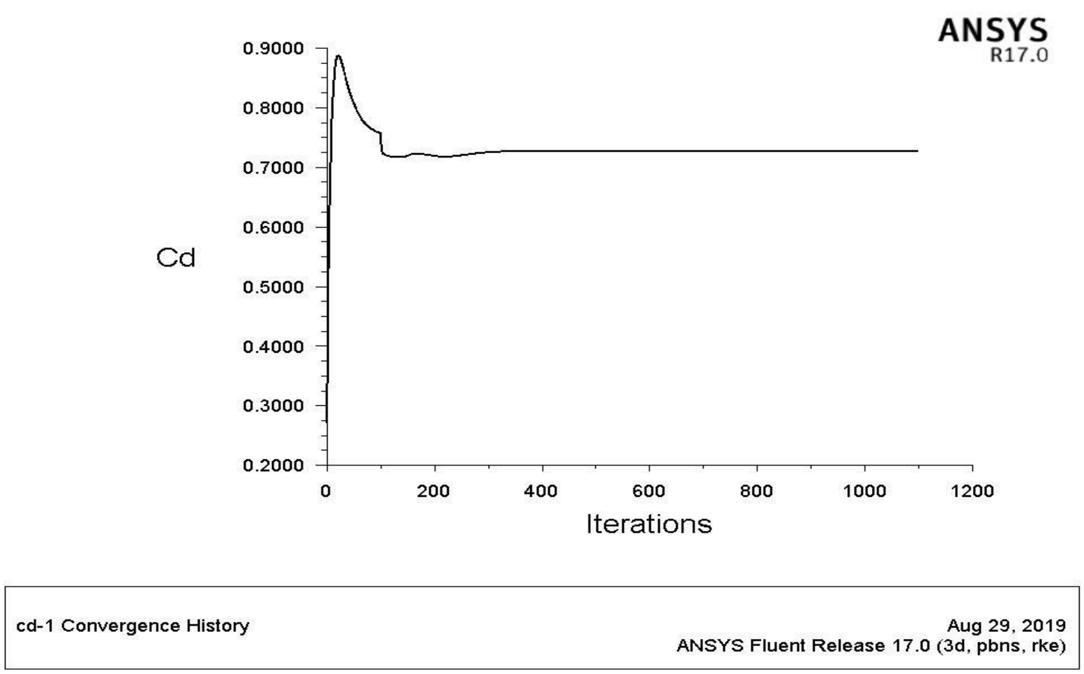

Figure 5. 4: Drag coefficient of baseline model at 120 kmph

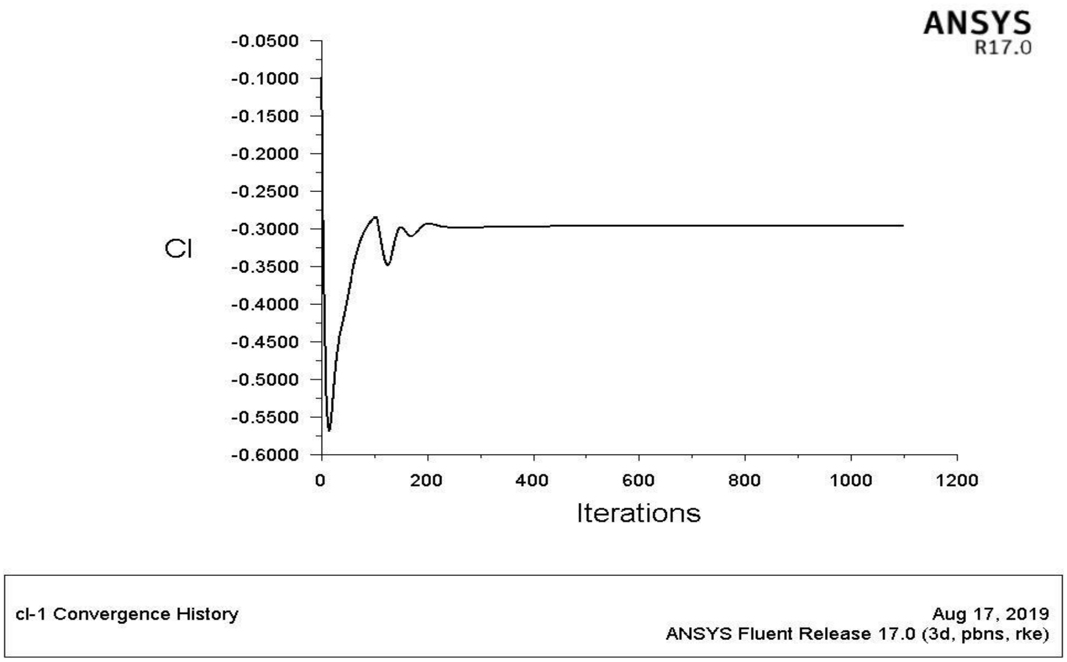

Figure 5. 5: Lift coefficient of baseline model at 80 kmph

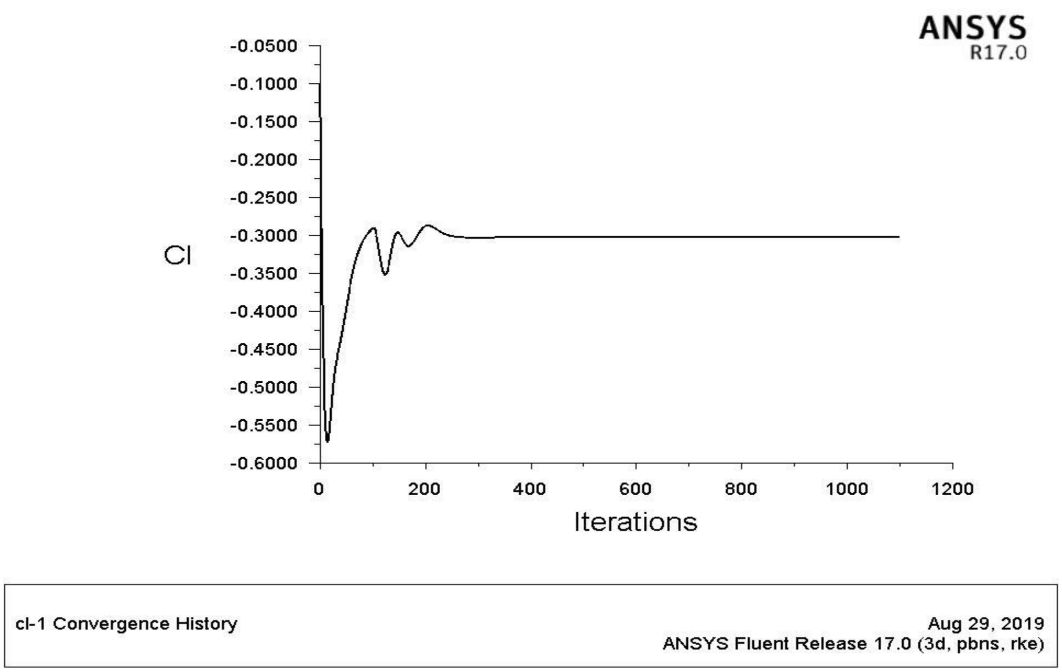

Figure 5. 6: Lift coefficient of baseline model at 100 kmph

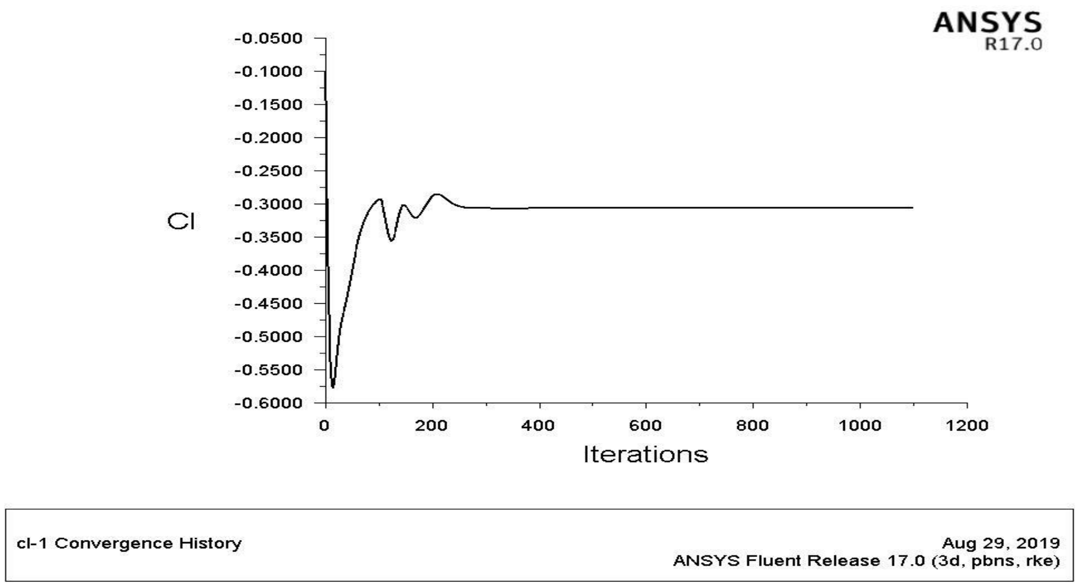

Figure 5. 7: Lift coefficient of baseline model at 120 kmph

All the above graphs indicate (Figures 5.2-5.7) the drag and lift coefficients of the baseline model at speed of 80, 100, and 120 kmph, here the drag and lift coefficients are summarized below in table 5.1.

Table 5. 1: Summary of drag and lift coefficients of the baseline model at different speeds

Model	Speed (kmph)	C_d	C_l
Baseline Model	80	0.72872	-0.29553
	100	0.72877	-0.30106
	120	0.72895	-0.30518

Figures 5.2-5.7 and Table 5.1 showed that the result of the drag and lift coefficients of a baseline model at three different speeds (80 kmph, 100 kmph, and 120 kmph) when simulated the bus model by RKE turbulence model. As shown in the figures both the drag and lift coefficients converge before the 400th iteration.

As shown in Table 5.1 the drag and lift coefficients were found to be 0.72872, 0.72877, 0.72895 and -0.29553, -0.30106 and -0.30518 at speeds of 80, 100, and 120 kmph, respectively. The drag coefficient of a baseline model increases with increasing speed. However, the lift coefficient of a baseline model decreases with the increasing speed which results high downward force, which is very necessary for vehicle stability at higher speed.

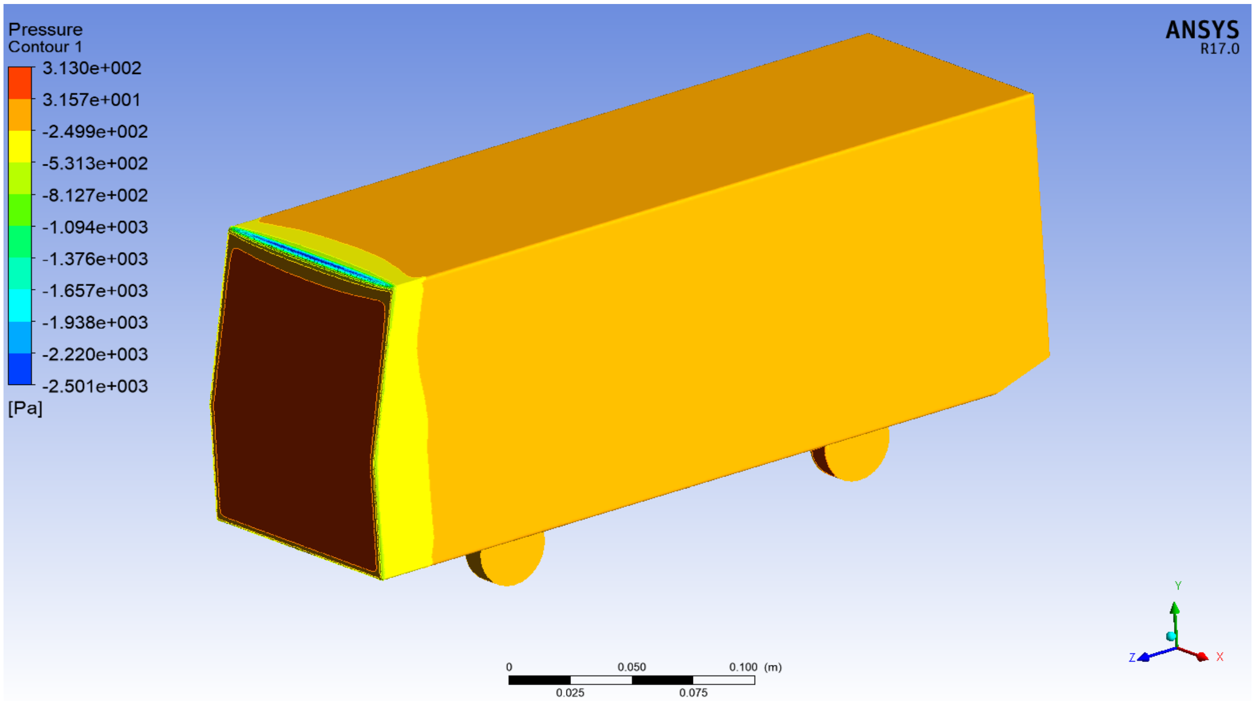

Figure 5. 8: Pressure contour of the baseline model at 80 kmph

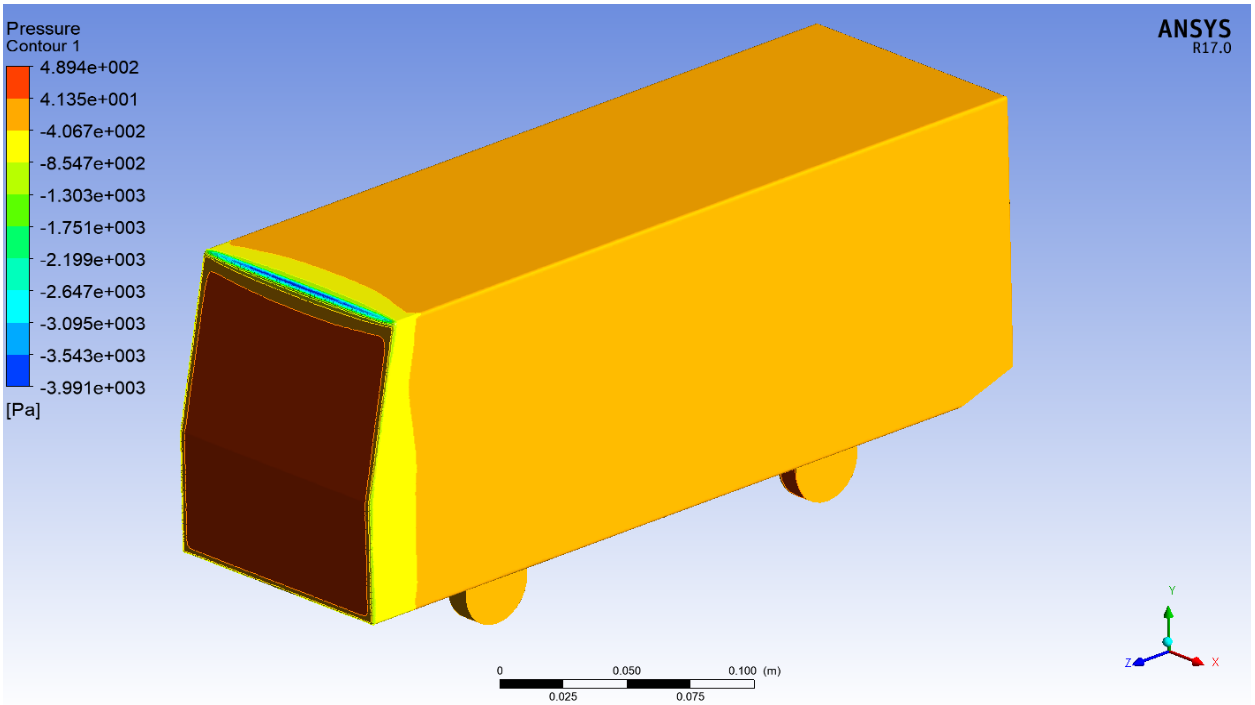

Figure 5. 9: Pressure contour of the baseline model at 100 kmph

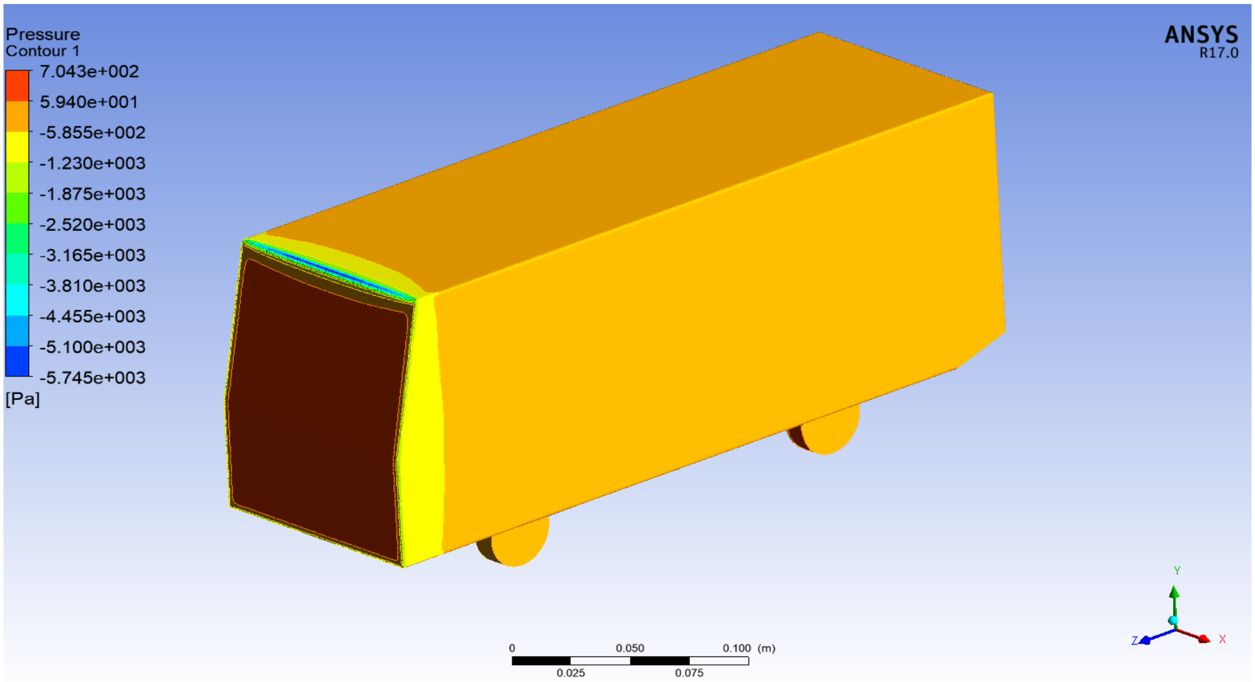

Figure 5. 10: Pressure contour of the baseline model at 120 kmph

From the Figures 5.8-5.10 it can be observed that the pressure distribution at a different speed on the body of the baseline model fluctuates a lot on its boundaries. The pressure contours plots indicate that the pressure on the front end of the vehicle reaches a maximum as the fluid flowing towards the vehicle comes to a stagnation state. Stagnation is the region that comes in contact with the air in the first instance when the car is in motion. It can be further observed that the pressure of the fluid over the entire body drops to negative values. The rear wall of the bus experiences low pressure compared to the front due to the flow separation and wake formation behind the bus. The high-pressure difference existing from the front to the rear end of the bus leads to a very high "Pressure Drag".

The total drag is a combination of viscous drag and pressure drag. Since the fluid is air which has very low viscosity, the friction drag is a very small component of the total drag at low velocities. But with the increase in velocity of the vehicle, friction drag also contributes significantly to the total drag. With the increase in speed, the flow separation zone where vortices are formed is found to increase in size. This produces even higher pressure drag. The friction drag also increases with increase in velocity. Hence, the total drag at 120 kmph is due to both viscous friction and separation.

The rear low-pressure region created by the flow separation must be brought to a minimum for reducing the pressure drag acting on the body. Incorporating aerodynamic design features as reported in the literature such as roof tapering, roof end lowering, and radius improvements will reduce the drag of the bus.

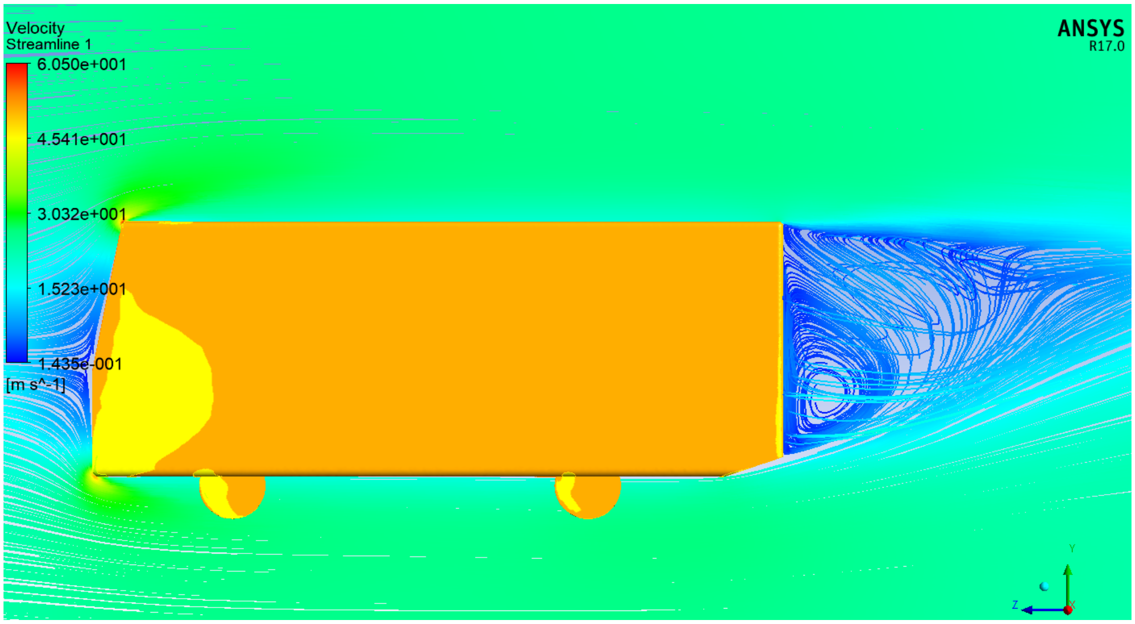

Figure 5. 11: Velocity contour of the baseline model at 80 kmph

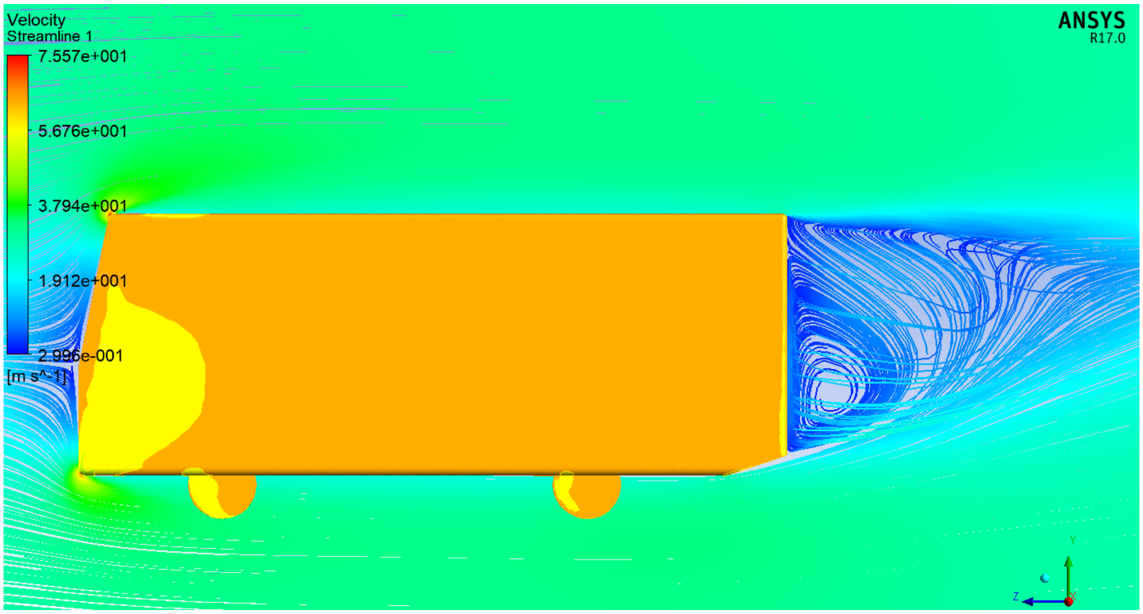

Figure 5. 12: Velocity contour of the baseline model at 100 kmph

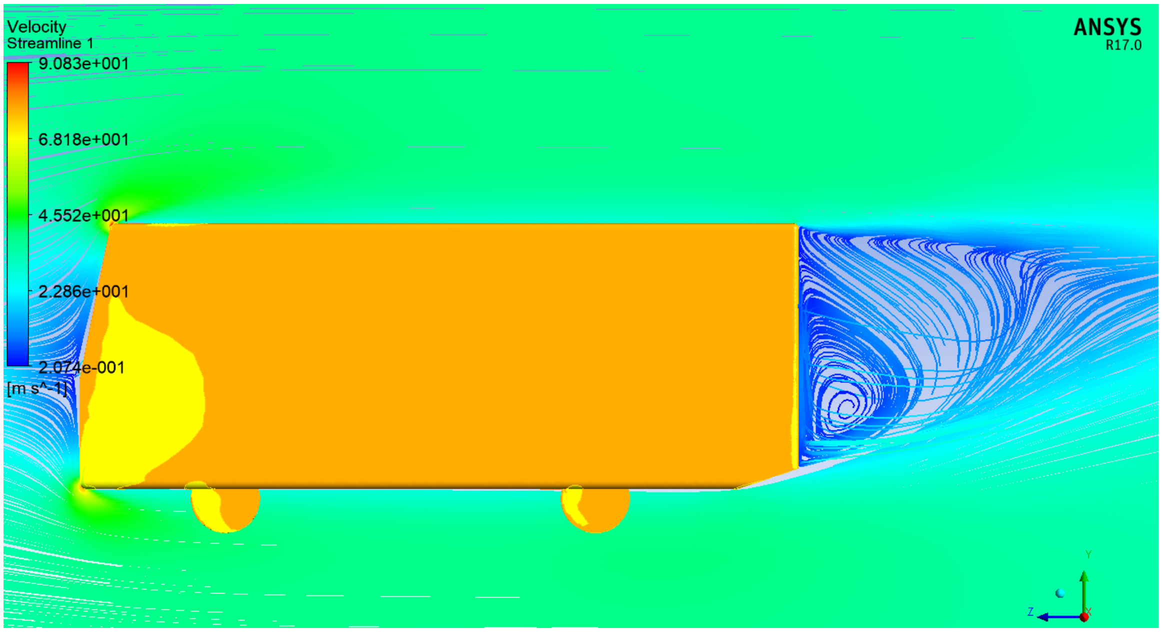

Figure 5. 13: Velocity contour of the baseline model at 120 kmph

The purpose of the analysis based on the visualization of the airflow around the vehicle is to locate the places where the flow is disturbed. The most important is the nature and the structure of the flow. Visualization of path lines provides important information about the flow structure. The areas of streamlined flow, separation, and recirculation, vorticity generation can be determined. This gives a more complete picture of the nature of the flow. Streamlines are the lines that are tangential to the flow velocity. As can be seen, the streamlines are in direction with the car surface and some streamlines tend to bend toward the rear side of the car. Also, the wake region in the back of the car can be observed clearly.

From Figures 5.11, 5.12 and 5.13 illustrates the velocity contour of the baseline model without any body modifications employed at three different speeds. A legend can be observed in figures representing the magnitude of the velocity of the airflow in m/s, with colors corresponding to the velocity contour shown. It should be noted that the velocities were 22.22 , 27.78, and 33.33 m/s and the maximum velocities for baseline model in the flow field due to flow separation were nearly 59.02, 74.59 and 90.69 m/s and the minimum velocities were 0.06721, 0.03135 and 0.03588 m/s, respectively. The colors indicate the velocity magnitude. The green color in the contour represents the velocities close to the input velocity and red color represents high-velocity areas of the contour. However, blue color sections in the contour represent low-velocity areas present on the bus body.

The low-velocity area can be seen on the front of the bus at the stagnation point, underbody of the bus, and on the back of the bus. These low-velocity areas produce high levels of turbulence and this turbulence increases the drag on the bus.

From the velocity distribution shown in Figures 5.11, 5.12 and 5.13, it can be observed that flow separation occurs on the rear end of the vehicle due to sudden change in the shape. The flow separation produces a low-pressure zone and it is also seen that vortices are formed due to recirculation. It can also be inferred that the velocity of flow increases over the bus top surface. This can be attributed to the convergence of flow. The high-speed air will not follow the outer contour of the bus instead it gets separated on the rear end, forming a low-pressure zone and inducing pressure drag on the vehicle.

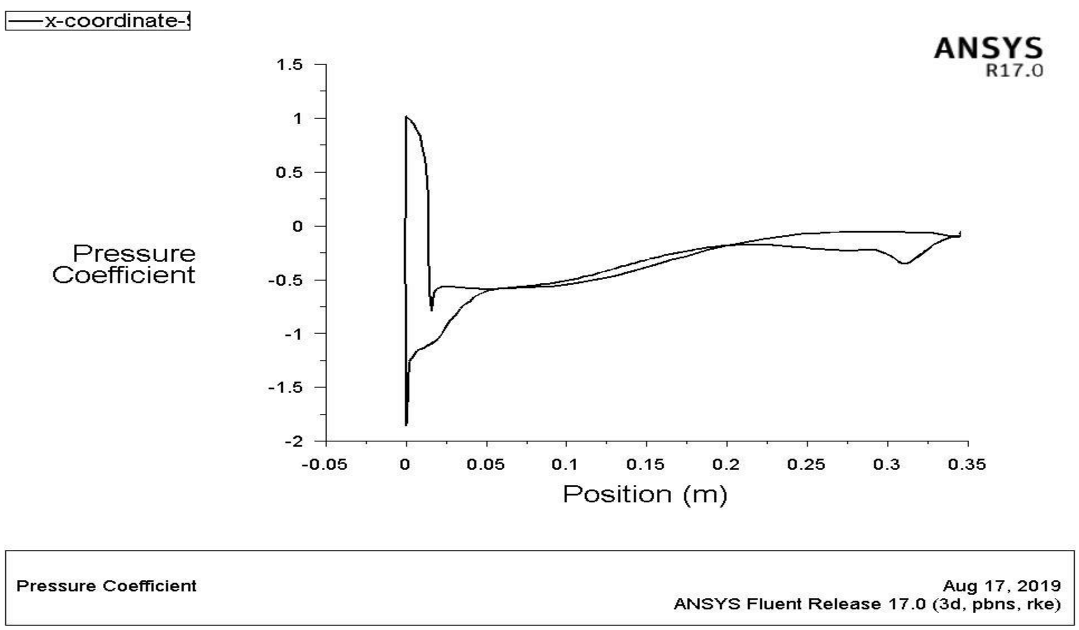

Figure 5. 14: Surface pressure distribution along the symmetry plane of the baseline model

The Pressure Coefficient is a dimensionless characteristic variable that can represent the relative pressure field in the domain. Due to the absence of internal flow, underfloor and body roughness, pressure drag occurs to highest percentage. Figure 5.14 shows the surface pressure distribution along the symmetry plane and it indicates that the maximum value is at the front surface of bus where the stagnation point is generated. After the front of the bus roof surface the pressure decreases due to its streamlined shape and then increases gradually to rear roof of the bus. The pressure on the floor of the vehicle is minimum at the front of the bus then gradually increases to rear of the bus. Therefore, it is important to analyze the high and low areas of pressure present on the bus and how these sections affected the airflow and coefficient of drag.

5.1.2 Model I Results

Convergence can usually be assessed by progressively tracking the imbalance that is accentuated by the advancement of the numerical calculations of the algebraic equations through each iteration step. This imbalance measures the overall conservation of the fluid properties; they are also commonly known as the residuals.

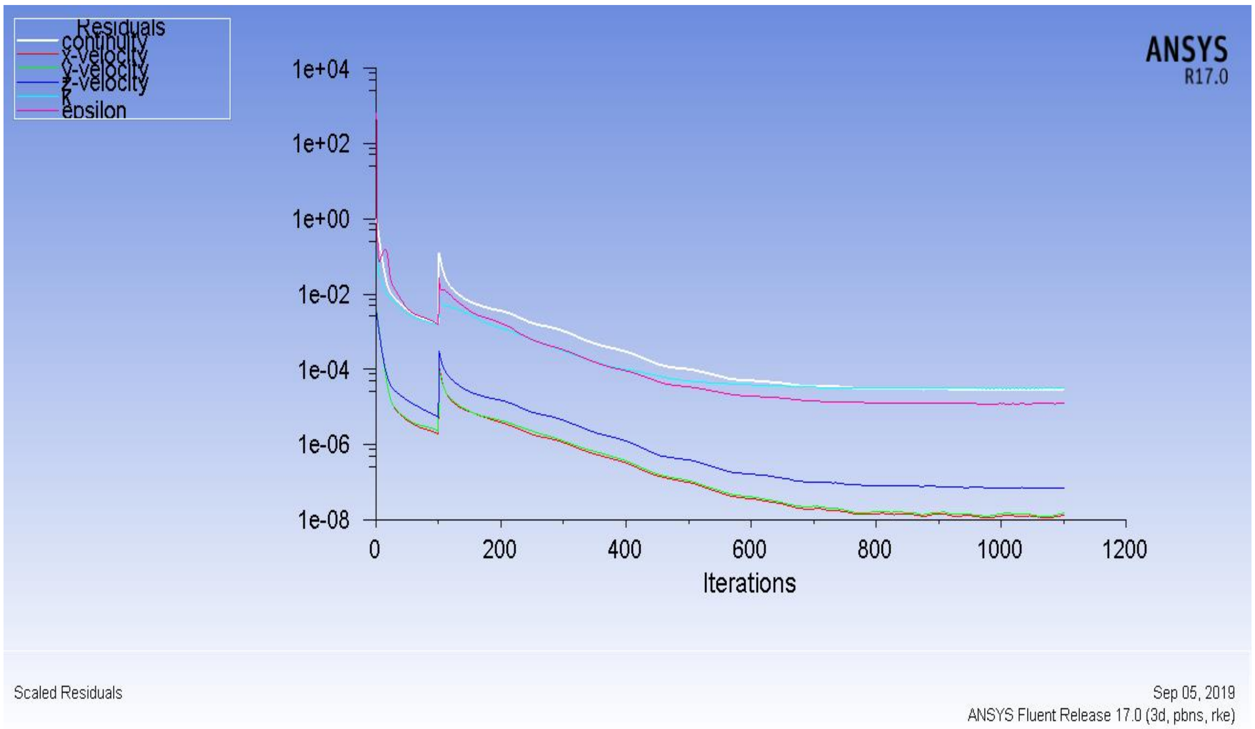

Figure 5. 15: Scaled residuals of model I

Analyzing the residual trends is one of the most fundamental measures in determining whether a solution is converged or not. The trends of the baseline simulation were already shown and discussed.

The results of scaled residuals (Figure 5.15) drag and lift coefficients, pressure, and velocity contour at speed of 80, 100, and 120 kmph for model one are depicted from Figure 5.16 to 5.21.

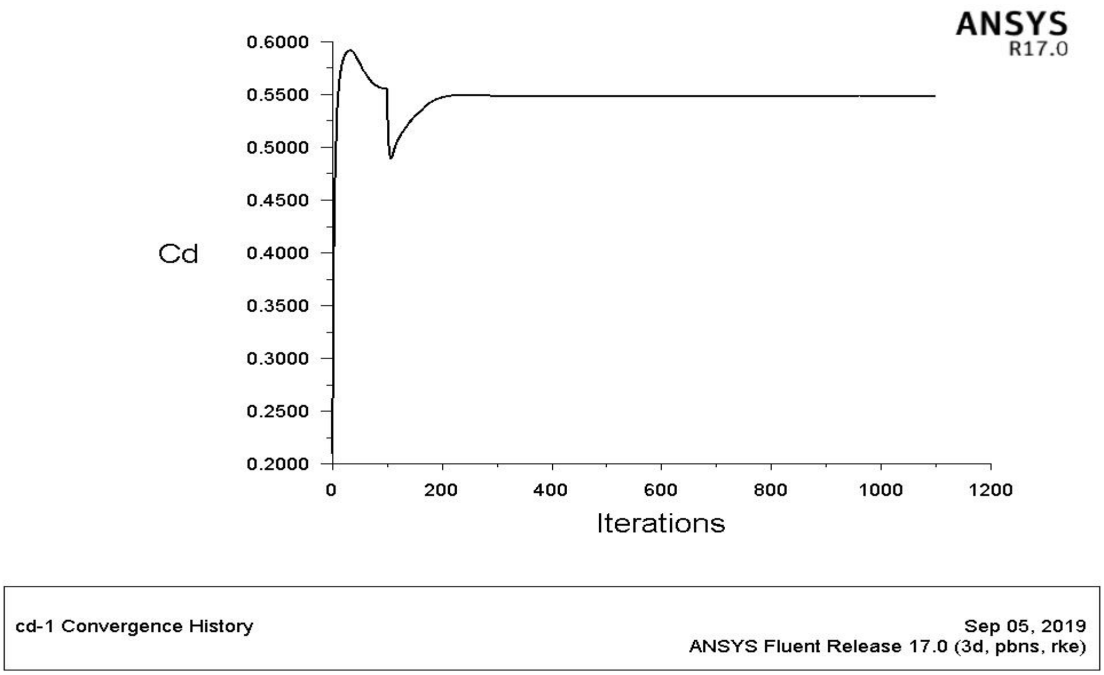

Figure 5. 16: The drag coefficient of model one at 80 kmph

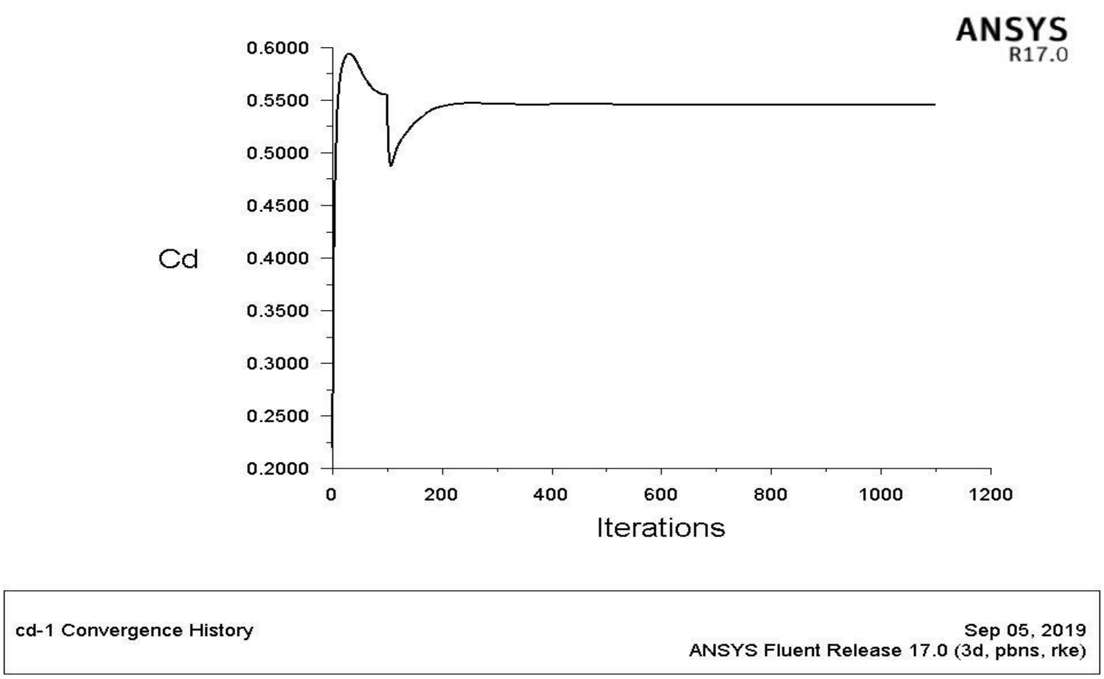

Figure 5. 17: The drag coefficient of model one at 100 kmph

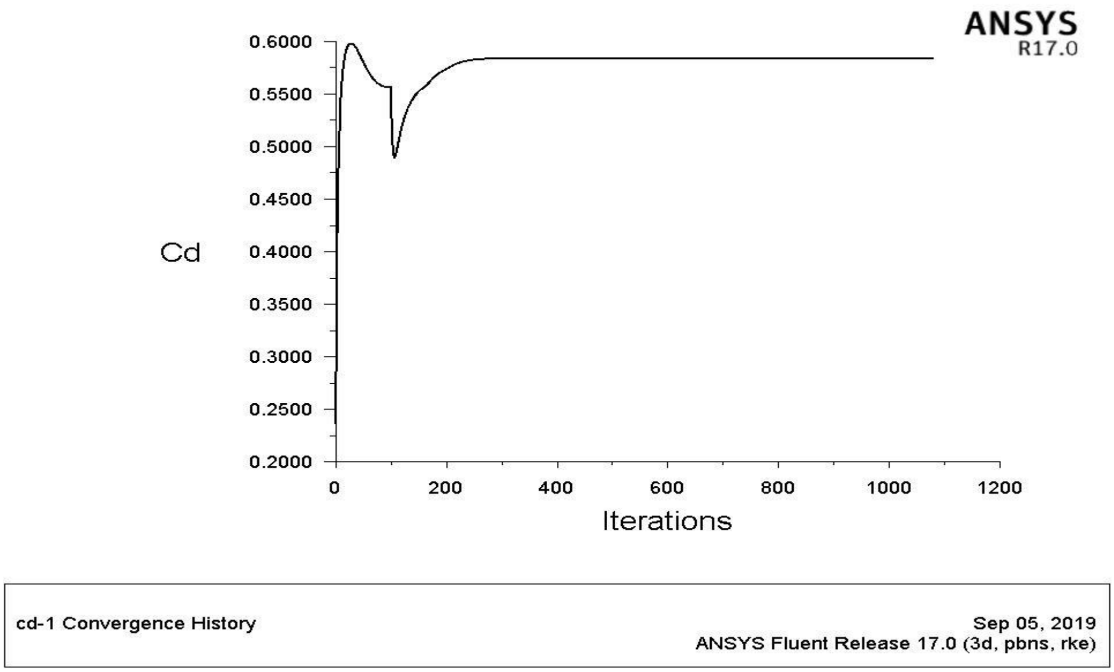

Figure 5. 18: The drag coefficient of model one at 120 kmph

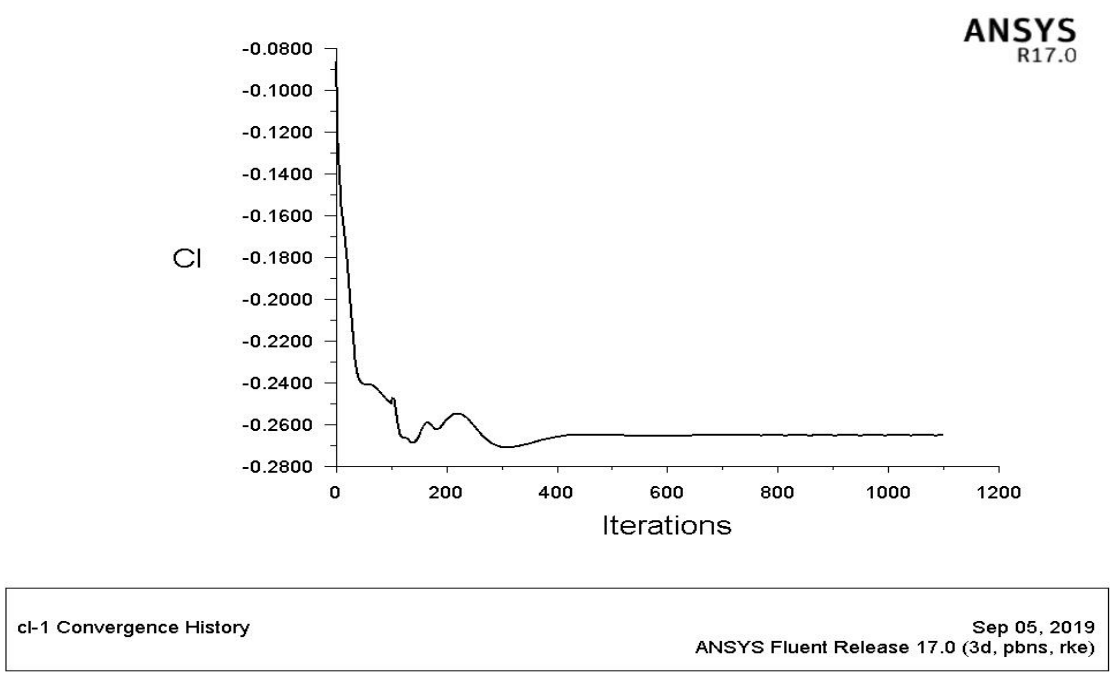

Figure 5. 19: Lift coefficient of model one at 80 kmph

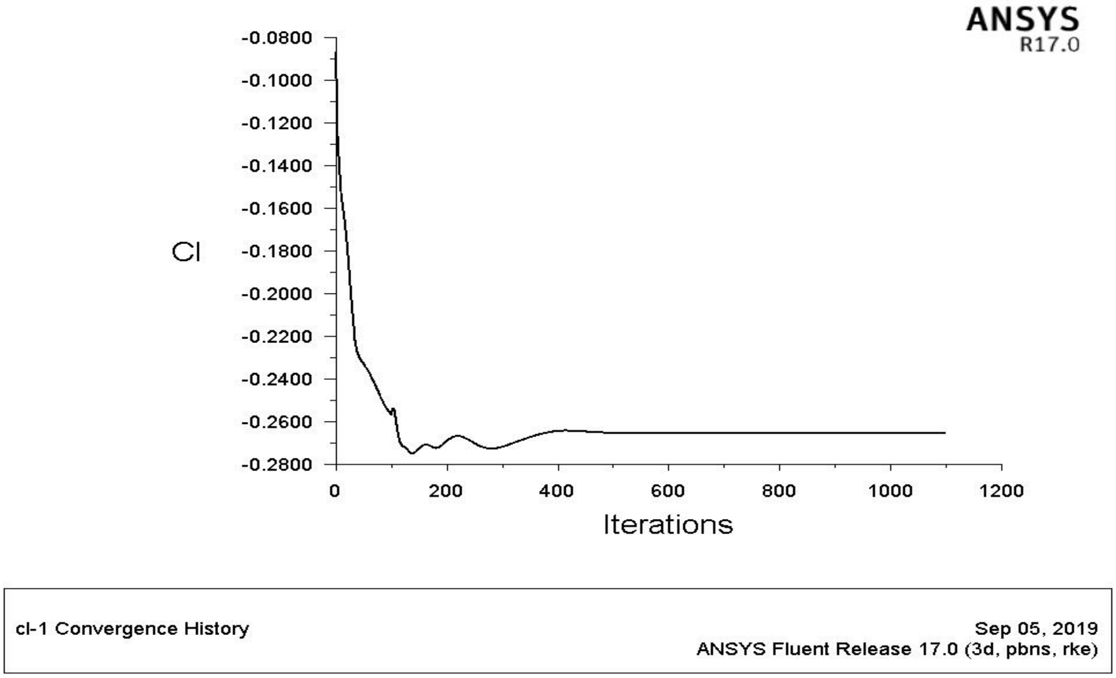

Figure 5. 20: Lift coefficient of model one at 100 kmph

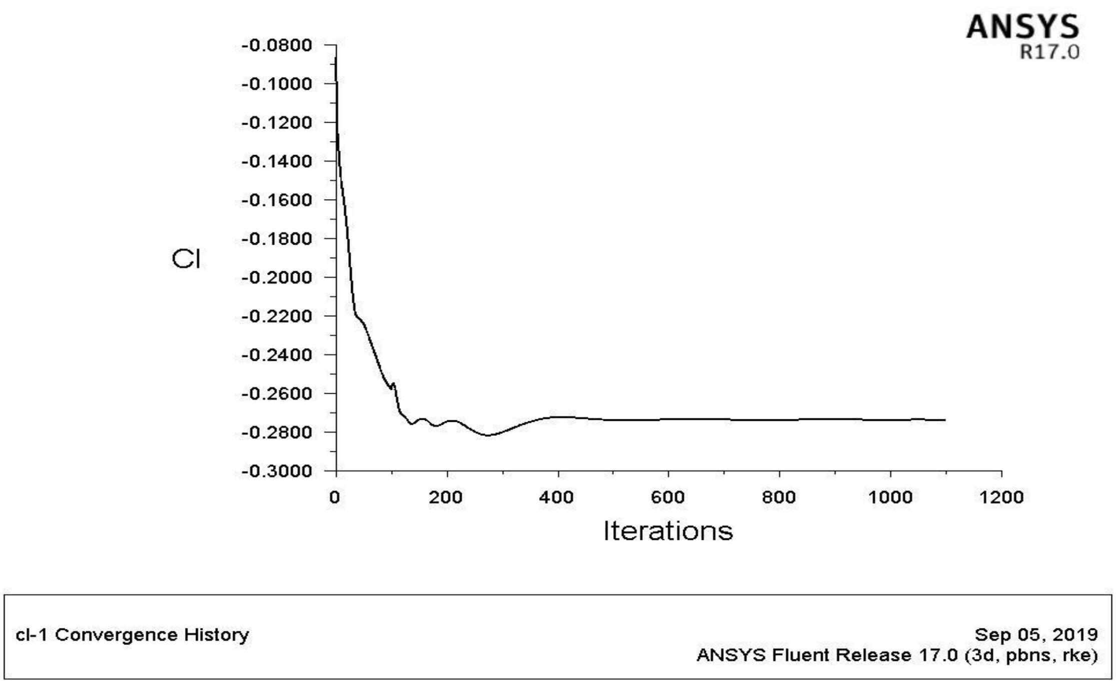

Figure 5. 21: Lift coefficient of model one at 120 kmph

All the above graphs indicate (Figures 5.16-5.21) the drag and lift coefficients of model one at speed of 80, 100, and 120 kmph, here the drag and lift coefficients are summarized below in table 5.2.

Table 5. 2: Summary of drag and lift coefficients of Model I at different speeds

Model	Speed (kmph)	C_d	C_l
Model One	80	0.54672	-0.26465
	100	0.54906	-0.26496
	120	0.58452	-0.27317

Figures (5.16-5.21) and Table 5.2 showed that the result of the drag and lift coefficients of model I at three different speeds of 80, 100, and 120 kmph. As shown in the Figures 5.16-5.21 both the drag and lift coefficients converge before 500th iteration. The drag coefficient of model I increases with increasing speed. However, the lift coefficient of model I decreases with increasing speed which results high downward force, which is very necessary for vehicle stability at higher speed.

The drag coefficient of model I (Table 5.2) is lower than the baseline model (table 5.1). The drag coefficient has reduced from 0.72881 (the averaged drag coefficient at 80, 100, and 120 kmph speeds) for the baseline model to 0.5601 (the averaged drag coefficient at 80, 100, and 120 kmph speeds) for model I, thus the average reduction in C_d is 23.15%. This deviation of the drag coefficient of the model I with respect to the baseline model will give a clear idea about how much the drag force is affected by small modification in front.

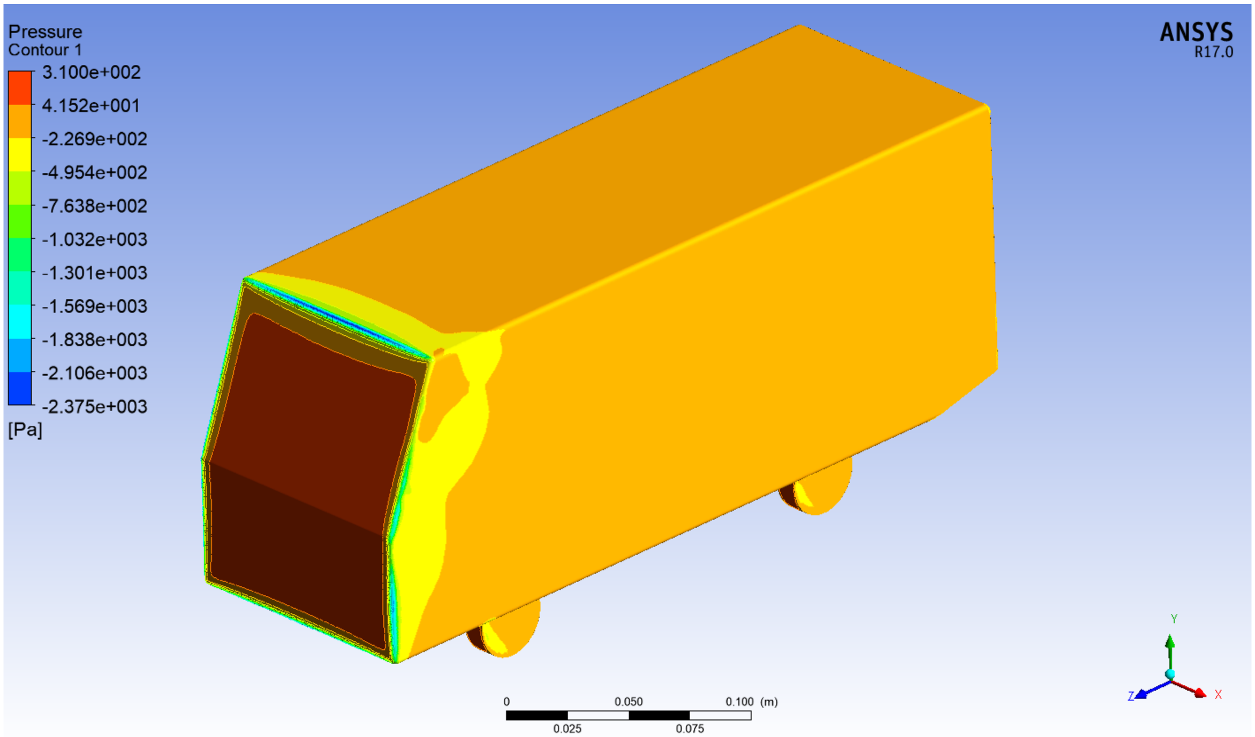

Figure 5. 22: Pressure contour of model one at 80 kmph

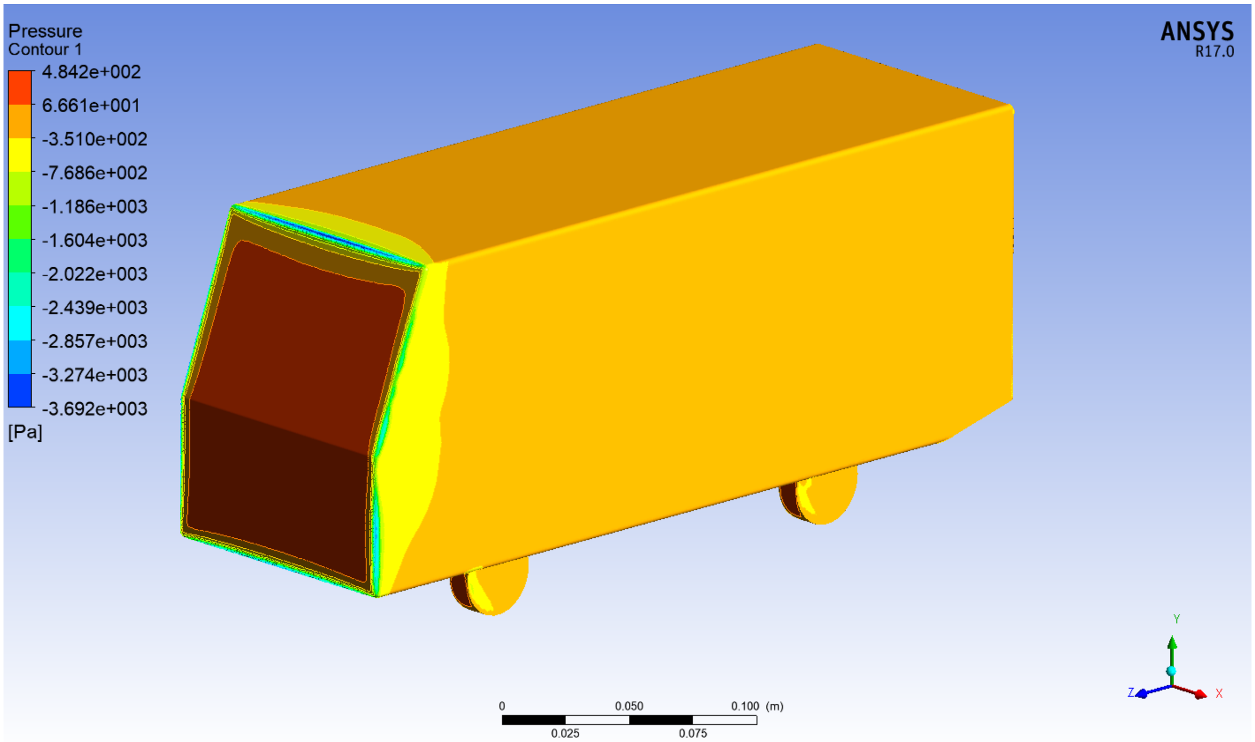

Figure 5. 23: Pressure contour of model one at 100 kmph

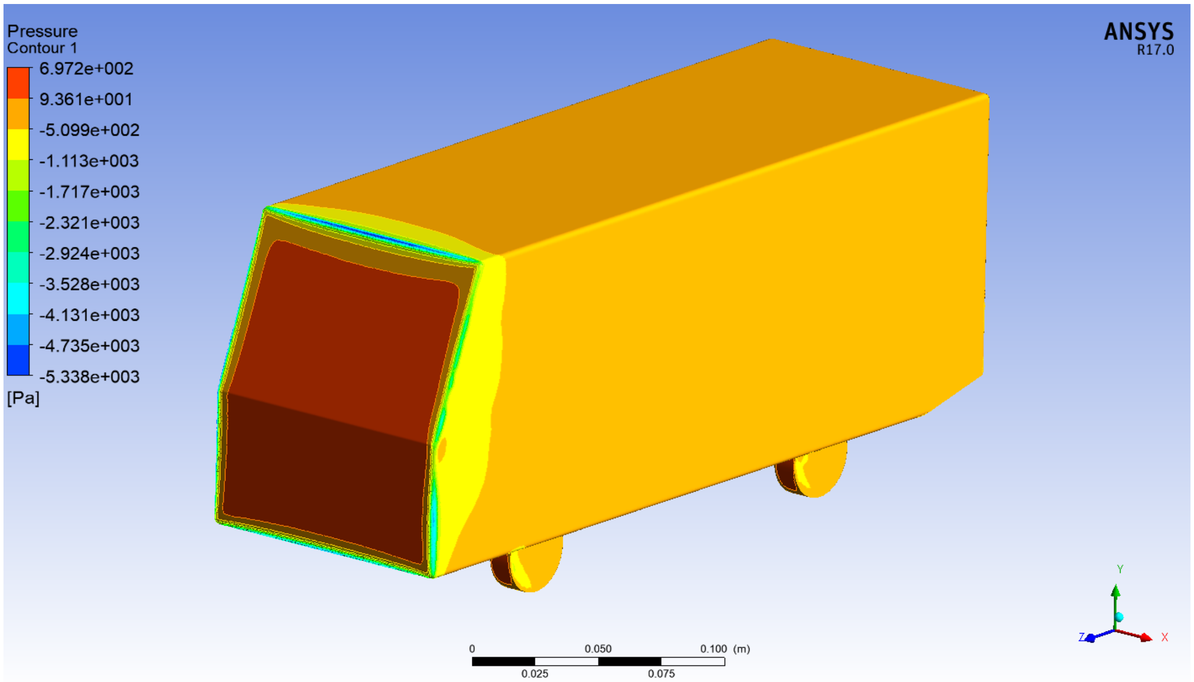

Figure 5. 24: Pressure contour of model one at 120 kmph

The contour of pressure distribution shown in Figures 5.22, 5.23 and 5.24 indicates the level of pressure effect on the surface of the model one. The concept of pressure drags happen when there are two different areas with different level of pressure. Contours of pressure Figures 5.22, 5.23 and 5.24 demonstrate that maximum static pressure is developed on the forward face of the bus model where stagnation of the flow appears colored by red. On the other hand, a low level of static pressure takes place where separated flow exists at the back of the bus model. It is known that the pressure differences between forwarding and backward faces of the bus model cause drag force. The maximum pressure increases with increasing speed. The increase in the surface pressure increases the drag coefficient which can be seen from Table 5.2.

The pressure difference of model one is 2685, 4176.2 and 6035.2 Pa at speed of 80, 100 and 120 kmph, respectively whereas, the pressure difference of the baseline model was 2814, 4480.4 and 6449.3 Pa at speed of 80, 100, and 120 kmph, respectively. The pressure difference of the model one is lower than the baseline model on each respective speed. This fact suggests that the proposed modification results in a lower pressure difference in the modified design. In order to reduce more drag forces of the external flow the sharp corners of the bus model must be converted into a curved shape.

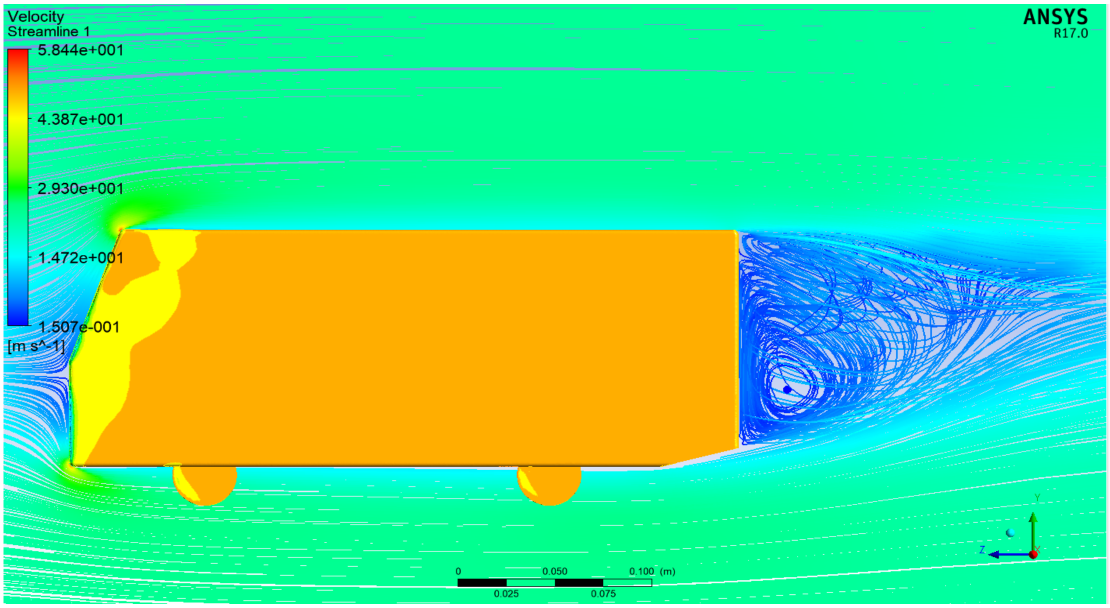

Figure 5. 25: Velocity contour of model one at 80 kmph

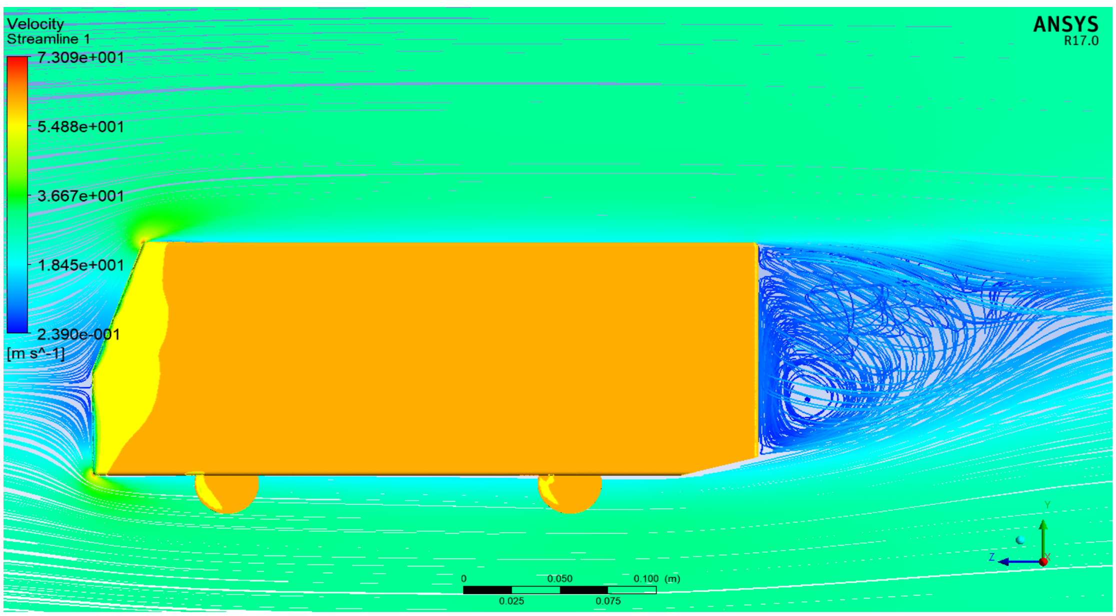

Figure 5. 26: Velocity contour of model one at 100 kmph

The value of velocity is directly proportional to the value of the drag and lift coefficient. Thus, the velocity distribution around the car gives a big impact on the aerodynamic performance of the car. The airflow separation of model one shown in Figure 5.25, 5.26 and 5.27 causes the airflow to become turbulent, hence lower pressure region formed at the back of the car. This will cause a negative effect on the car aerodynamic performance and stability. Flow separation was observed along the front and rear end of the roof.

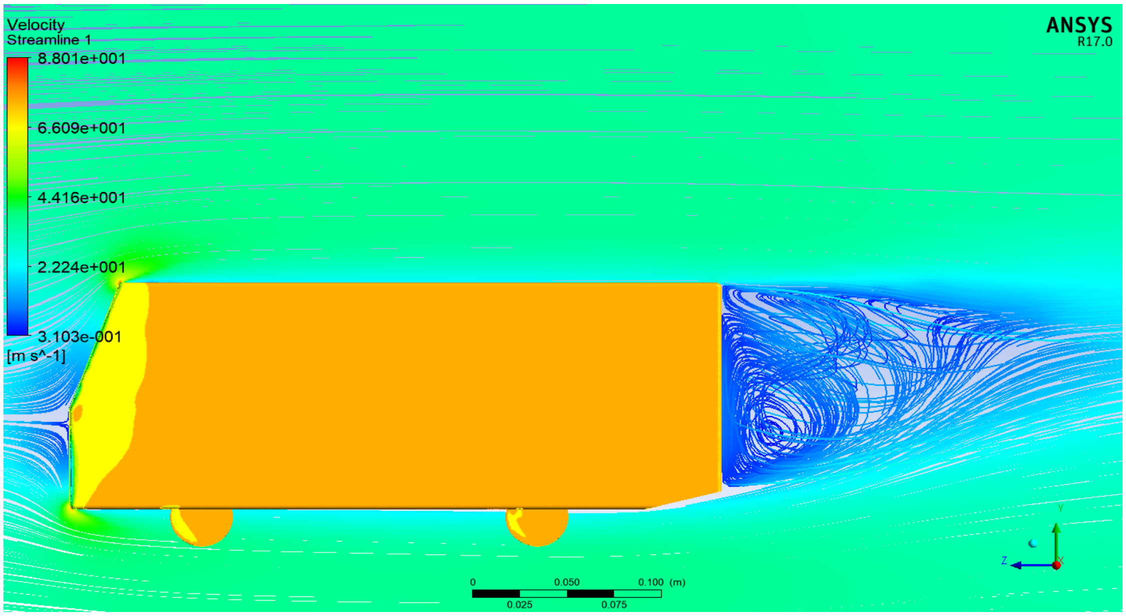

Figure 5. 27: Velocity contour of model one at 120 kmph

Model one is the modification of the baseline model by increasing the inclination angle of the windshield. The test procedure was the same as baseline model. The flow separation at the front roof end of the bus has reduced due to increase the inclination angle of windshield. However, the low-velocity area colored by blue in the wake region is high almost similar to the baseline model. From the velocity streamline contour (Figure 5.25, 5.26 and 5.27), it can be seen that the wake region gets stronger and wider as the speed increases. Also, the velocity of air is reduced at the front due to the air hitting the bus. Further, it is also reduced behind the bus due to low pressure.

In terms of the pressure coefficient, it is not expected to see significant difference compared to the baseline model. Figure 5.28 shows the surface pressure distribution of model I along the symmetry plane and it indicates that the maximum value of pressure is at the front surface of bus where the stagnation point is generated. After the front of the bus roof surface the pressure decreases due to its streamlined shape and then increases gradually to rear roof of the bus. The pressure on the floor of the vehicle is lowest at the front of the bus then increased rapidly after stagnation point. Finally increases gradually to rear of the bus.

After evaluating the aerodynamic performance of the baseline model, it is found that there is very much scope for modification so as to improve the coefficient of drag and fuel efficiency.

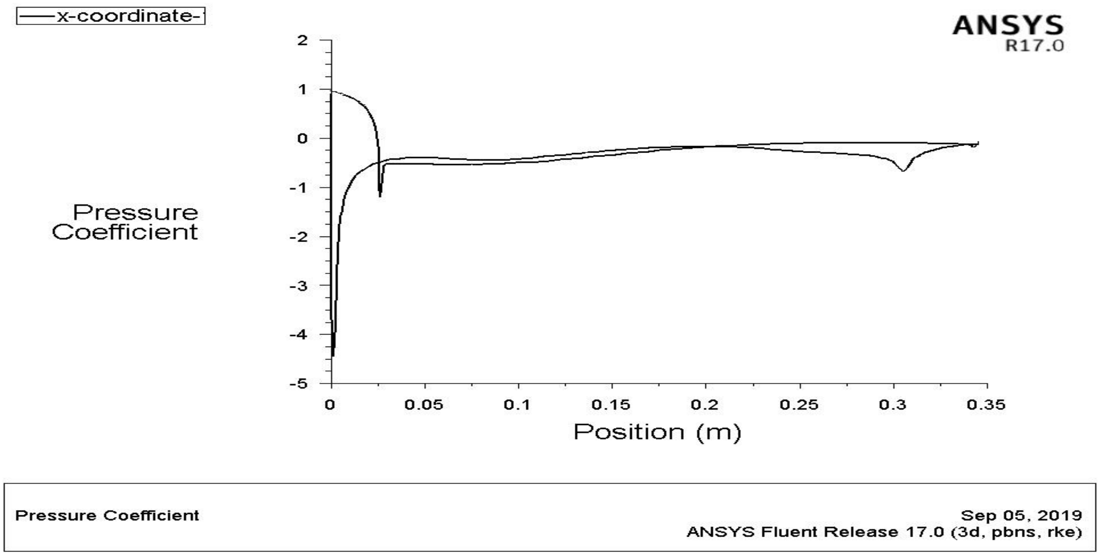

Figure 5. 28: Surface pressure distribution along the symmetry plane of model one

5.1.3 Model II Results

Model II designed with a curved front surface and smooth rounded corners on the front and rear end of the roof. Modification is done in the front and rear end of the roof based on the results from baseline model and model one.

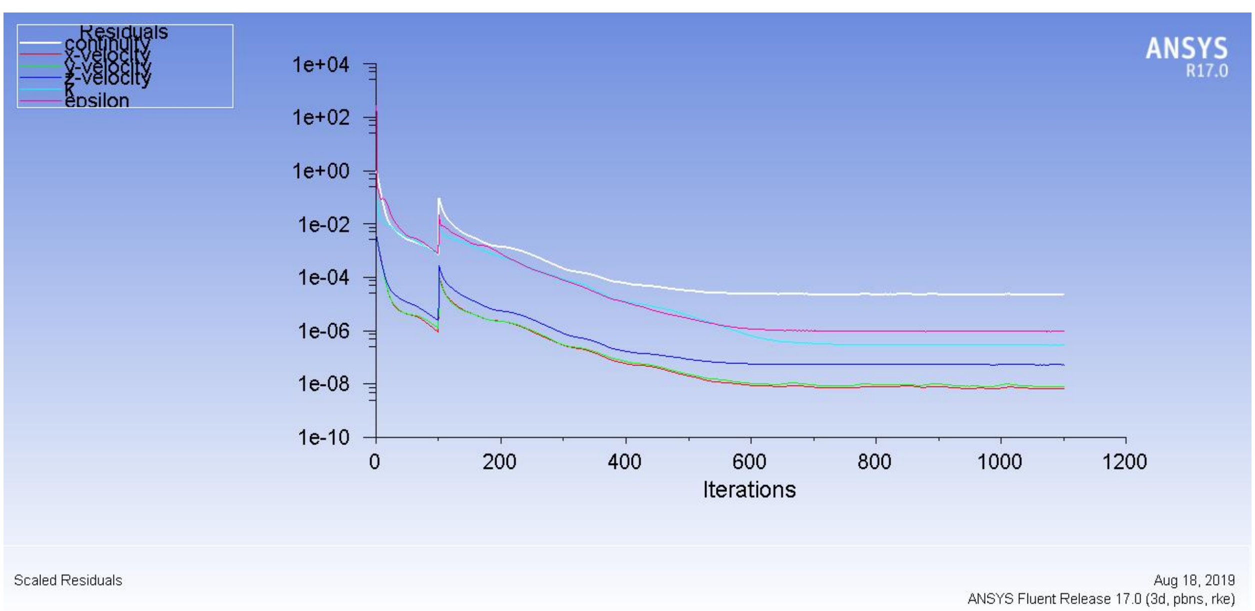

Figure 5. 29: Scaled residuals of model II

The scaled residuals graph shown in Figure 5.29 is evident that the convergence for model two was achieved after 600 iterations. The residuals are jumped off at the 101st iteration because the scheme has been changed from first-order upwind to second-order upwind in order to reach convergence much faster.

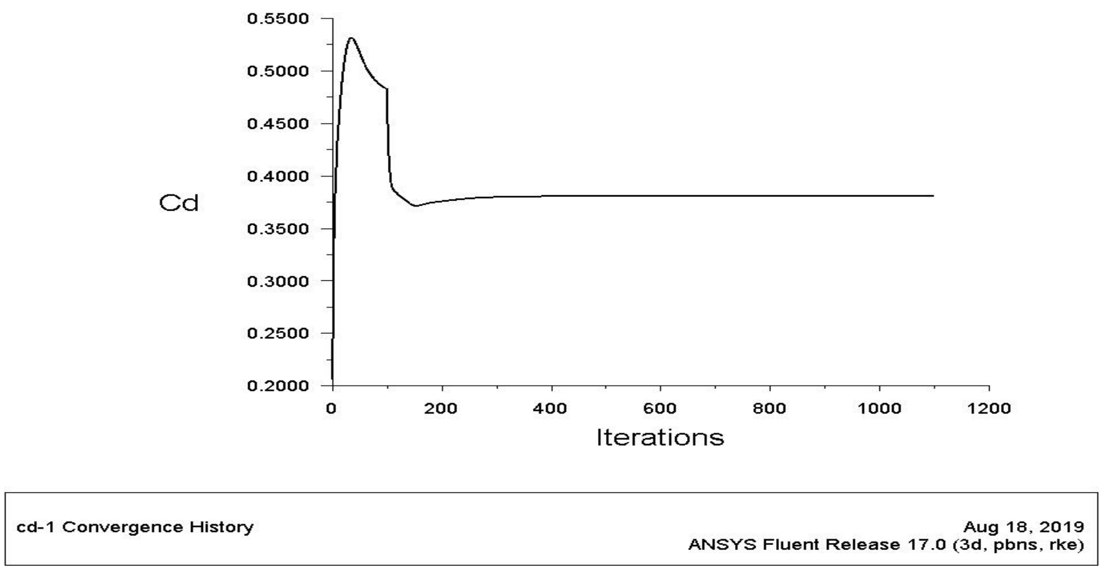

Figure 5. 30: Drag coefficient of model two at 80 kmph

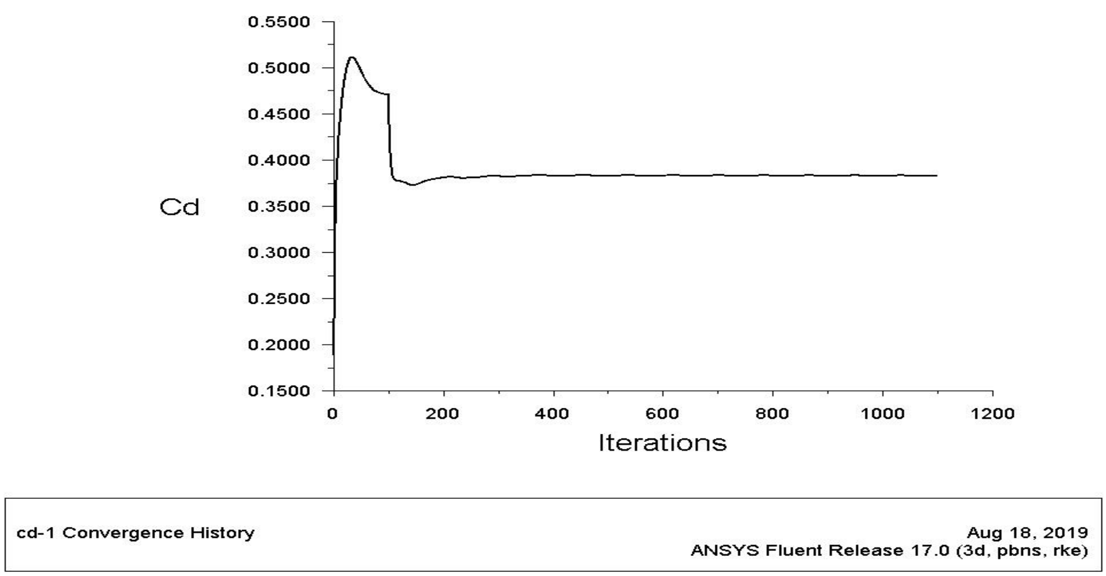

Figure 5. 31: Drag coefficient of model two at 100 kmph

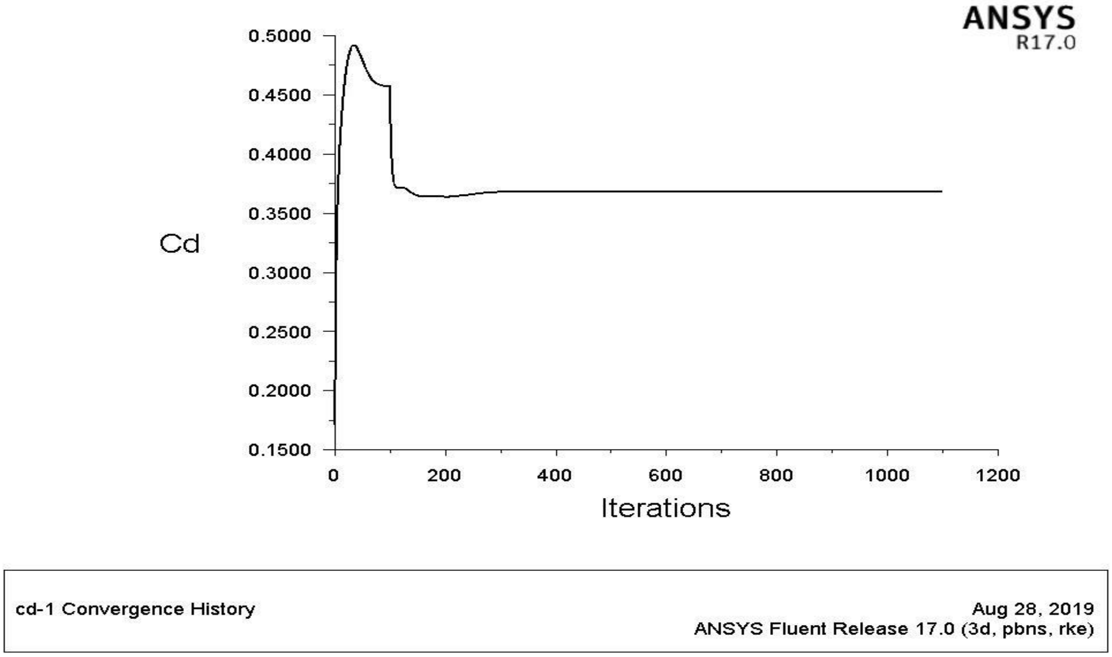

Figure 5. 32: Drag coefficient of model two at 120 kmph

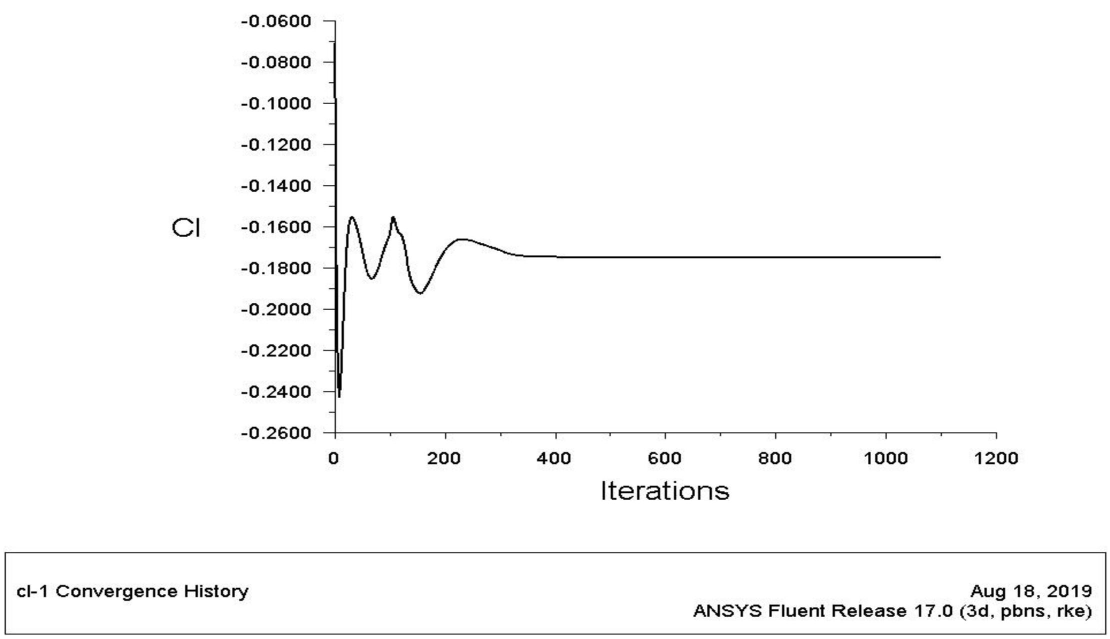

Figure 5. 33: Lift coefficient of model two at 80 kmph

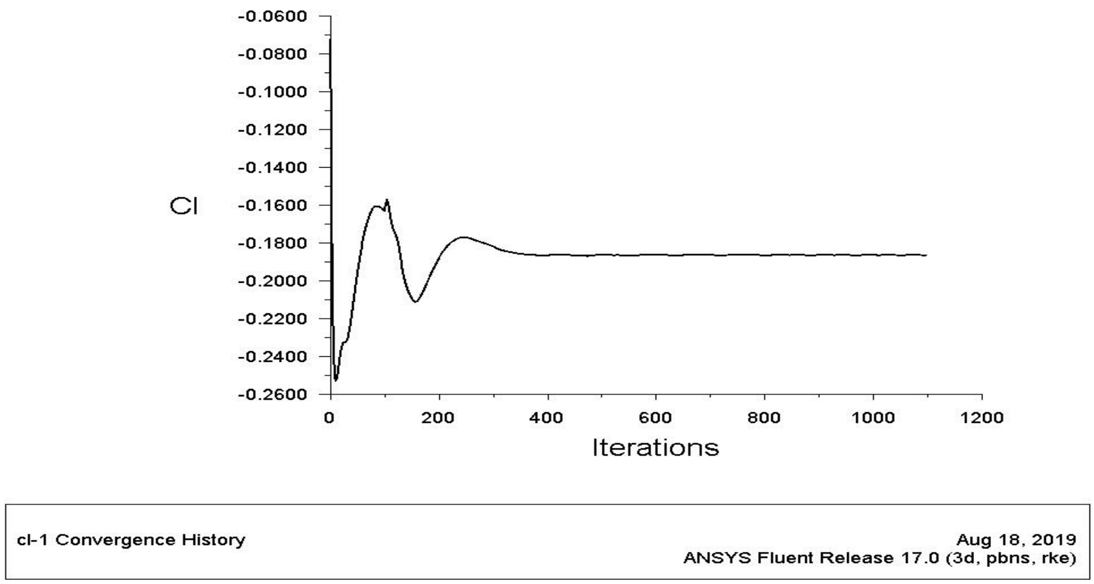

Figure 5. 34: Lift coefficient of model two at 100 kmph

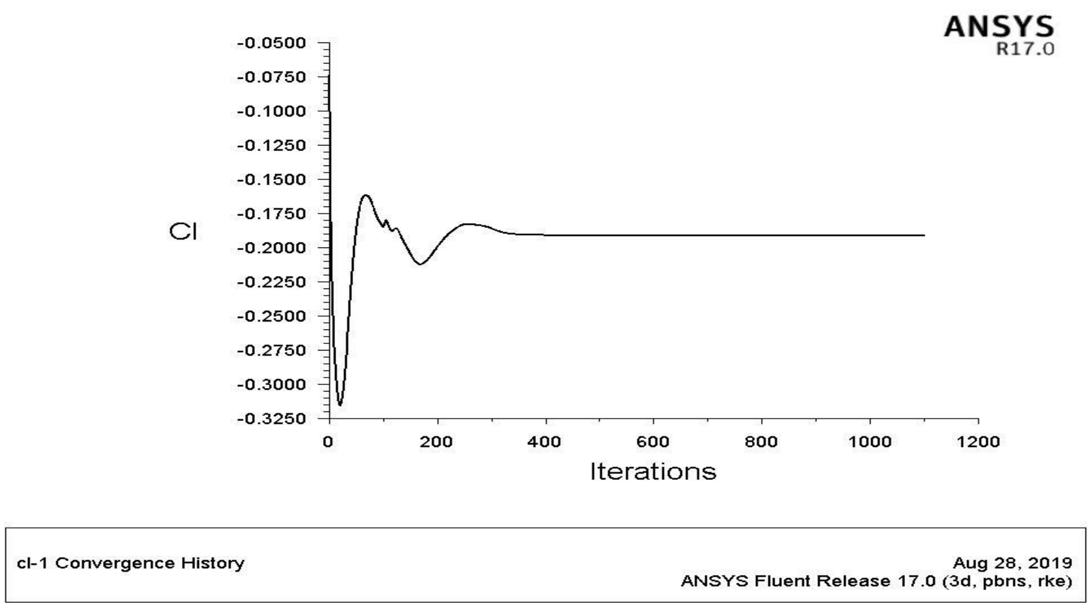

Figure 5. 35: Lift coefficient of model two at 120 kmph

All the above graphs (Figures 5.30-5.35) indicates that the drag and lift coefficients of model II at speed of 80, 100, and 120 kmph, here the drag and lift coefficients are summarized in table 5.3 for model II.

Table 5. 3: Summary of drag and lift coefficient for model II at different speeds

Model	Speed (kmph)	C_d	C_l
Model Two	80	0.38114	-0.17429
	100	0.38354	-0.18612
	120	0.38412	-0.19048

Figures 5.30-5.35 and Table 5.3 showed that the result of the drag and lift coefficients of model II at three different speeds (80, 100, and 120 kmph) when simulated the bus model by realizable turbulence model in ANSYS Fluent. As shown in the figures, both the drag and lift coefficients converge before the 400th iteration. The drag coefficients were calculated to be 0.38114, 0.38354, and 0.38412 as shown in table 5.3 and the lift coefficients were -0.17429, -0.18612 and -0.19048 at different speed of 80, 100, and 120 kmph, respectively.

The drag coefficient of model two (Table 5.3) is reduced than both the baseline model (Table 5.1) and model I (Table 5.2). The drag coefficient has reduced from 0.72881 (the average drag coefficient at 80, 100, and 120 kmph speeds) for the baseline model to 0.38293 (the average drag coefficient at 80, 100, and 120 kmph speeds) for model II, thus the average reduction in C_d is 47.46%. This deviation of the drag coefficient of the model II with respect to the baseline model will give a clear idea about how much the drag force is affected by outer body modification. Model II designed with a curved front surface and smooth rounded corners on the front and rear end of the roof. The lift coefficient of model II decreases with an increasing speed which results high downward force, which is very necessary for vehicle stability at higher speed. However, there is an increment in lift coefficient from the baseline model.

The pressure drag arises from the pressure difference or more generally from non-uniform pressure distribution around the model. The stagnation pressure at the front of the body represented by the red area is more than that acting on the rear of the body, so resultant force acting on the body in the direction of relative motion exists.

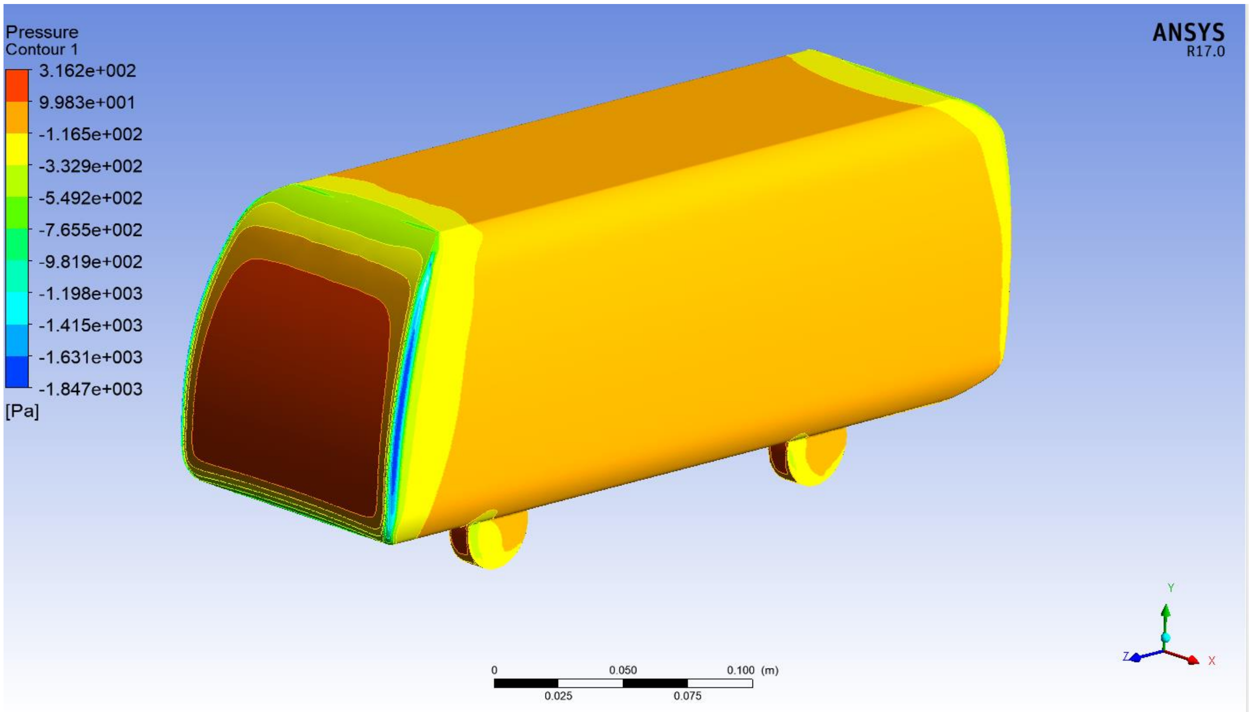

Figure 5. 36: Pressure contour of model two at 80 kmph

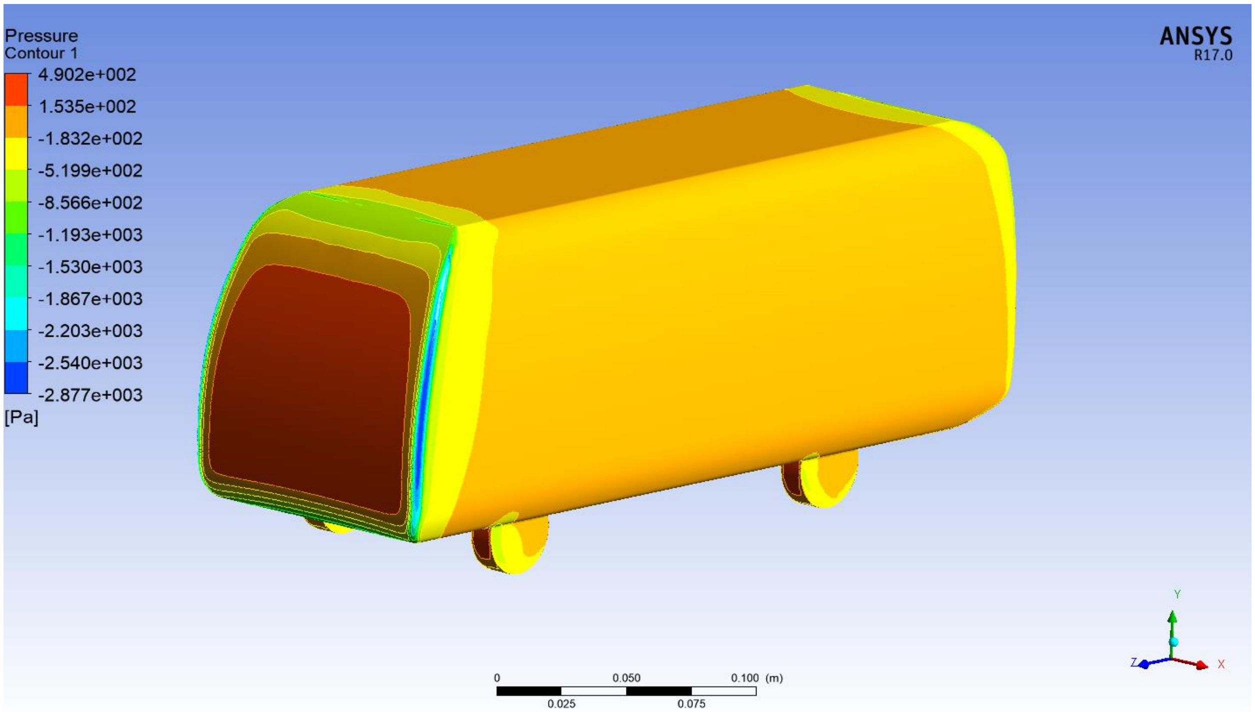

Figure 5. 37: Pressure contour of model two at 100 kmph

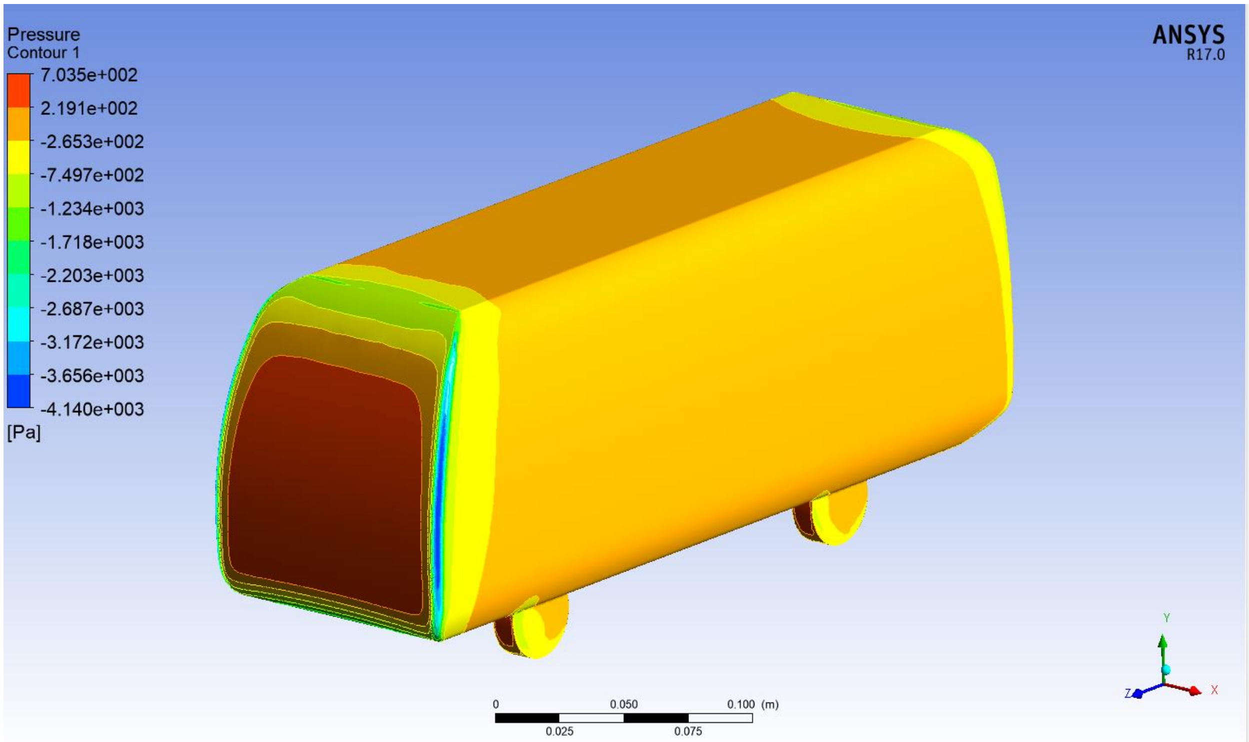

Figure 5. 38: Pressure contour of model two at 120 kmph

The contour of pressure distribution shown in Figures 5.36, 5.37 and 5.38 indicates the level of pressure effect on the surface of the bus. The concept of pressure drags happen when there are two different areas with different level of pressure. In this case, the area on the front of the bus's body (stagnation point colored by red) is relatively higher than the pressure level at the back of the bus. The maximum pressure increases with increasing speed. The pressure difference between the modified design (Model II) is lower than the baseline model. This fact suggests that the proposed modification results in a lower pressure difference in the modified design.

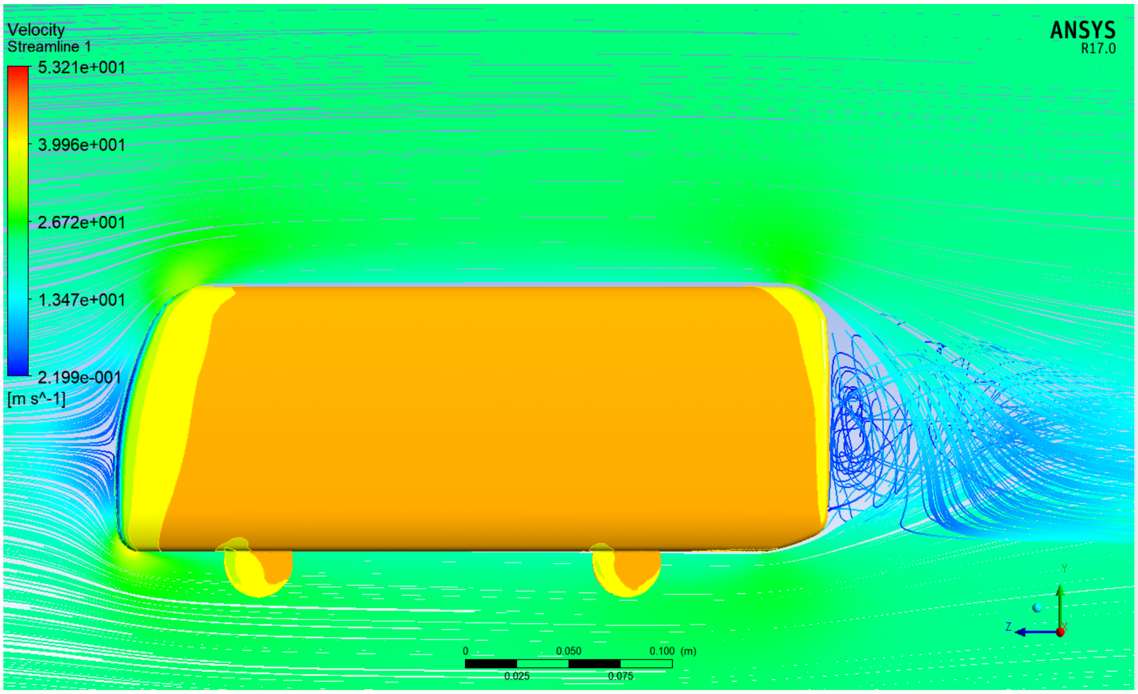

Figure 5. 39: Velocity contour of model two at 80 kmph

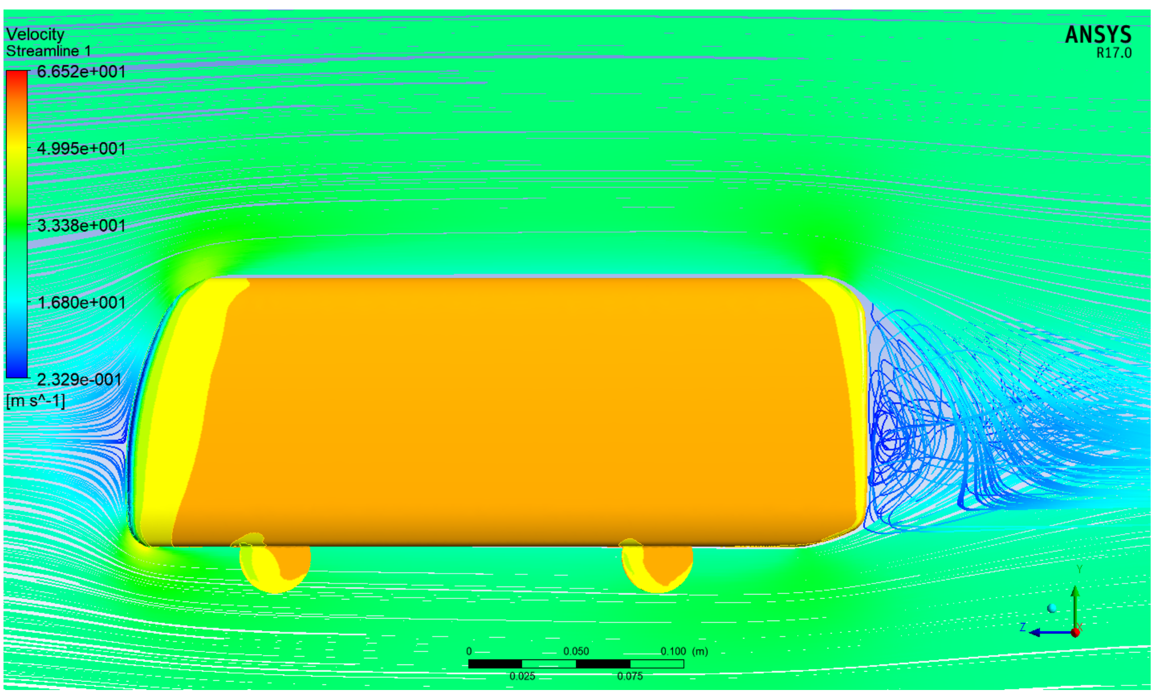

Figure 5. 40: Velocity contour of model two at 100 kmph

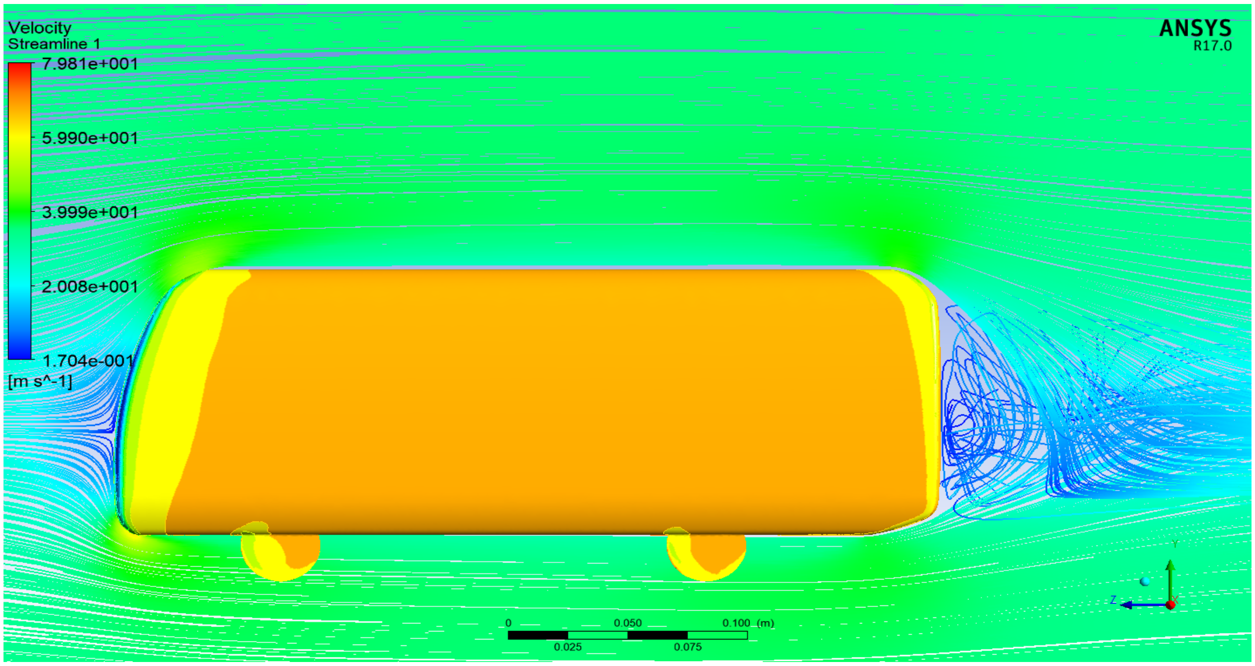

Figure 5. 41: Velocity contour of model two at 120 kmph

Model II is the modification of the baseline model in which the angle of windshield and cowl has been changed. The front top and rear roof end, windshield and cowl are made curvy as compared to both the baseline model and model I. The test procedure was the same as the baseline model and model I. The flow separation at the front top and rear roof end parts of the bus has reduced due to the fillet added on the end parts. Consequently, which minimize the low-velocity area in the wake region and delay the turbulence zone away from the bus model. Refer Figure 5.39, 5.40 & 5.41 and compared with Figure 5.11, 5.12 & 5.13. From the velocity streamline contour, It can be seen that the wake region gets stronger and wider as the speed increases.

The pressure coefficient graph (Figure 5.42) shows the surface pressure distribution along the symmetry plane of model II and it indicates that the maximum value is at the front surface of the bus where the stagnation point is generated. It can be noted that the pressure on the front of the bus roof decreases rapidly due to its streamlined shape and then increases gradually and again it decreases rapidly at the rear roof end then finally increases. The pressure on the floor of the vehicle is lowest at the front of the bus then increased rapidly after the stagnation point. Finally increases gradually to rear of the bus. Therefore, it is important to analyze the high and low areas of pressure present on the bus and how these sections affected the airflow and coefficient of drag.

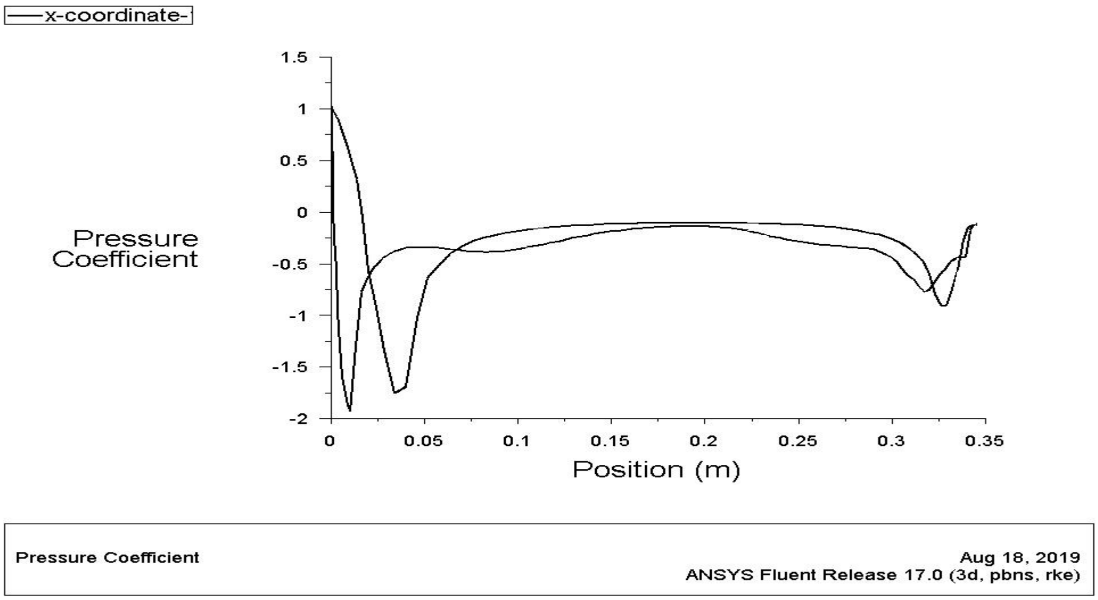

Figure 5. 42: Surface pressure distribution for model II

5.1.4 Model III Results

Model three designed with a more curved front surface and more smooth rounded corners on the front and rear end of the roof than other models as shown in Figure 3.5. Result of scaled residuals, drag and lift coefficient, pressure and velocity contour at speed of 80, 100 and 120 kmph for model III are presented below.

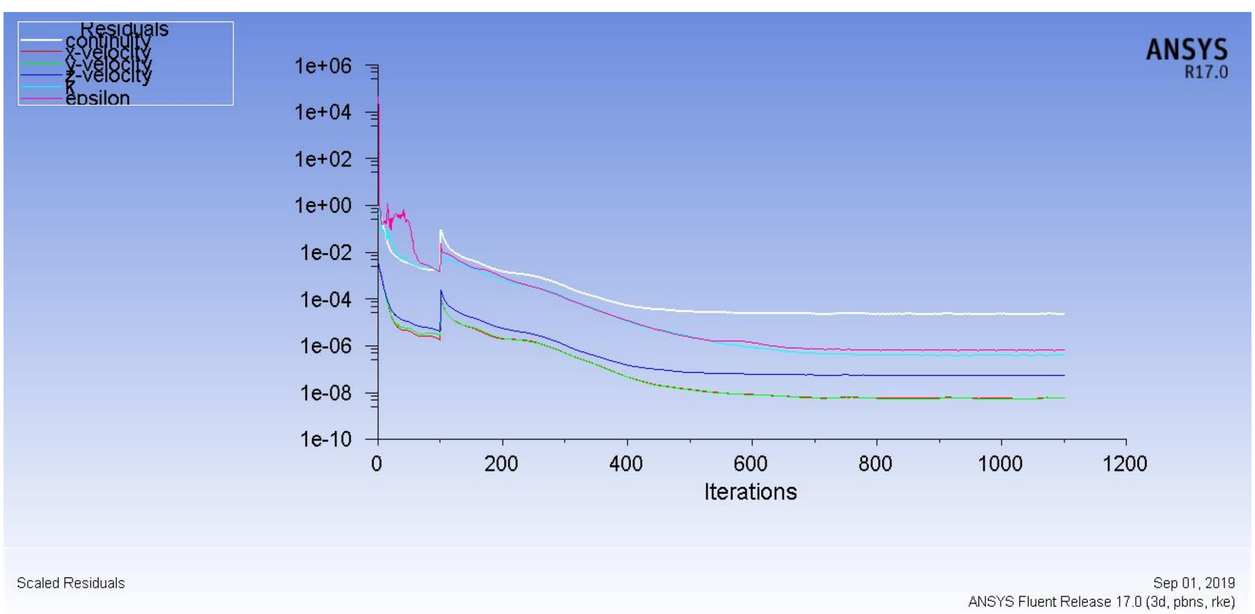

Figure 5. 43: Scaled residuals of model III

The numerical solver is an iterative method so the residual values between two steps can be set as the convergence criteria. Initially, it was 10^{-5}.

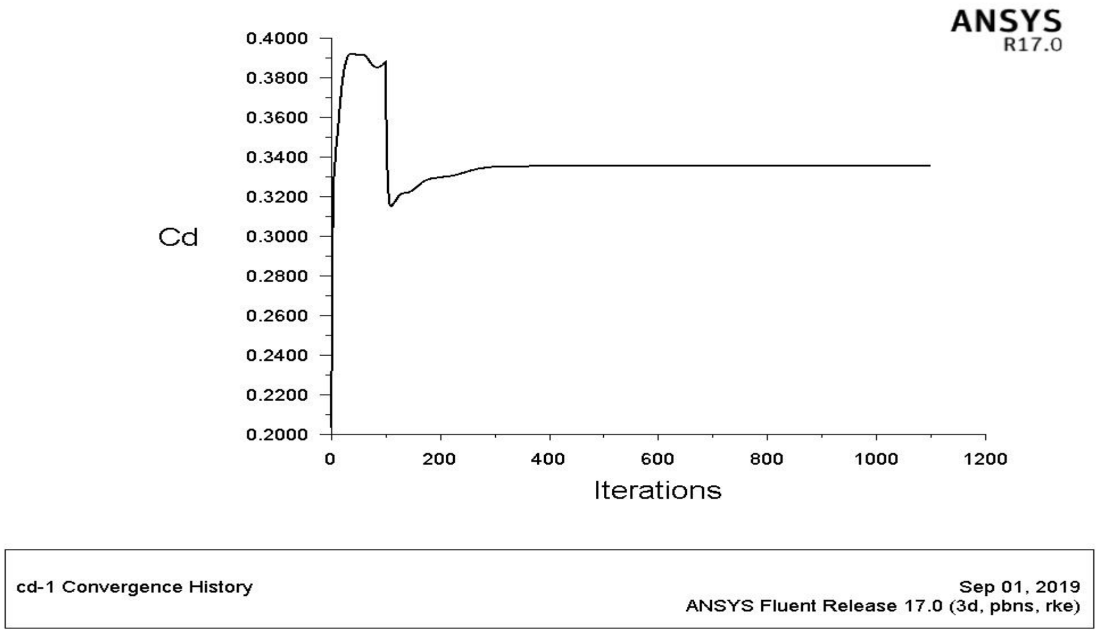

Figure 5. 44: Drag coefficient of model three at 80 kmph

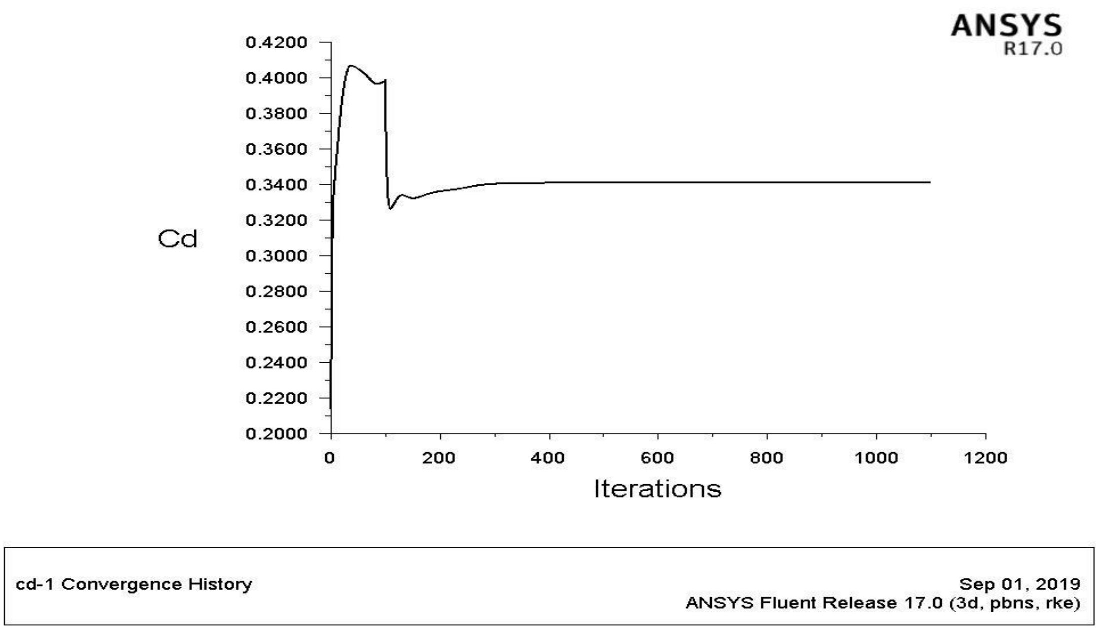

Figure 5. 45: Drag coefficient of model three at 100 kmph

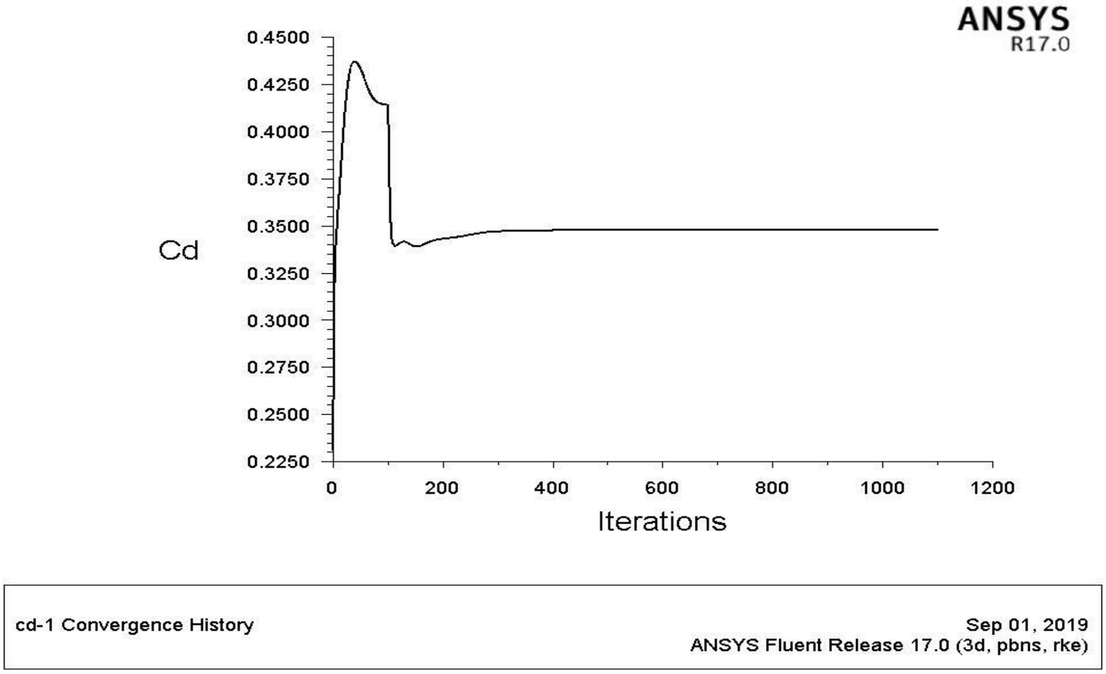

Figure 5. 46: Drag coefficient of model three at 120 kmph

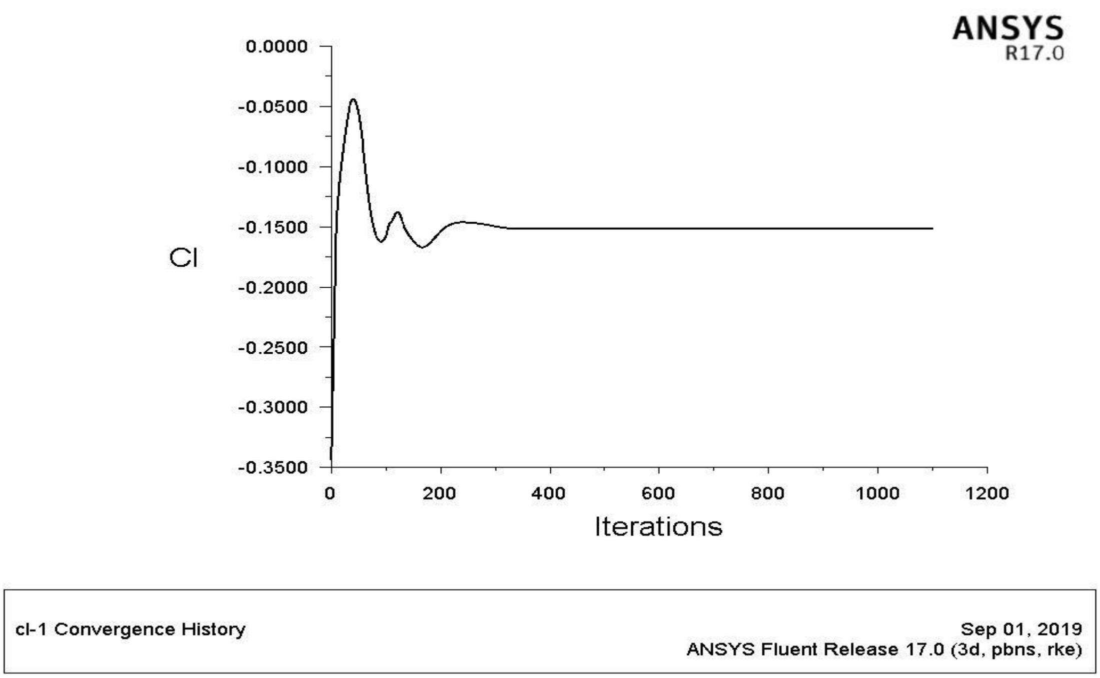

Figure 5. 47: Lift coefficient of model three at 80 kmph

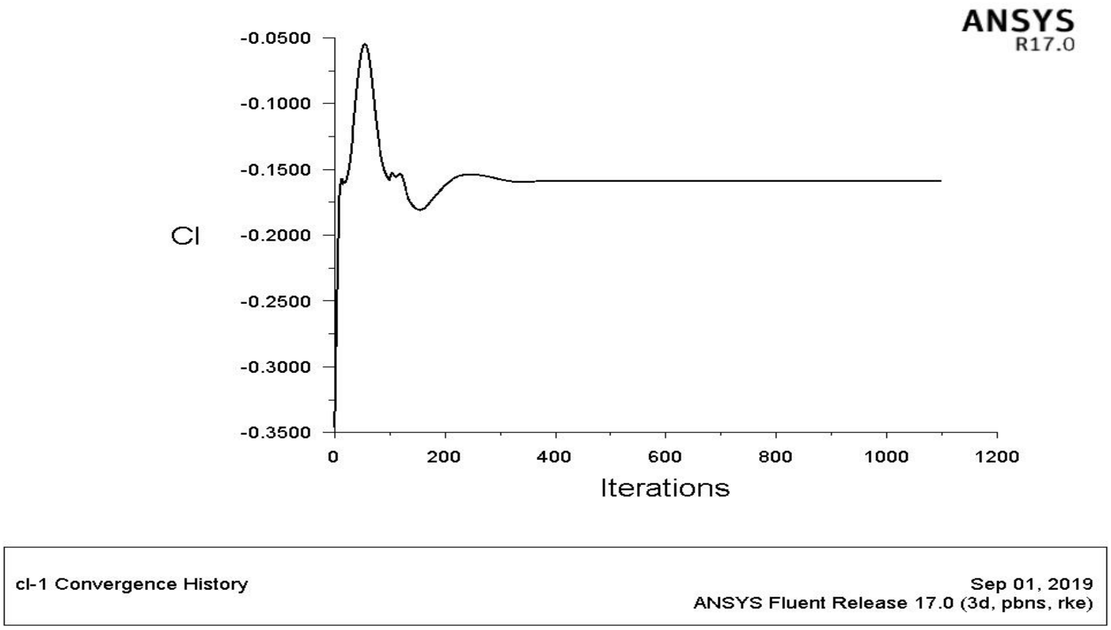

Figure 5. 48: Lift coefficient of model three at 100 kmph

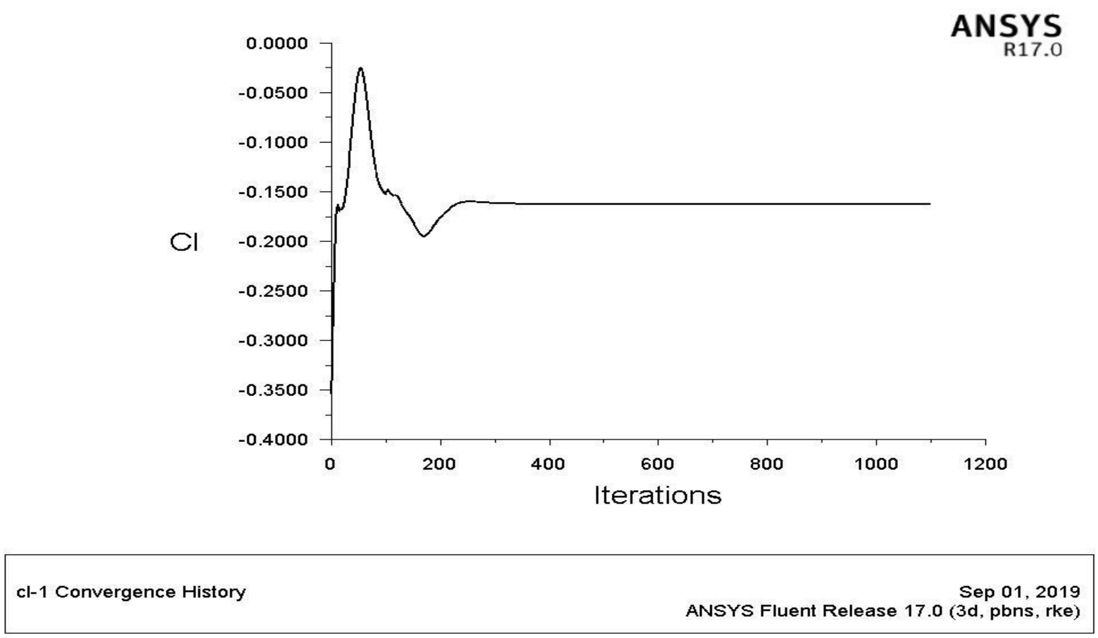

Figure 5. 49: Lift coefficient of model three at 120 kmph

All the drag coefficient graphs shown in Figure 5.44, 5.45 and 5.46 and lift coefficient graphs shown in Figure 5.47,5.48 and 5.49 of model III at speed of 80, 100 and 120 kmph are summarized in Table 5.4.

Table 5. 4: Summary of drag and lift coefficient of model three at different speeds

Model	Speed (kmph)	Cd	Cl
Model Three	80	0.33598	-0.15144
	100	0.34142	-0.15861
	120	0.34813	-0.16168

The drag coefficient of model III (Figure 5.44-5.46) is reduced than both the baseline model (Table 5.1), model I (Table 5.2) and model II (Table 5.3). The drag coefficient has reduced from 0.72881 (the averaged drag coefficient at 80, 100, and 120 kmph speeds) for the baseline model to 0.34184 (the averaged drag coefficient at 80, 100, and 120 kmph speeds) for model III, thus the average reduction in C_d is 53.09%. This deviation of the drag coefficient of the model III is higher than the drag deviation of model II (47.46%) from the baseline which implies that model III is more streamlined than model II. Also, the drag coefficient increases with increasing speed, these also hold true for model III.

Figure 5.44-5.49, shows how the drag and lift coefficients converge with each iteration. Both the drag and lift coefficients of model III converge before the 400th iteration. The lift coefficient of model III decreases with increasing speed which results high downward force, which is very necessary for vehicle stability at higher speed. However, there is a large increment in lift coefficient from the baseline model which leads the bus to be unstable at higher speed.

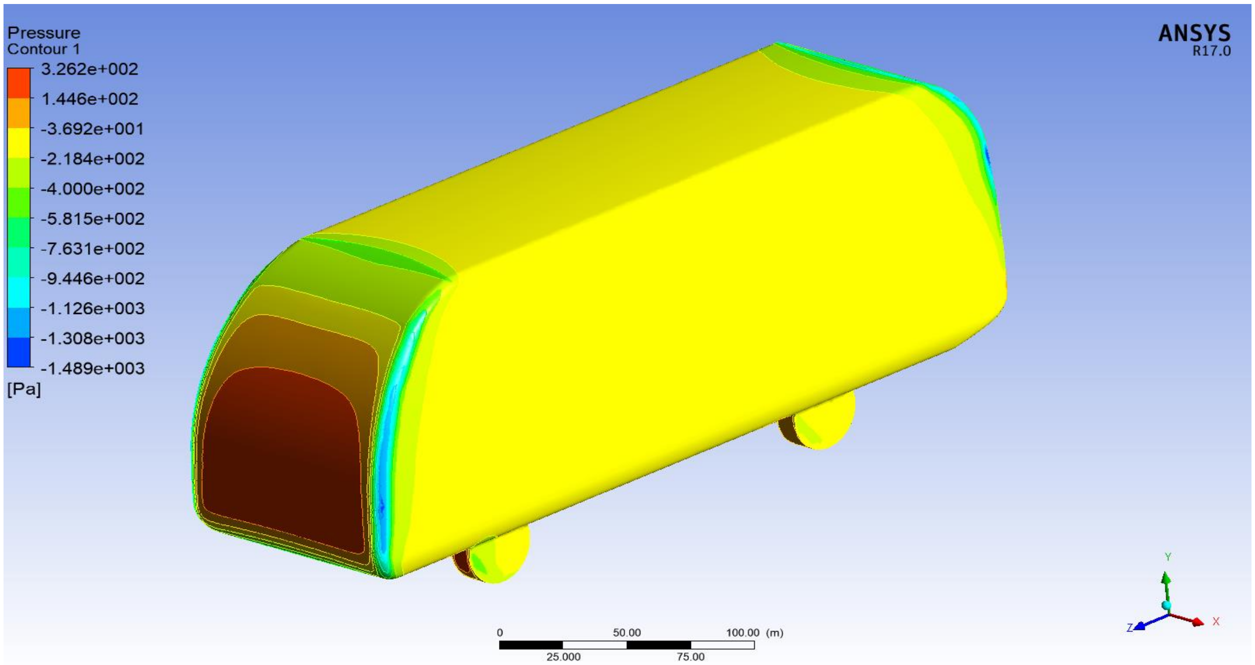

Figure 5. 50: Pressure contour of model three at 80 kmph

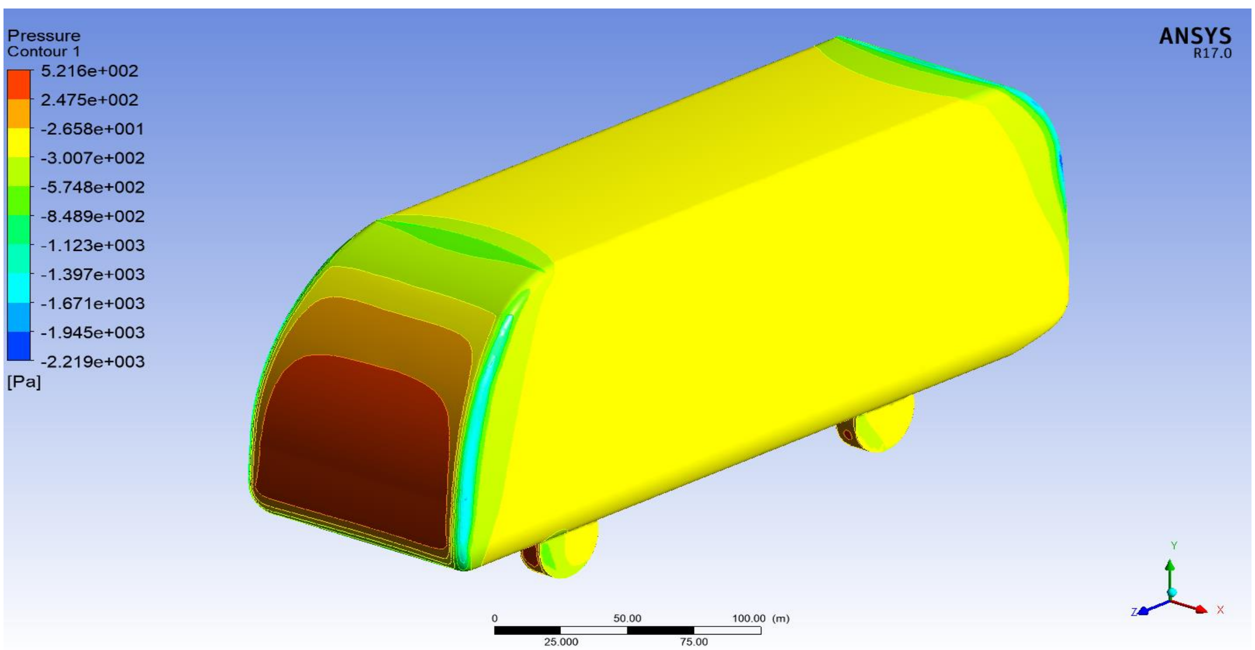

Figure 5. 51: Pressure contour of model three at 100 kmph

The contour of pressure distribution shown in Figures 5.50, 5.51 and 5.52 indicates the level of pressure effect on the surface of the bus. From the figures, it can be seen how the pressure increases with increasing speed. The drag coefficient of model three increases with the increase in speed.

The increase in the amount of drag is because of the increase in the amount of forwarding resistant force which increases the pressure on the vehicle.

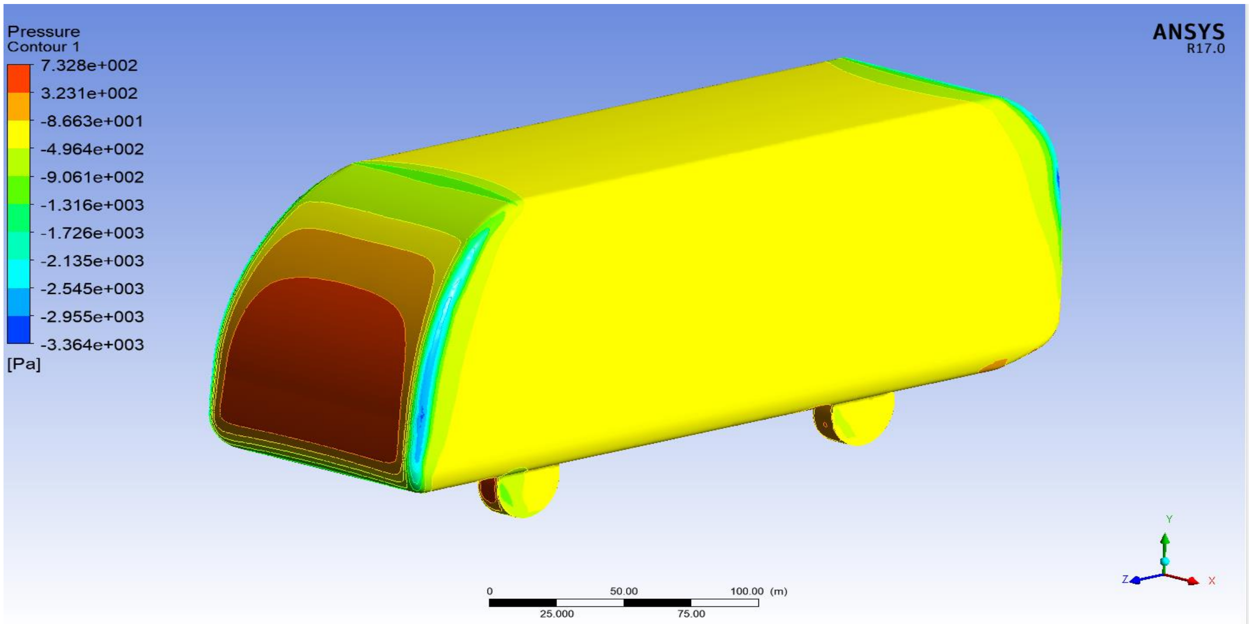

Figure 5. 52: Pressure contour of model three at 120 kmph

The area of high stagnation pressure at the front of the bus has reduced. Also, the pressure difference of model III is lowest than both the baseline model, model I and model II. This fact suggests that the proposed modification results in the lowest pressure difference in the modified design.

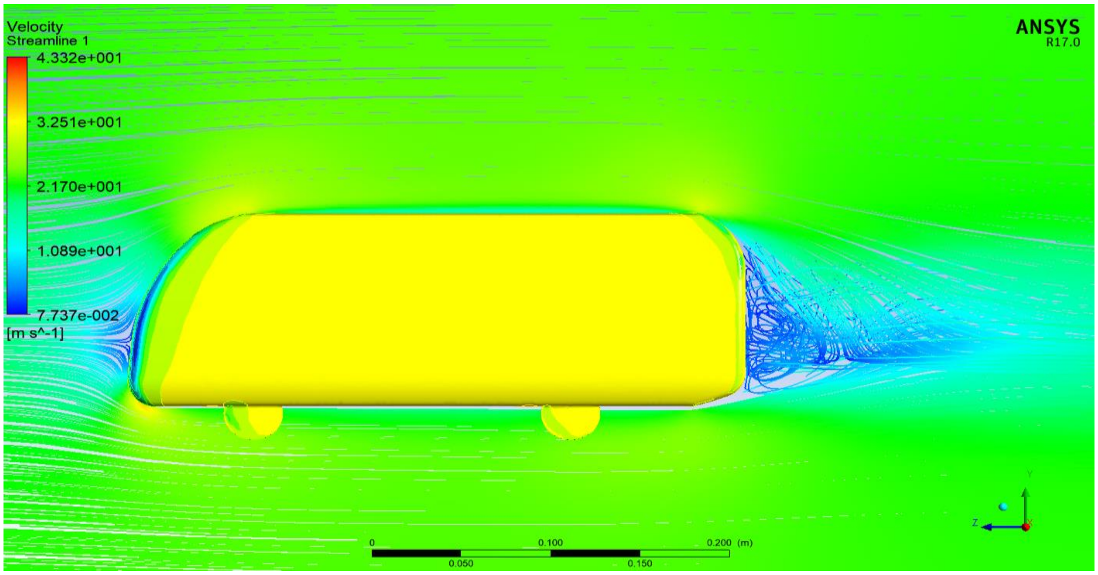

Figure 5. 53: Velocity contour of model three at 80 kmph

A streamlined front end that allows better airflow will effectively improve the aerodynamic performance of the vehicle.

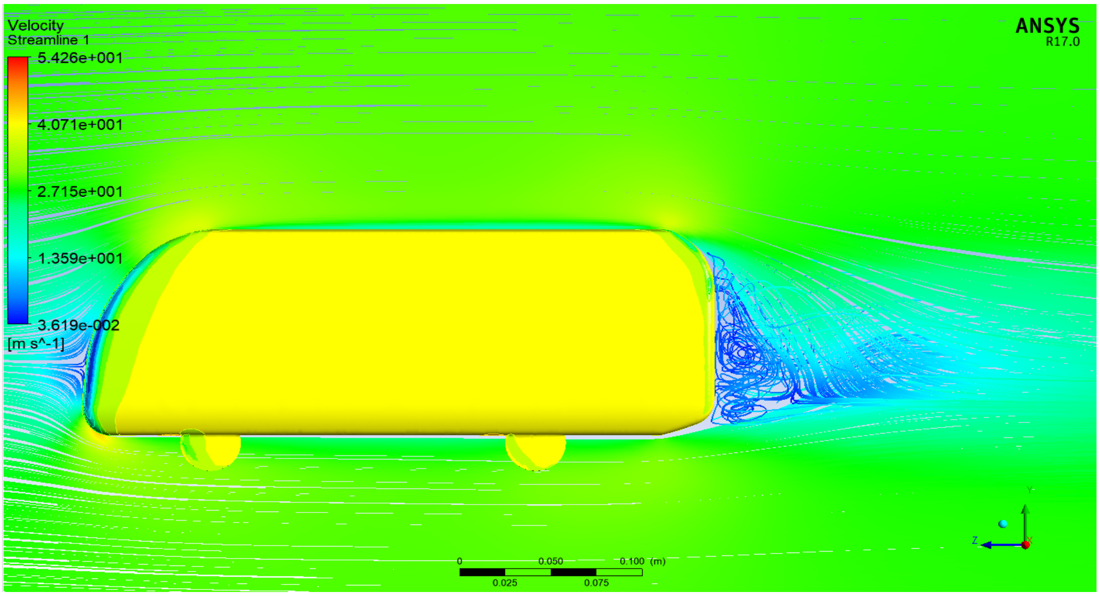

Figure 5. 54: Velocity contour of model three at 100 kmph

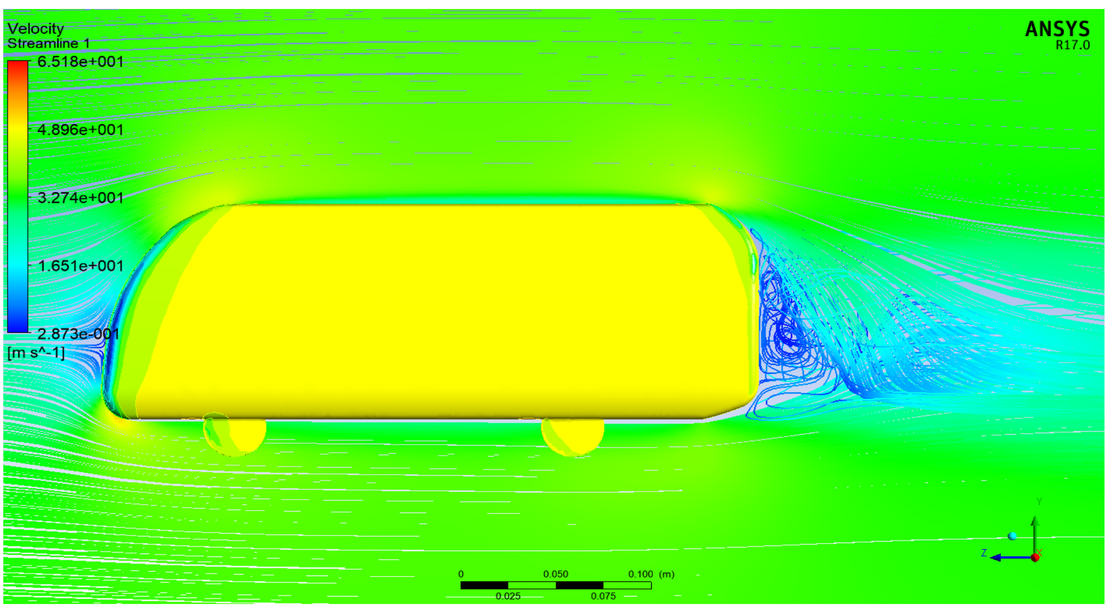

Figure 5. 55: Velocity contour of model three at 120 kmph

Model III is the modification of model II in which the front top and rear roof end, windshield, and cowl are made curvier as compared to model II. These the streamlined front top and rear roof end and windshield allow better airflow will effectively improve the aerodynamic performance of the vehicle. The simulation and other analyses carried out are the same as all other models. From the velocity streamline contour (Figure 5.53, 5.54 and 5.55) shows that the wake region gets stronger and wider as the speed increases. However, the wake region of model III is smaller than all other models. When observing the streamlines at the bus midplane it can be seen that the flow is more streamlined and the wake region behind the bus has reduced drastically thus there is a significant reduction in the coefficient of drag for model III.

In terms of the pressure coefficient of model III is no a significant difference compared to model II. Figure 5.56 shows the surface pressure distribution on the body of the bus along the symmetry plane of model III and it indicates that the maximum value is at the front surface of the bus where the stagnation point is generated. It can be noted that the pressure on the front of the bus roof decreases more rapidly due to its streamlined shape and then increases gradually and again it decreases due to streamlined shape of rear roof end and finally increases due to wake zone.

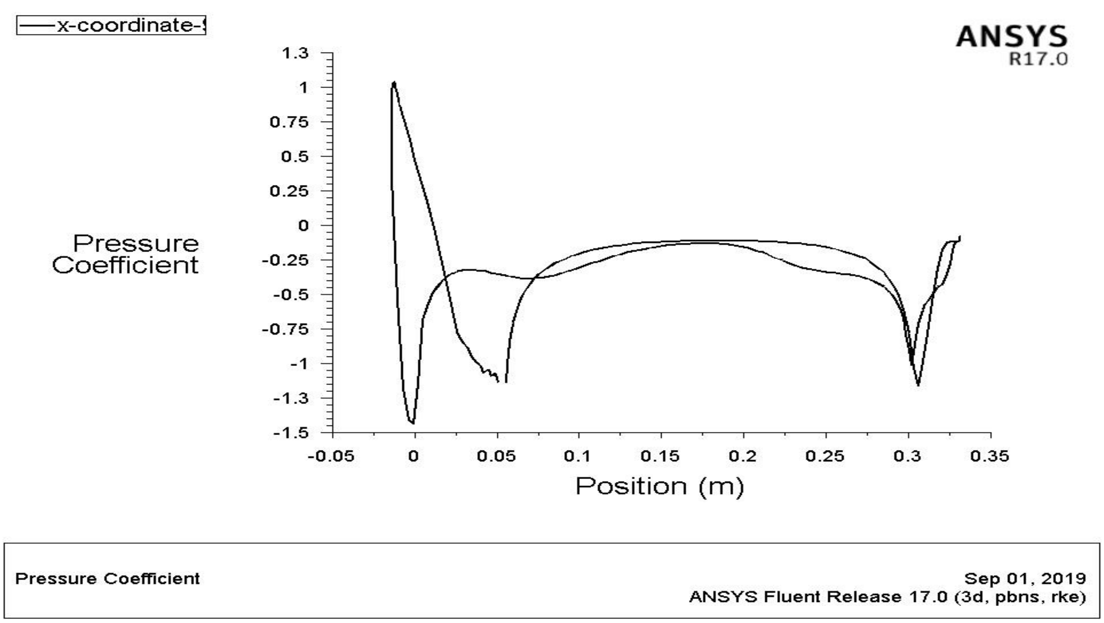

Figure 5. 56: Surface pressure distribution along the symmetry plane for model III

On the windshield close to the roof the velocity is increasing and high value is reached at the roof edge. Along the roof, the velocity damps into the free stream and pressure are normalizing until the back where separation occurs due to the geometry.

5.1.5 Results of Model IV (Model III with rear spoiler)

Model four is just a model three with the rear spoiler, which is a drag reduction device added at rear end of the roof. Rear spoiler diffuses the airflow passing a vehicle, which minimizes the turbulence at the rear of the vehicle, adds more downward pressure to the back end and reduces lift acted on the rear. The rear spoilers contribute to major aerodynamic stability of the car (Hu and Wong, 2011). The same procedure has been followed as the previous models. The solution has started with first-order upwind for the first 100 iterations to accelerate the convergence and then continued with the second-order upwind scheme.

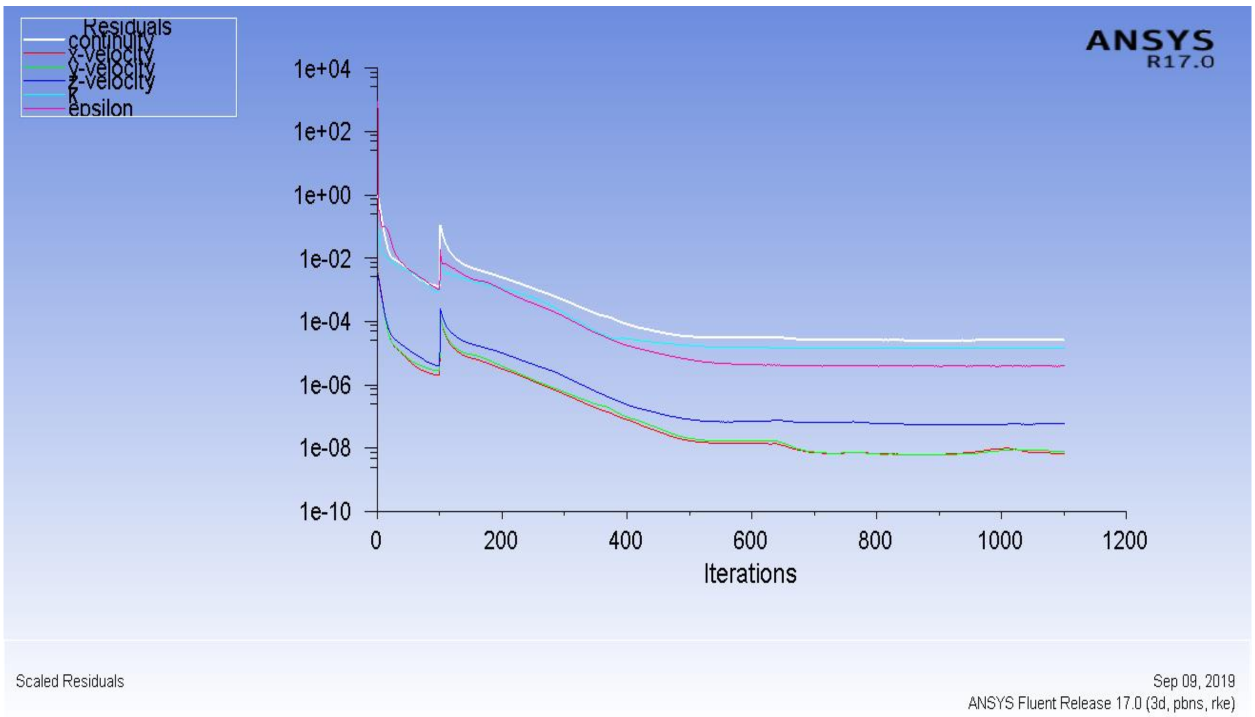

Figure 5. 57: Scaled residuals of model IV

The scaled residuals for model IV shows how the parameters converge with each iteration. It is evident that the convergence for this model achieved before 700 iterations. Result of scaled residuals (Figure 5.57), drag and lift coefficients, pressure and velocity contour at speed of 80, 100 and 120 kmph for model IV are presented in Figure 5.58 to 5.63.

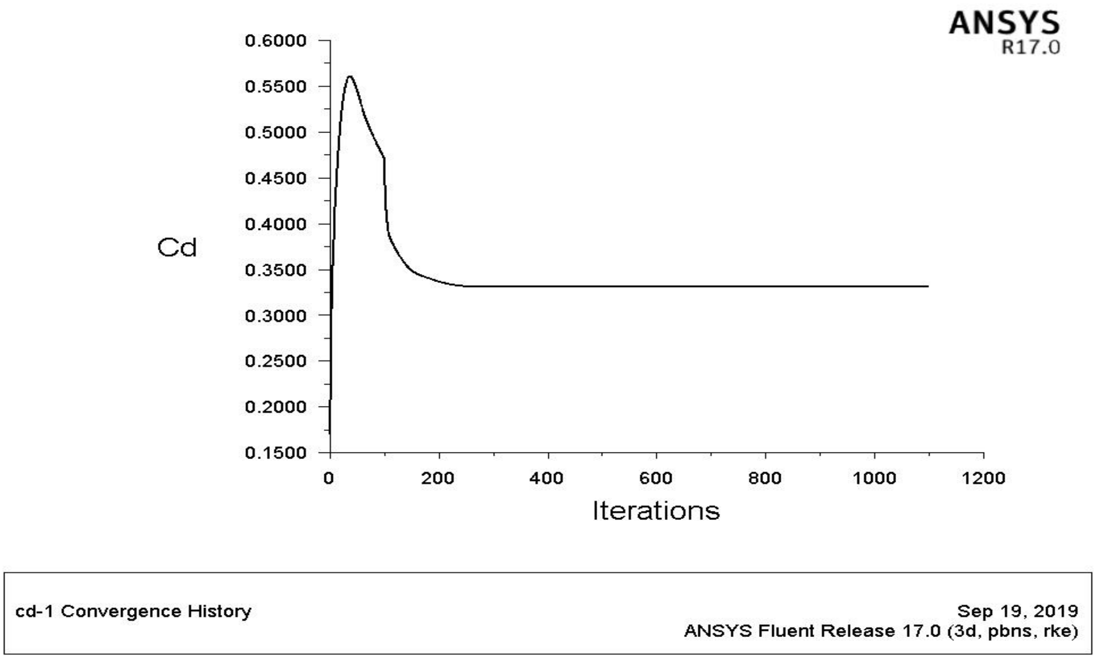

Figure 5. 58: Drag coefficient of model four at 80 kmph

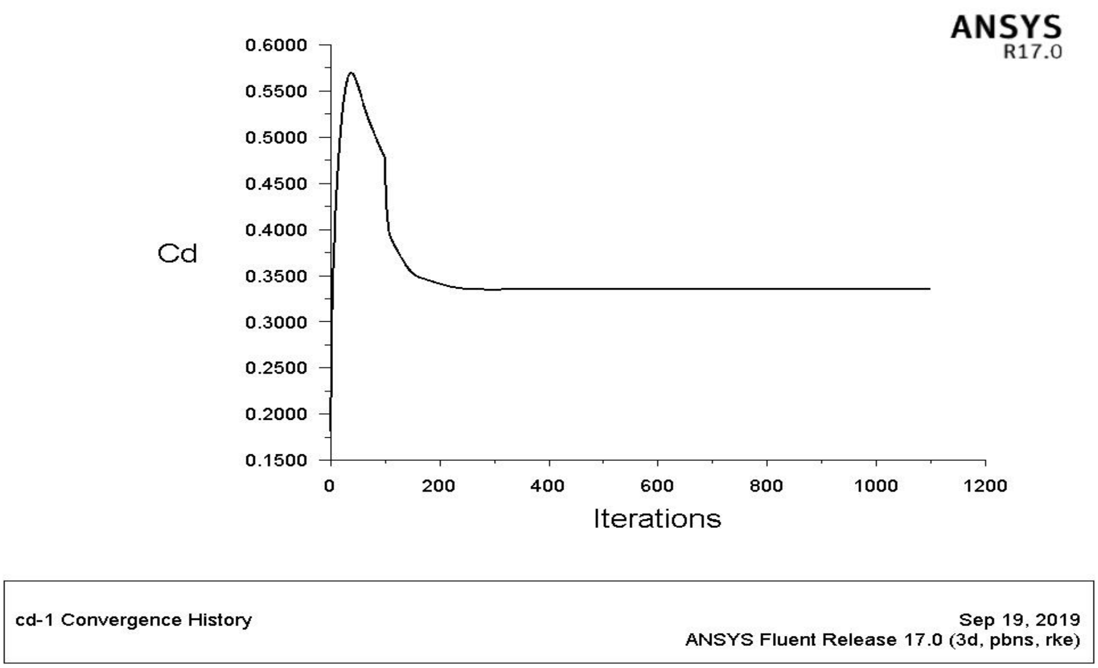

Figure 5. 59: Drag coefficient of model four at 100 kmph

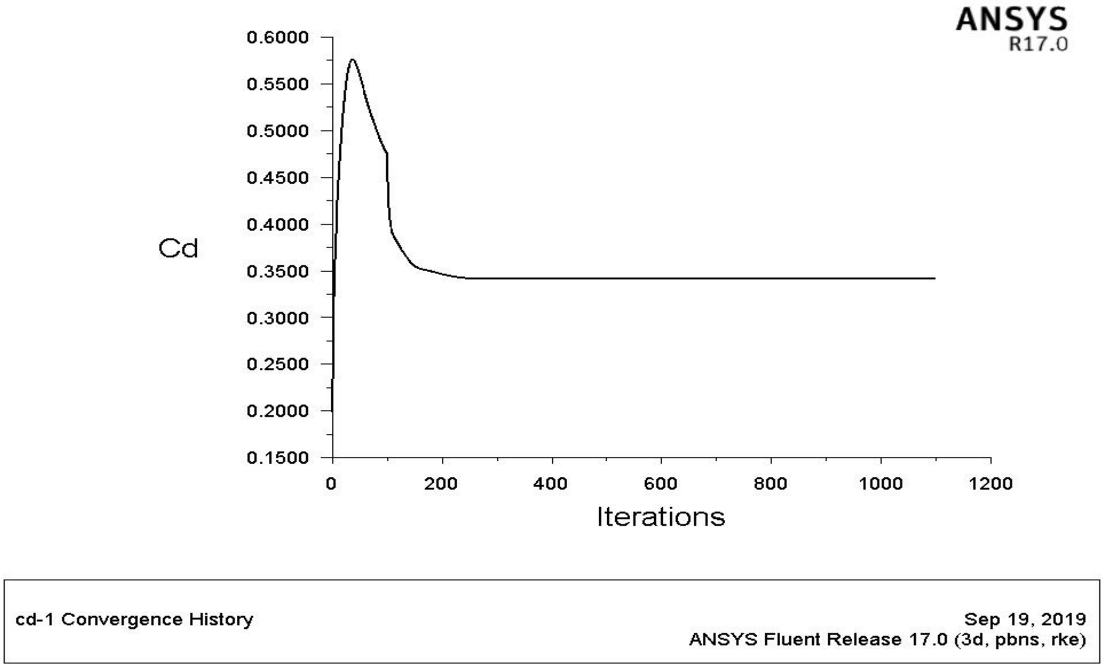

Figure 5. 60: Drag coefficient of model four at 120 kmph

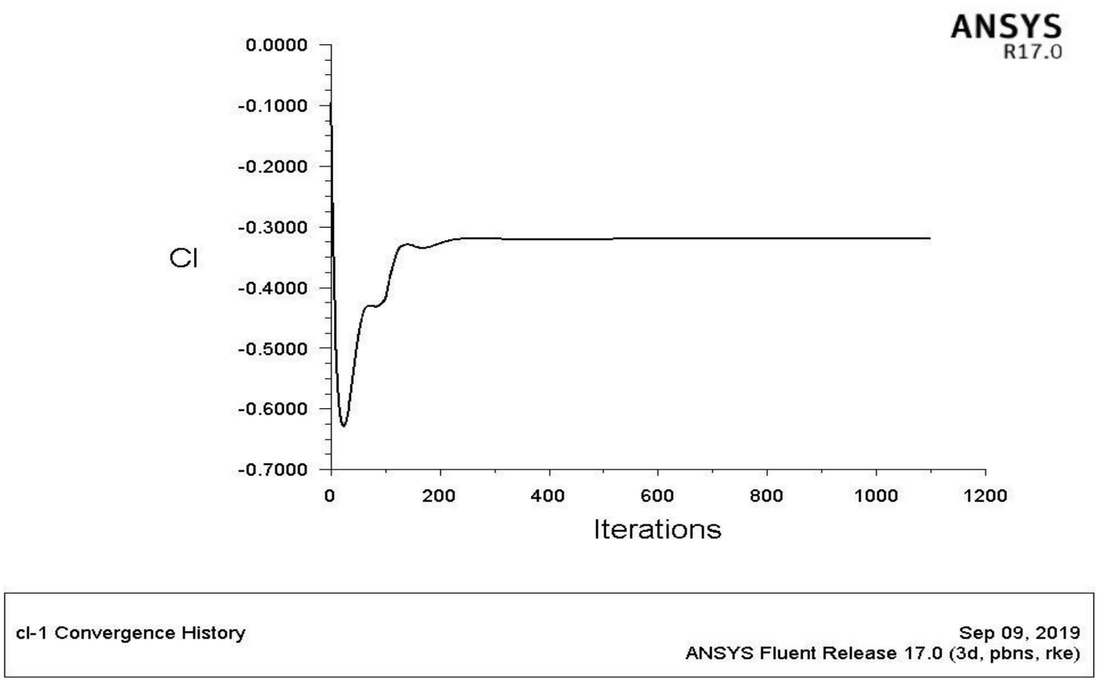

Figure 5. 61: Lift coefficient of model four at 80 kmph

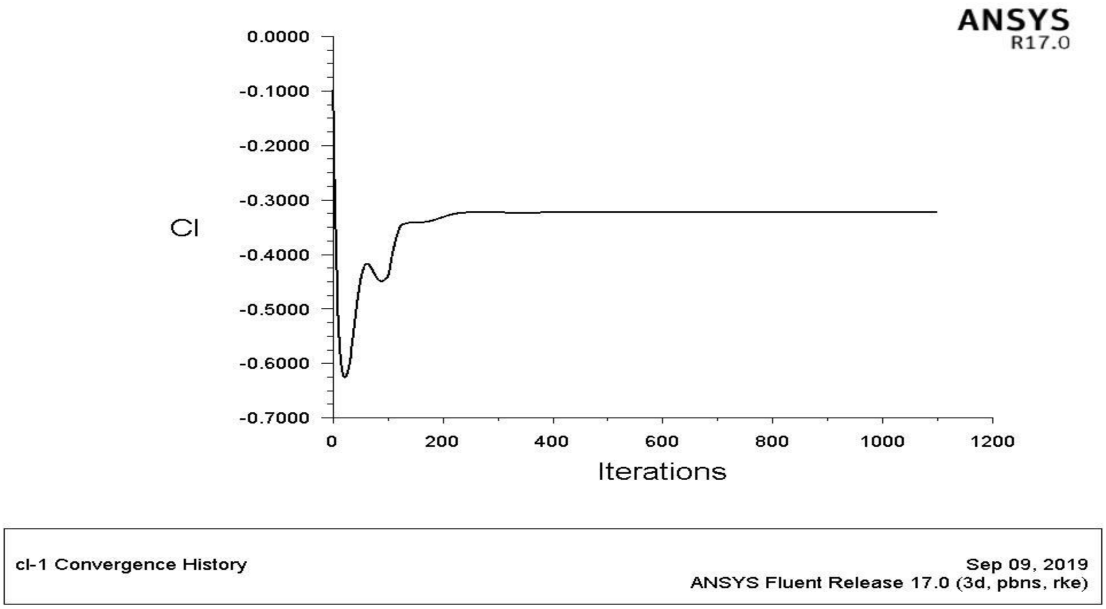

Figure 5. 62: Lift coefficient of model four at 100 kmph

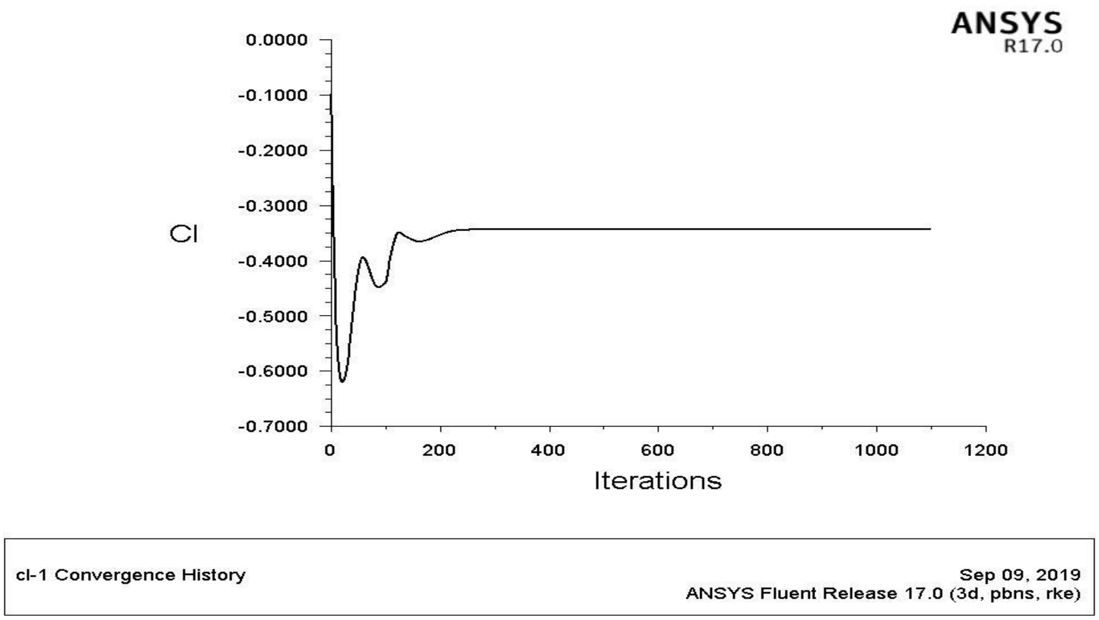

Figure 5. 63: Lift coefficient of model four at 120 kmph

All the drag coefficient graphs are shown in Figure 5.58, 5.59 and 5.60 and lift coefficient graphs Figure 5.61, 5.62 and 5.63 of model IV at speed of 80, 100 and 120 kmph are summarized in Table 5.4.

Table 5. 5: Summary of drag and lift coefficients of model IV at different speeds

Model	Speed (kmph)	C_d	C_l
Model Four	80	0.33014	-0.31882
	100	0.33239	-0.32173
	120	0.33547	-0.34138

Table 5.5 provided that the drag coefficient for model IV is 0.33267, there weren't too many changes in comparison to the third model, since the previous achieved a 0.34184 drag coefficient. But there is a great reduction in lift coefficient for model IV (-0.32731) to lift coefficient of model III (-0.15724), i.e. about 52% deviation in lift coefficients.

The drag coefficient has reduced from 0.34184 (the averaged drag coefficient at 80, 100, and 120 kmph speeds) for model III to 0.33267 (the averaged drag coefficient at 80, 100, and 120 kmph speeds) for model IV, thus the average reduction in C_d is 2.68%. This drag coefficient deviation of model IV is due to the rear spoiler because model IV doesn't have any modification on model III except the added device attached at the rear roof end of model III. Also, this model has a higher deviation of drag coefficient than other modified models when compared with the baseline model i.e. 54.35%. Figure 5.58-5.63, shows how the drag and lift coefficients converge with each iteration. Both the drag and lift coefficients of model IV converge early before 300th iteration. There is a large reduction in lift coefficient from model III as well as from other models this leads the bus to be more stable at higher speed. This increases the tires' capability to produce cornering force, improves braking performance and gives better traction.

Any flow disturbance has a reason. Changes in pressure distribution on the car body surface, as well as the formation of pressure gradients, affect the character and behavior of the boundary layer. The pressure distributions were visualized on the surface of the vehicle. Based on the pressure contours, the value of the pressure drag and aerodynamic downforce can be determined.

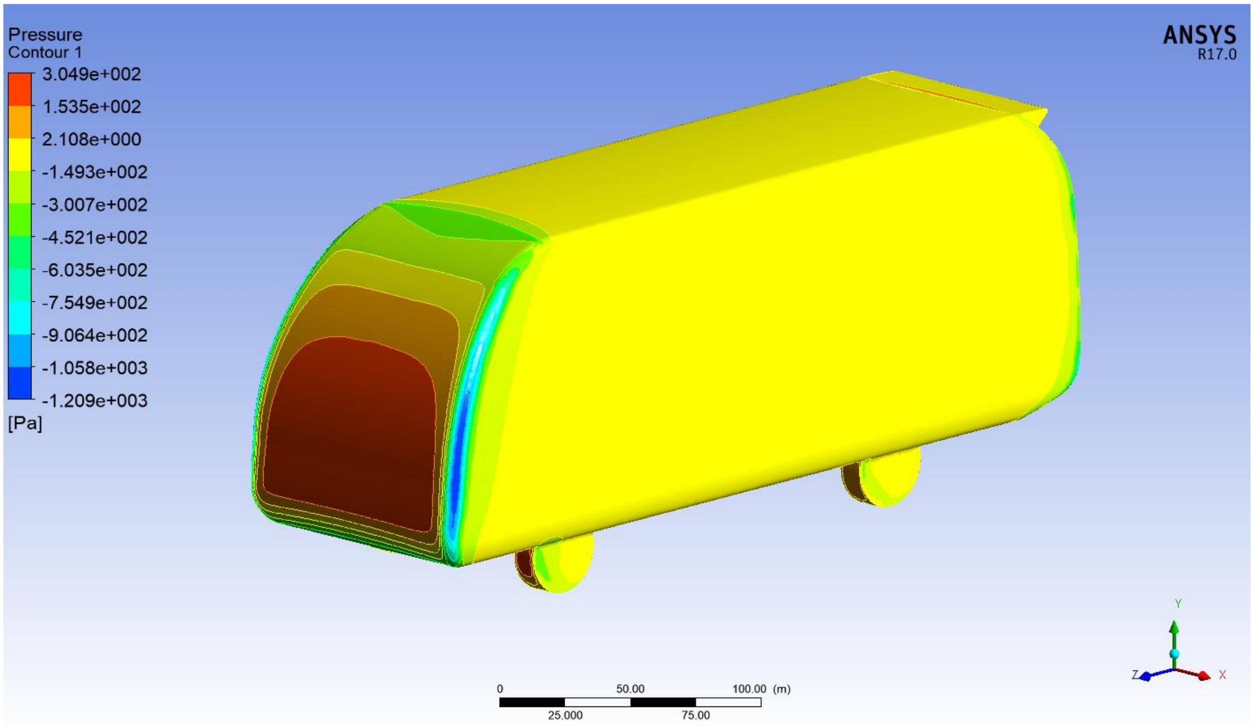

Figure 5. 64: Pressure contour of model four at 80 kmph

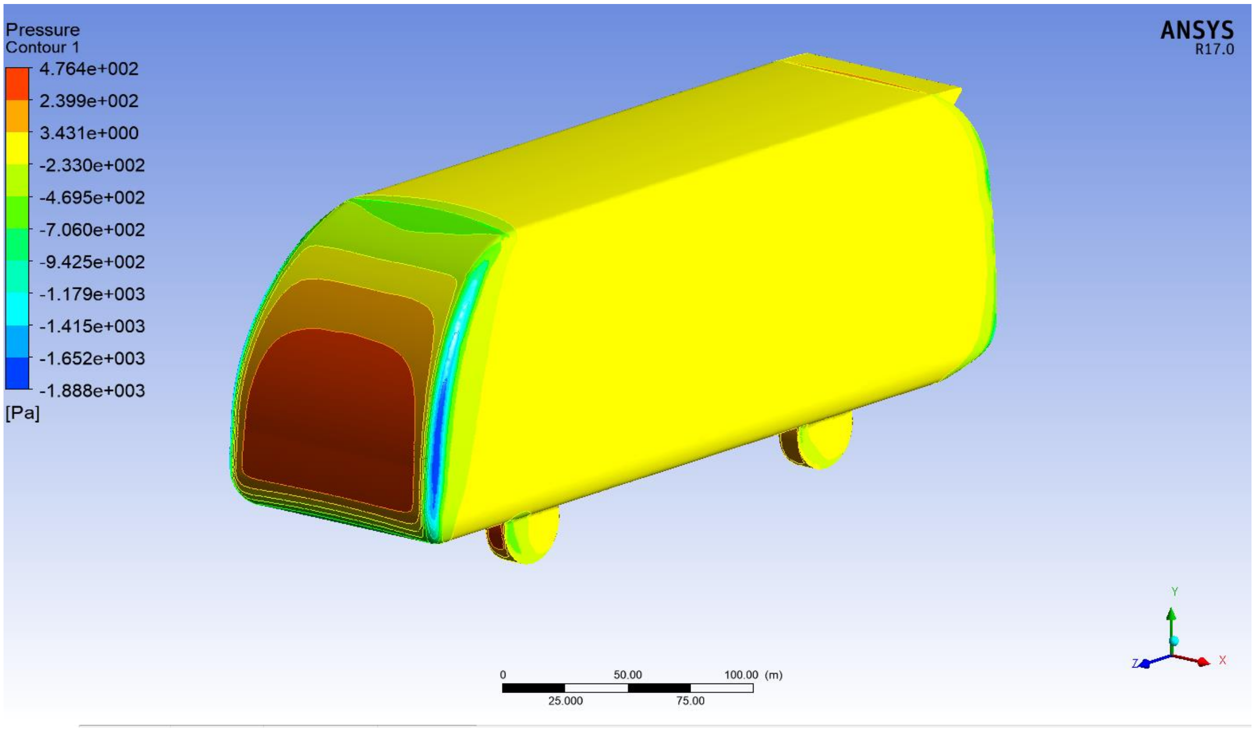

Figure 5. 65: Pressure contour of model four at 100 kmph

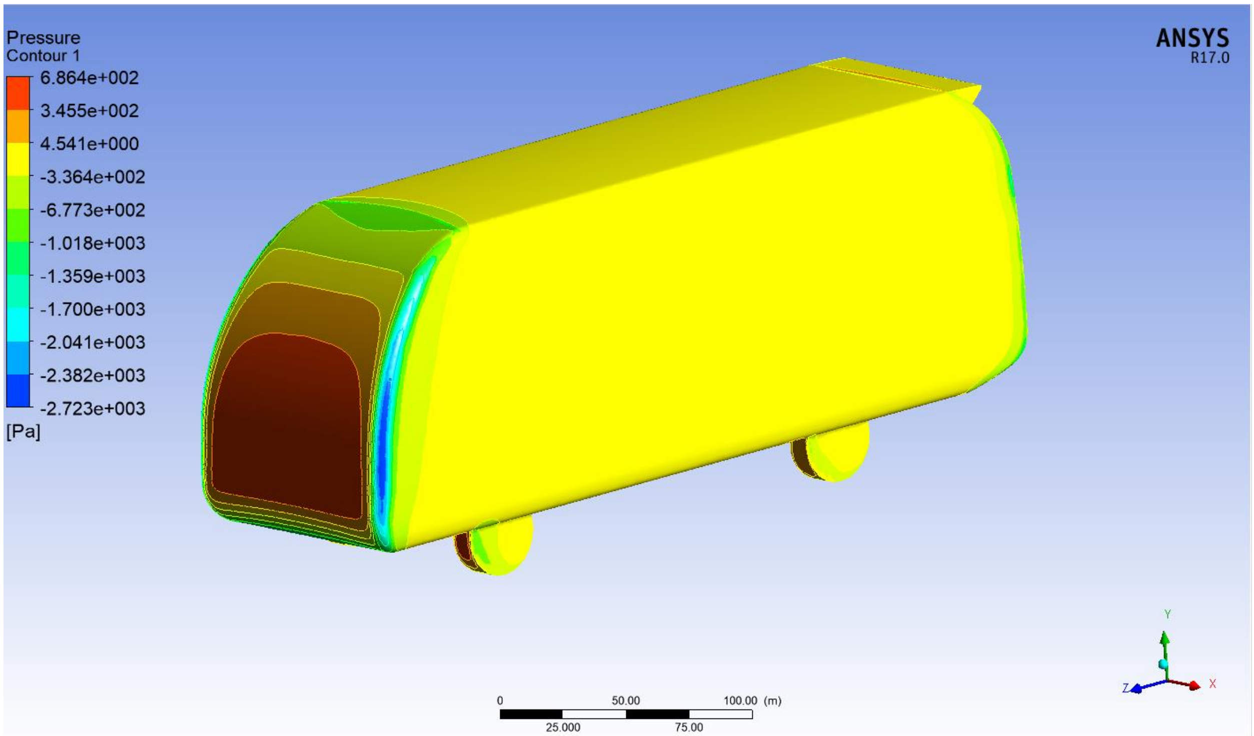

Figure 5. 66: Pressure contour of model four at 120 kmph

As it is well-known, the pressure (form) drag represents the major part of the total drag on the bus in comparison to the friction drag, the pressure distributions on the frontal and rear surfaces are considered. The pressure drag depends on the difference between the pressure distributions on the frontal and rear surfaces of the bus. For all models of pressure contour graphs, the pressure is really high on the bus frontal surface due to flow stagnation. The pressure is very low on the rear surface due to wake formation behind the bus.

Red color represents high-velocity areas of the contour as shown in Figures 5.64, 5.65 and 5.66. These high velocities are surrounded by slowly decreasing velocities which are represented by orange through yellow-colored sections in the contour. This was continued until, farther away from the vehicle, then the velocity evened out at the magnitude of the input velocity. An increase in the velocity from the input velocity to the maximum velocity causes the flow to separate and makes the low-velocity air to swirl at the back of the model.

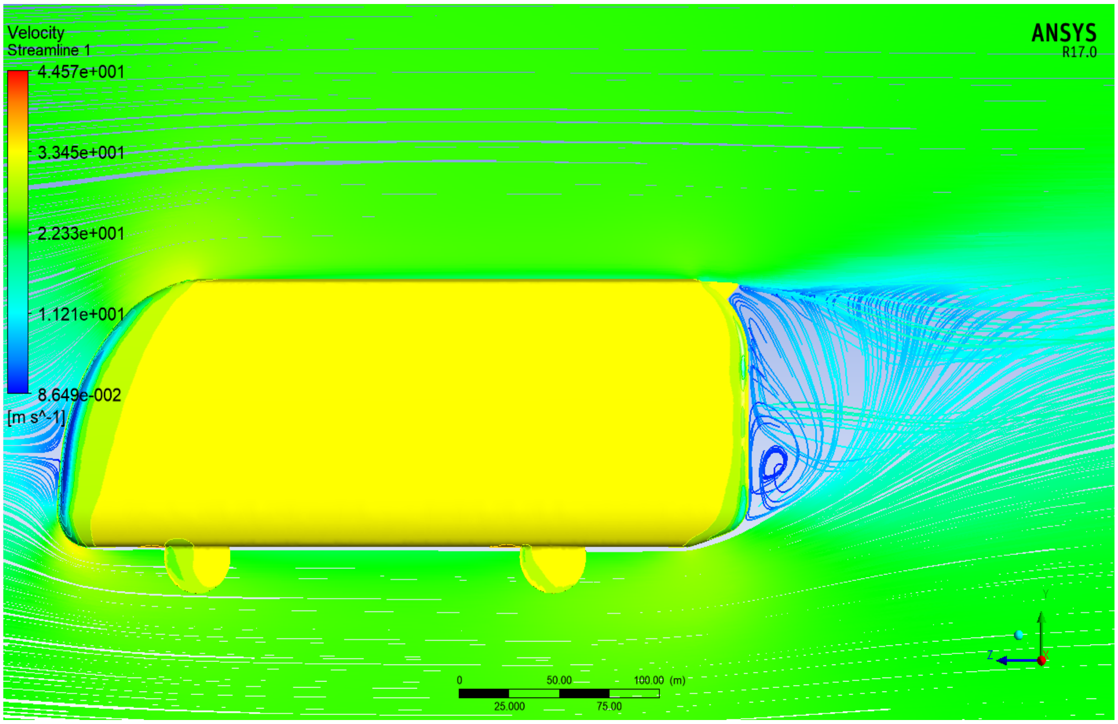

Figure 5. 67: Velocity contour of model four at 80 kmph

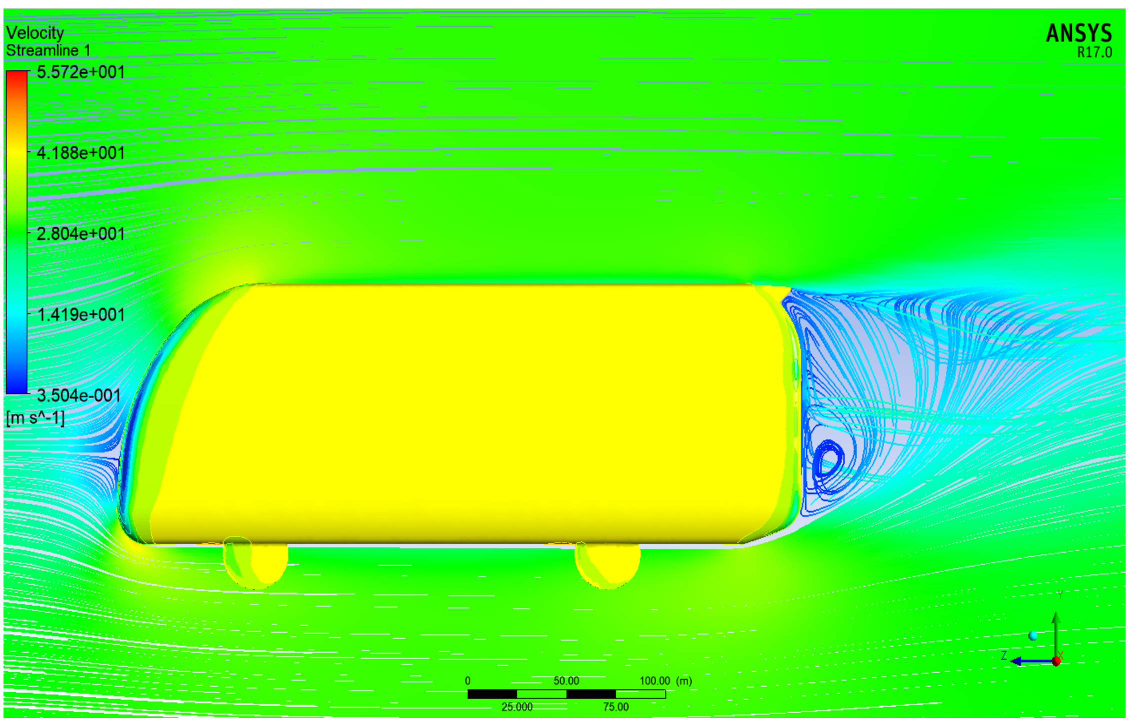

Figure 5. 68: Velocity contour of model four at 100 kmph

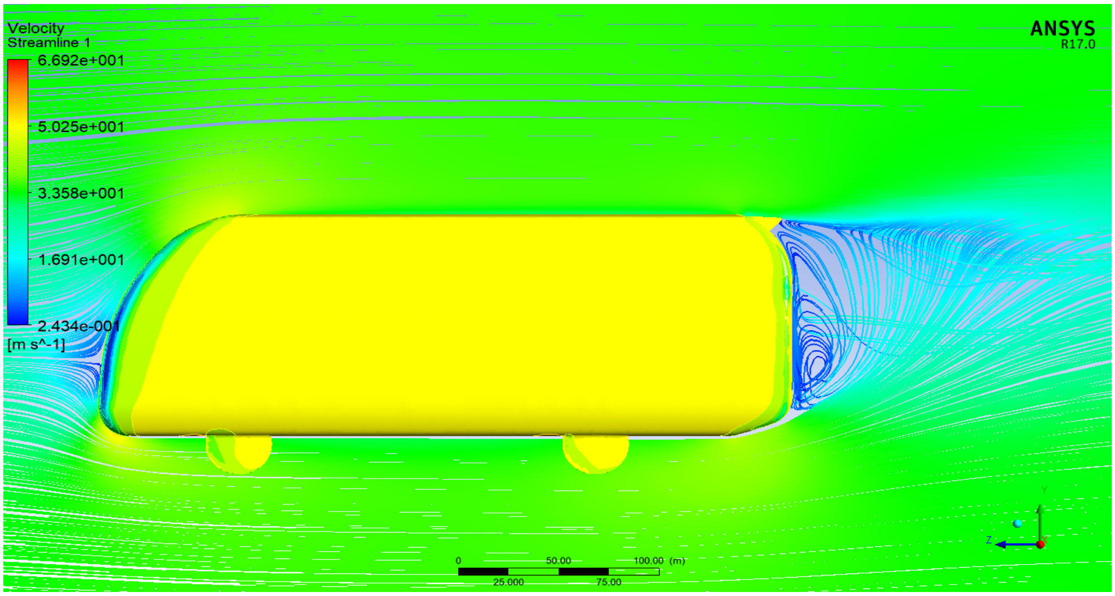

Figure 5. 69: Velocity contour of model four at 120 kmph

This model is the last model in the study. This model is the same as that of model III the only difference is the rear spoiler added on model III. Due to the presence of a rear spoiler in the rear upper part of the bus, the flow pattern behind the bus has slightly improved than model III. Consequently, which minimize the low-velocity area in the wake region and delay the turbulence zone away from the bus model. In all models of the bus velocity streamline contour shows that the wake region gets stronger and wider as the speed increases.

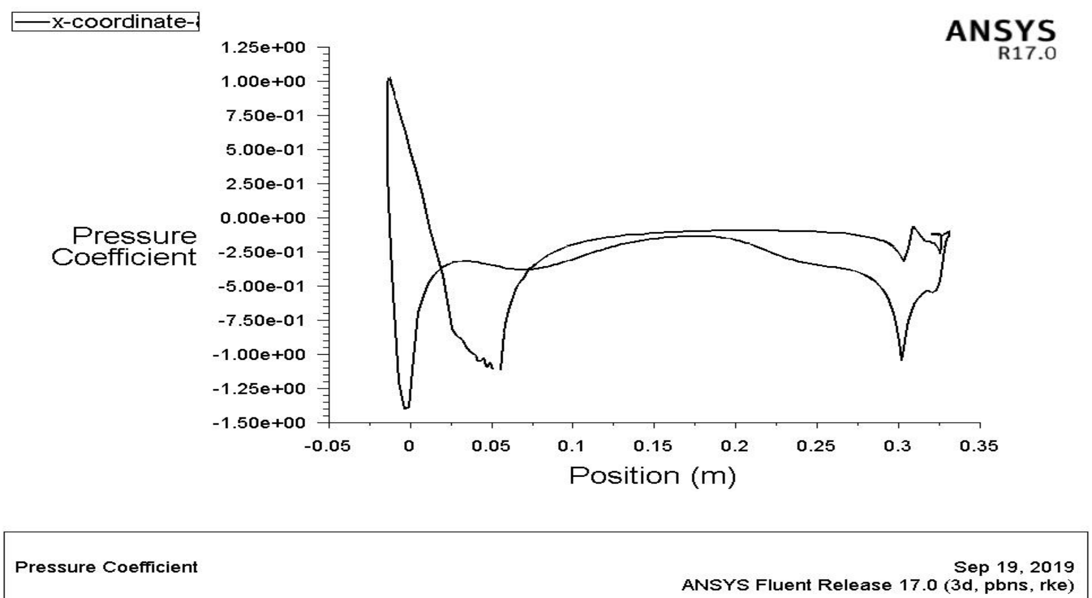

Figure 5. 70: Surface pressure distribution along the symmetry plane for model IV

The surface pressure distribution changes on the surface of model IV changes between maximum and minimum values. The pressure reduction on the spoiler is less than all other models. In this model, the amount of downward force is higher than all other models. The change in the surface pressure on the body of model four can be seen in Figure 5.70.

The low-pressure region behind the bus was seen spread across a wider area in the baseline design. The vortices formed behind the bus were also spread across the wide region. With the new designs of the bus, the flow is attached leading to suppressed vortices formation at the rear and these vortices were seen moving towards the ground. This change in the aerodynamic characteristics is due to the effect of the cornered radii in the front and rear of the roof, inclined and rounded windscreen and finally using rear spoiler.

5.2 Comparison Between Models

In order to choose the best aerodynamic model of an Isuzu Midi Bus with lowest drag and lift coefficients the comparison between models are necessary. Figure 5.71 and 5.72 shows the difference in drag and lift coefficient at speed of 80, 100 and 120 kmph between baseline model and all four models.

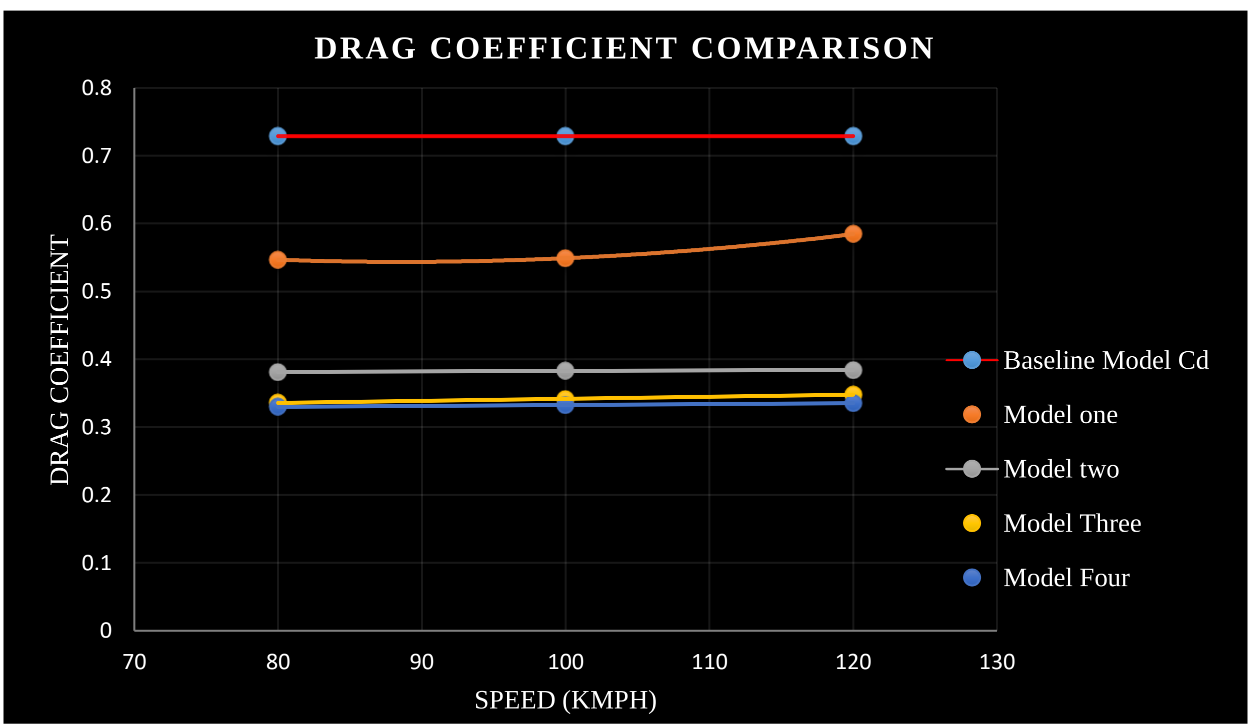

Figure 5. 71: Drag coefficient comparison of all models at different speed

The drag coefficient of all models increases as their speed increases (Figure 5.71). However, the slope is different for each model. Both at low and high speeds model IV has the lowest drag coefficient and the baseline model has the highest drag coefficient. Due to the exterior body modifications on the baseline model, the coefficient of drag reduced by model I, model II, models III and IV were approximately 23.15%, 47.46%, 53.09%, and 54.35%, respectively. The drag coefficient of model IV is lower than model III with average reduction in C_d of 2.68% resulting from the rear spoiler. Due to the reduced drag coefficient at both lower and higher speeds model IV saves more fuel and has less environmental effect because of its reduced fuel consumption and reduced emission.

Figure 5. 72: Lift coefficient comparison of all models at different speed

In order to improve the stability of an Isuzu midi bus at higher speeds the downward force should be high which is the result of reduced lift coefficient. From the figure 5.72, model IV has the least lift coefficient which makes it the most stable of all model at high speeds. Least stable is model III with the highest lift coefficient. The lift coefficient of all models decreases with increasing speed. Model IV achieved lowest lift coefficients, which increases the tires' capability to produce cornering force, improves braking performance and gives better traction.

The comparison between drag and lift coefficients of the baseline model with other four models at speeds of 80, 100, 120 kmph were summarized in Table 5.6. Also summarizes the drag and lift coefficients of four with the percentage difference from the baseline model.

Table 5. 6: Comparative coefficients of drag and lift for all models

Models	Speed (kmph)	Drag coefficient (C_d)	Average C_d Value	Percent of C_d reduction from baseline model (%)	Lift coefficient (C_l)	Avarage C_l Value
Baseline Model	80	0.72872	0.72881	-	-0.29553	-0.30059
	100	0.72877		-	-0.30106	
	120	0.72895		-	-0.30518	
Model I	80	0.54672	0.56010	25.01	-0.26465	-0.26759
	100	0.54906		24.66	-0.26496	
	120	0.58452		19.81	-0.27317	
Model II	80	0.38114	0.38293	47.69	-0.17429	-0.18363
	100	0.38354		47.37	-0.18612	
	120	0.38412		47.31	-0.19048	
Model III	80	0.33598	0.34184	54.01	-0.15144	-0.15724
	100	0.34142		53.15	-0.15861	
	120	0.34813		52.24	-0.16168	
Model IV	80	0.33014	0.33266	54.69	-0.31882	-0.32731
	100	0.33239		54.39	-0.32173	
	120	0.33547		53.98	-0.34138	

5.3 Calculation of Fuel Consumption

According to (Siddhesh, 2017) the fuel saving of the modified models relative to a baseline model can be calculated. Percentage fuel reduction is sixty percent of total drag reduction. The calculated values were given in Table 5.7.

Table 5. 7: Fuel Consumption Reduction

Models	Speed (kmph)	Percent of C_d reduction from baseline model (%)	Percent of fuel saving (%)
Baseline Model	80	-	-
	100	-	-
	120	-	-
Model I	80	25.01	15.01
	100	24.66	14.79
	120	19.81	11.88
Model II	80	47.69	28.61
	100	47.37	28.42
	120	47.31	28.38
Model III	80	54.01	32.41
	100	53.15	31.89
	120	52.24	31.34
Model IV	80	54.69	32.81
	100	54.39	32.63
	120	53.98	32.39

Table 5.7 shows a maximum of 32.81% fuel can be saved in model IV from a baseline model at 80 kmph and 32.61% of fuel can be saved in model IV at three average speeds from a baseline model. The other high reduction was from model III with 32.41%, 31.89% and 31.34% at speed of

80, 100 and 120 kmph, respectively. Model II reduces the amount of fuel consumption with 28.61%, 28.42% and 28.38% relative to a baseline model at speeds of 80, 100 and 120 kmph, respectively. However, model I has the least fuel reduction with 15.01%, 14.79% and 11.88% of fuel when compared to baseline model at speed of 80, 100 and 120 kmph, respectively.

5.4 Calculation of Reduction on Fuel Exhaust Emission

According to (Siddhesh, 2017) the fuel consumption by ground vehicles accounts for over 30% of CO_2 and other greenhouse gas emissions. From this the percent reduction of modified bus model relative to a baseline model was calculated to be 30% of 32.81 (percent of fuel saving) which is 9.8% of emissions reduced in model IV at 80 kmph, and average emission percent reduction was 30% of 32.61 which is 9.7% was reduced, in model three we can save 9.5% and model two 8.5% greenhouse gas was reduced. This reduction in exhaust emission has a significant effect in the environment.

5.5 Results and Discussions of Experimental Validation

The results of the CFD analysis must verified on vehicle aerodynamics studies. Some authors compare results with literature data. In this study the computational results verificated by wind tunnel test. The determined C_d values for a baseline model both experimentally and numerically are shown in Table 5.8.

Table 5. 8: C_d difference (%) between experimental and CFD anlysis

Speed (m/s)	C_d (Wind Tunnel Test)	C_d (CFD Simulation)	C_d Difference (%)
12	0.77795	0.71416	9.2
17	0.79280	0.71828	9.4
22	0.79904	0.72872	8.8
27.8	0.83024	0.72895	12.2

The drag coefficient of the baseline model was determined by both experimentally and numerically. However, there were a difference between the experimental result and CFD result.

This difference is acceptable. It can be results from the uncertainty of the wind tunnel, calibration error rate or vibration in high speeds of wind tunnel. The comparison can be seen in Figure 5.73.

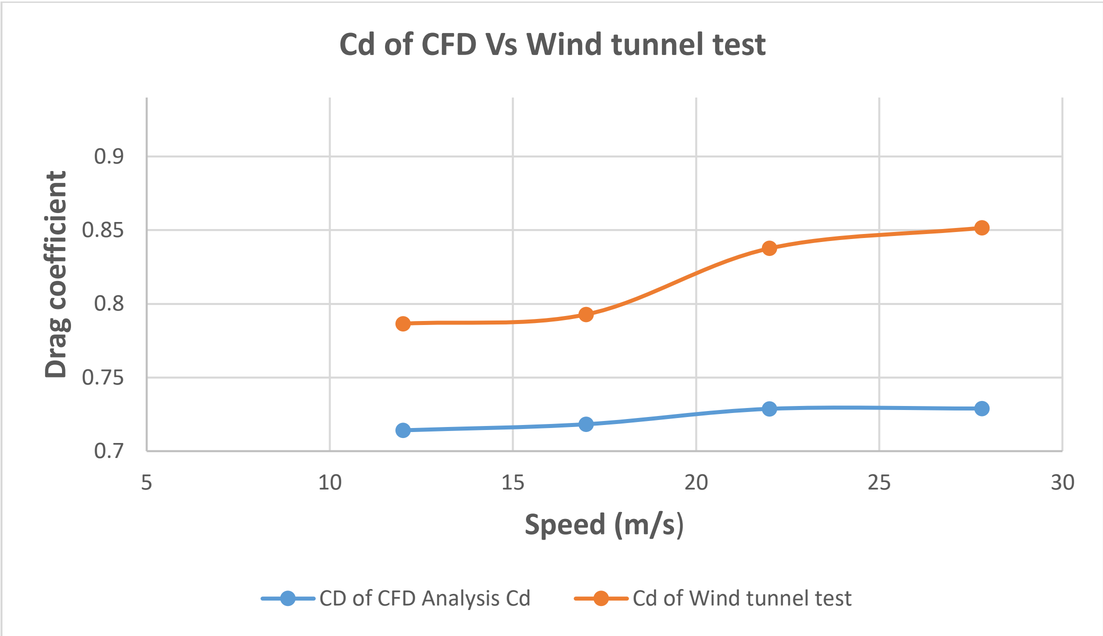

Figure 5. 73: Comparison of C_d between experimental and CFD anlysis.

5.6 Grid Independence Test

In section 3.8 the effect of the selected mesh size for the simulation were studied by varying the size of mesh. The here under graphs shows that both drag and lift coefficients are not dependent up on the selected mesh size.

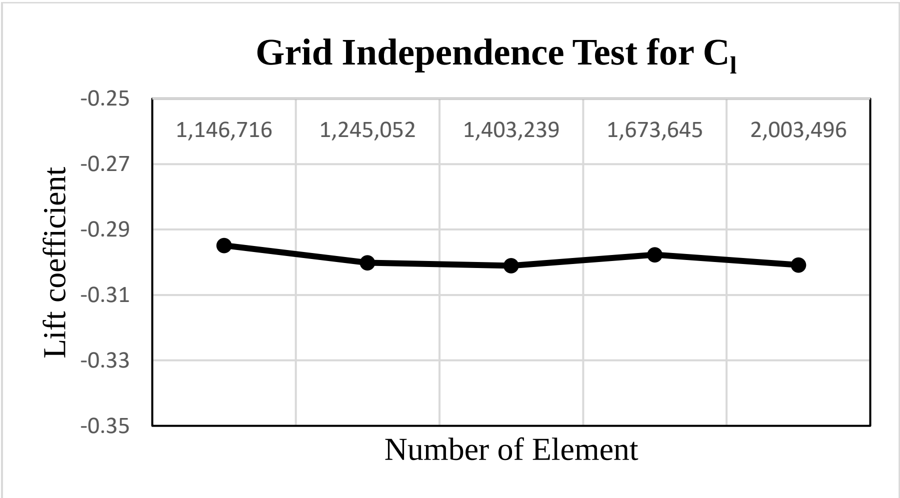

Figure 5. 74: Grid Independence test result for C_l

The drag and lift coefficients have little variation with variation of the number of elements. Hence the selected mesh size (10mm) with number of element 1,403,239 is accurate enough to capture the flow phenomena.

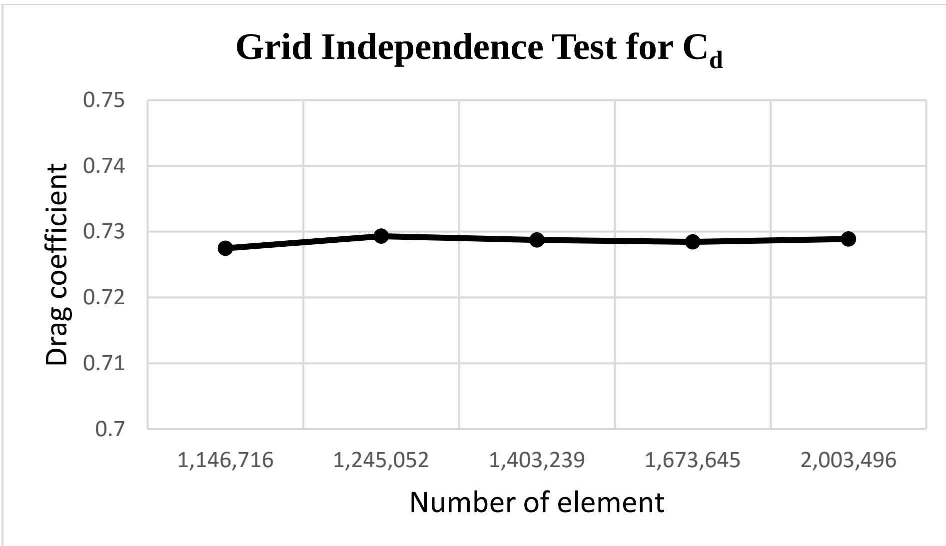

Figure 5. 75: Grid Independence test result for C_d

6. CONCLUSIONS AND RECOMMENDATIONS

Two approaches were used in this study for the investigation of external aerodynamics of four different Isuzu midi bus (Model I, II, III and IV) models. Combining wind tunnel experiment and CFD computation has shown how integration of both methods can lead to a better aerodynamic design.

6.1 Conclusions

After the analysis of all models, the modified models and a model with rear spoiler reduced the amount of swirling air in the back of the bus and hence reduced the amount of drag coefficient compared to baseline model. It was found that the large circulation region was formed in the back of an Isuzu midi bus baseline model and it created large pressure difference between the front and the rear of the bus, causing high drag in order to improve the aerodynamic performance of the existing bus four modifications of exterior body were prepared. The last prepared model employed rear spoiler, which was meant to push the flow separation a bit rearward and reduce the amount of drag by minimizing the wake region, and by throwing the turbulent air behind the vehicle.

The main findings are

- ❖ The results show that there is a possibility of improving the aerodynamic performance of bus by modifications the exterior design of bus body and by using add on device which is spoiler. These modifications are helpful in reducing the coefficient of drag i.e. C_d which improved fuel consumption and reduced to exhaust emission.
- ❖ It was found that the least drag force was acting on model IV. Bus model II and III gave an intermediate result as expected. The average drag coefficient of the baseline model, model I, model II, model III and model IV were 0.72881, 0.56010, 0.38293, 0.34184 and 0.33267, respectively. Due to the exterior body modifications on the baseline model, the coefficient of drag reduced by model I, model II, models III and IV were approximately 23.15%, 47.46%, 53.09%, and 54.35%, respectively. Also, model IV achieved lowest lift coefficients, which increases the tires' capability to produce cornering force, improves braking performance and gives better traction.
- ❖ The maximum of 32.81% fuel can be saved in model IV from a baseline model at 80 kmph and 32.61% of fuel can be saved in model IV at three average speeds this results 9.7% of

emissions reduction in model IV. This reduction in exhaust emission has a significant effect in the environment.

- ❖ This work uniquely proves that possibility of refining the exteriors Isuzu Midi Bus for simultaneous improvement in aerodynamics and aesthetics (attractive design) from the point view of product design.

6.2 Recommendations

- ❖ Many local automotive industries and bus bodybuilding companies have to check the aerodynamics performance of their vehicles body shape and have to give more emphasis on the aerodynamics of vehicles as there is a significant saving of fuel by reducing drag as demonstrated in this study.
- ❖ To obtain more accurate results it's recommended that to use a powerful computer with high processing speed and capacity, which improves the meshing quality and reduces processing time.

6.3 Recommendations for Future Work

The following recommendations can be taken into consideration as future work.

- ❖ The turbulence model which is used in this study can be tested in the determination of aerodynamic characteristics of different vehicle body shape types such as trucks, buses, and trains running on Ethiopian roads.
- ❖ Experimental studies, using a wind tunnel, could be run on the baseline model found in this study to compare the values found from numerical analysis for validity.
- ❖ Using add-on devices and different modifications that reduce the aerodynamic drag present on the bus. Also, design and test active drag reduction device to reduce the drag force on the vehicle.

REFERENCES

Abdel Gawad and Abdel Aziz (2006), 'Aerodynamic and heat transfer characteristics around Vehicles with different front shapes in driving tunnels', *Proceedings of Eighth International Congress of Fluid Dynamics and Propulsion (ICFDP 8)*, Sinai, Egypt.

Abdulkareem Sh. Mahdi Al-Obaidi and Wesley Allen Otten (2018), 'Aerodynamic analysis of personal Vehicle side mirror', *Journal of Engineering Science and Technology*, School of Engineering, Taylor's University, 7th EURECA Special Issue 52 - 64.

Ahmed. H and Chacko (2012), '*Computational optimization of Vehicle Aerodynamics'*, Annals of Proceedings of the 23rd International DAAAM Symposium, Volume 23, No.1, ISSN 2304-1382.

Ahmed, G. Faltin, and G. Ramm (1984), '*Some salient features of the time-averaged ground vehicle wake'*, SAE, Technical Paper 840300.

A. Muthuvel, M.K. Murthi, Sachin. N. P, Vinay M. Koshy, S. Sakthi, and E. Selvakumar (2013), 'Aerodynamic Exterior Body Design of Bus', *International Journal of Scientific & Engineering Research (IJSER)*, Volume 4, Issue 7, ISSN 2229-5518.

A. Thacker et al. (2012), 'Effects of suppressing the 3D separation on the rear slant on the flow structures around an Ahmed body', *Journal of Wind Engineering and Industrial Aerodynamics*, ELSEVIER 107–108 (2012) 237–243.

Arun Raveendran et al. (2009), '*Exterior styling of an intercity transport bus for improved Aerodynamic performance*', SAS TECH, Volume 8 issue 2.

Barnard, R. H. (2009), '*Road Vehicle Aerodynamics Design*', Mech Aero, 3rd edition.

Batchelder, J.H. (2009), '*A CFD investigation of potential aerodynamic enhancements to a microcar class vehicle*', unpublished Master's thesis submitted to Rensselaer Polytechnic Institute, USA.

B.Saravanan (2016), 'Analysis on Bus Body Aerodynamics & Fuel Efficiency in City Buses', *International Journal of Engineering Science and Computing (IJESC)*, Volume 6 Issue No. 12.

Bellman, M., Agarwal, R., Naber, J., and Chusak, L. (2010), '*Reducing the energy consumption of ground vehicles by active flow control*', ASME 2010 4th International Conference on Energy Sustainability, pp 785793, American Society of Mechanical Engineers.

C. N. Patil, K.S. Shashishekar, A. K. Balasubramanian, and S. V. Subbaramaiah, (2012), 'Aerodynamic Study and Drag Coefficient Optimization of Passenger Vehicle', *International Journal of Engineering Research & Technology (IJERT)*, Vol. 1, Issue 7.

Che Zakem, R. (2008), '*Aerodynamics of aftermarket rear spoiler*', Unpublished Bachelor Thesis submitted to University of Malaysia Pahang.

Cheng and S Mansor (2017), '*Rear-roof spoiler effect on the aerodynamic drag performance of a simplified hatchback model*', Journal of Physics: Conference Series 012008, Fifteenth Asian Congress of Fluid Mechanics (15ACFM).

Cooper K R. (2006), 'Full-Scale Wind-tunnel tests of production and prototype', Second-Generation Aerodynamic Drag Reducing Devices for Tractor-Trailers', *SAE*, Paper No.2006-01-3456, USA.

Darshan M. Desai and Imran Molvi (2017), 'Effect of Various Aerodynamic Drag Reduction Methods on Vehicle- A Review', *International Journal of Advance Engineering and Research Development, Scientific Journal of Impact Factor (SJIF)*, Volume 4, Issue 6.

Donovan J Cogan (2016), '*The Aerodynamic design and development of an urban concept vehicle through CFD analysis'*, Cape Peninsula University of Technology.

D. Palande and Ashwini (2016), 'Aerodynamics Study of Automobile Car Ahmed Body using CFD Simulation to Predict the Drag Coefficient and Down Forces', *International Engineering Research Journal (IERJ)*, Special Issue Page 1140-1145, ISSN 2395-1621.

Eyad Amen Mohamed, Muhammad Naeem Radhwi and Ahmed Farouk Abdel Gawad, (2015), 'Computational investigation of aerodynamic characteristics and drag reduction of a bus model', *American Journal of Aerospace Engineering*, Volume 2: pp 64-73.

G. Ganesh (2015), ‘Analysis of Effects of Rear Spoiler in Automobile Using Ansys, *International Journal of Scientific and Engineering Research*, Volume 6, Issue 6, ISSN 2229-5518, PP: 762-766.

G. Siva and V. Loganathan (2016), ‘Design and Aerodynamic analysis of a car to improve performance’, *Middle-East Journal of Scientific Research (Recent Innovations in Engineering, Technology, Management and Applications)*, ISSN 1990-9233, PP 133-140.

Guo, L., Zhang, Y., and Shen, W. (2011), ‘Simulation analysis of Aerodynamics characteristics of different two-dimensional Automobile shapes’, *Journal of Computers*, 6(5), 999-1005. doi:10.4304/jcp.6.5.9991005.

Hardik Panchal, Krishna Kumar, and Raybahadursinh Chauhan (2016), ‘*A review on Aerodynamic study of Vehicle body using CFD*’, Conference Paper, ResearchGate, NCEVT.

Hu X. X., and Wong, T. T. (2011), ‘A numerical study on rear-spoiler of passenger vehicle’, World Academy of Science, Engineering and Technology, *International Journal of Mechanical and Mechatronics Engineering* Vol. 57, pp636-641.

Hucho W.H. (1998), *‘Aerodynamics of Road Vehicles’*, 4th Edition, Society of Automotive Engineers, Warrendale.

Hucho W. H. and Sovran G. (1993), *‘Aerodynamics of road vehicles’*, Annual Review of Fluid Mechanics, Vol. 25(1), pp 485-537.

H. Taherian and Aniket Bhave (2014), ‘*Aerodynamics of an intercity bus and its impact on CO_2 reductions*’, ResearchGate, UAB School of Engineering - ECTC Proceedings -Vol. 13, DOI: 10.13140/2.1.1252.7046.

Jeff Patten et al. (2012), ‘*Review of aerodynamic drag reduction devices for heavy trucks and buses*’, CSTT-HVC-TR-205, National Research Council of Canada, Centre for surface transportation technology, 2012.

Jiyuan Tu, Guan Heng Yeoh and Chaoqun Liu (2007), ‘*Computational fluid dynamics: A practical approach*’, Butterworth-Heinemann; 1st edition, Burlington.

Kapadia, S., Roy, S. (2003), 'Detached eddy simulation over a reference Ahmed car model', AIAA Paper 2003-0857.

Kim C., (2011) "A Streamlined design of a high-speed coach for fuel savings and reduction of carbon dioxide", *International Journal of Automotive Engineering,* Technical Paper 20114633.

Krishnani, P. N. (2009), '*CFD study of drag reduction of a generic sport utility vehicle'*, Unpublished master's thesis submitted to the Mechanical Engineering Department, California State University, Sacramento.

Maji, S. and Almadi, H. (2007), *'Development of Aerodynamics of a Super Mileage Vehicle'*, SAE Technical Paper 2007-26-060, 2007, DOI:10.4271.

Matt, Cable (2009), '*An Evaluation of Turbulence Models for the Numerical Study of Forced and Natural Convective Flow in Atria'*, Unpublished thesis submitted to Queen's University Kingston, Ontario, Canada p. 148.

Menter, F.R. (1994), 'Two-equation eddy-viscosity turbulence models for Engineering applications', *AIAA Journal*, 32(8):1598-1605.

Metz N. (2001), *'Contribution of passenger cars and trucks to* CO_2*,* CH_4*,* N_2O*, CFC, and HFC emissions'*, SAE Technical Paper 2001-01-3758.

Min-Ho Kim, Jong-YoungKuk and In-Bum Chyun (2002), '*A numerical simulation on the drag reduction of the large-sized bus using rear spoiler*', SAE Technical paper series 2002-01-3070.

Muhammad Ferdous Raiyan, Safayet Hossain, Mohammed Nasir Uddin Akanda and Nahed Hassan Jony (2014), 'A comparative flow analysis of NACA 6409 and NACA 4412 Aerofoil', *International Journal of research in Engineering and Technology*, ISSN: 2319-1163 | pISSN: 2321-7308, Volume: 03 Issue: 10.

Pankaj Mishra and K R Aharwal (2018), '*A review on a selection of turbulence model for CFD analysis of airflow within cold storage*', 2nd International Conference on Advances in Mechanical Engineering (ICAME), IOP Publishing.

P. Ramasekhar Reddy and R. Lokanadham (2017), 'CFD analysis on aerodynamic effects on a passenger car', *International Research Journal of Engineering and Technology (IRJET)*, Volume: 04 Issue: 09.

P. R. Sonawane, S.P. Sekhawat, and K.K. Rajput (2011), 'Aerodynamic Analysis of Car Body for Minimum Fuel Consumption', *Journal of information knowledge and research in Mechanical Engineering*, ISSN 0975-668X, Volume-01, Issue-02.

Pravin M. and M. Hiwase (2014), 'Aerodynamics basic concept and rear end application in small vehicles- A review', *International Journal of Engineering Research and Technology (IJERT)*, ISSN: 2278-0181, Vol. 3 Issue 7.

Qi-Liang Wang, Zheng Wu, and Xian-Liang Zhu (2017), '*Analysis of the aerodynamic performance of tesla models by CFD*', 3rd Annual international conference on electronics, Electrical Engineering, and information science, advances in Engineering research (AER), volume 131.

Ram Bansal and R. B. Sharma (2014), 'Drag reduction of a passenger car using add-on devices', Hindawi publishing corporation, *Journal of Aerodynamics*, Volume 2014, Article ID 678518.

R. H. Barnard (2001), *'Road Vehicle Aerodynamic Design*', Mech. Aero Publishing, second edition.

R. Manimaran (2015), 'Aerodynamic study of the Ahmed body in road-situations using computational fluid dynamics", Thermal and Automotive research group, VIT University, India.

R. Mc. Callen, K. Salari, J. Ortega, F. Browand, and M. Hammache (2004), *'Effort to reduce truck aerodynamic drag-joint experiments and computations lead to smart design'*, AIAA Fluid Dynamics Conference, June 28 – July 1.

Rehan Salahuddin Khan and Sudhakar Umale (2014), 'CFD aerodynamic analysis of Ahmed body', *International Journal of Engineering Trends and Technology (IJETT)* -Volume 18, Number 7, Sardar Patel College of Engineering, India.

S. Banga, Md. Zunaid, Naushad Ahmad Ansari, S. Sharma and Rohit Singh Dungriyal (2015), "CFD simulation of flow around the external vehicle: Ahmed body', *IOSR Journal of Mechanical and Civil Engineering (IOSR-JMCE)*, e-ISSN: 2278-1684, Volume 12, Issue 4, pp 87-94.

Siddhesh Kanekar, Prashant Thakre and E Rajkumar (2017), '*Aerodynamic study of state transport bus using computational fluid dynamics*', School of Mechanical Engineering, VIT University, IOP Conf. Series: Materials Science and Engineering 263 (2017) 062052.

Shih T.H., Liou W.W., Shabbir A., Yang Z., and Zhu J. (1995), 'A new-eddy viscosity model for high Reynolds number turbulent flows - model development and validation', Computers Fluids, 24(3):227-238.

Snegirjov, A. Ju. (2009), High-performance computing in technical physics. Numerical simulation of turbulent flows: a training manual. Publishing House of St. Petersburg State Polytechnical University, St. Petersburg, Russia, pp: 143.

S.M. Rakibul Hassan et al. (2014), Numerical study on aerodynamic drag reduction of racing cars", 10th International Conference on Mechanical Engineering, ICME 2013, Bangladesh University of Engineering and Technology, Procedia Engineering 90 (2014) 308– 313.

S. Watkins G. Oswald (1999), 'Wind Engineering Introduction to Aerodynamic' pp 541-554.

Thabet, Senan, and Thabit, Thabit H. (2018), 'Computational Fluid Dynamics, Science of the future', *International Journal of Research and Engineering*, Vol.5, No. 6, pp. 430-433.

Vipul Kshirsagar and Jayashri V. Chopade (2018), 'Aerodynamics of high-performance vehicles', *International Research Journal of Engineering and Technology (IRJET)*, Volume: 05 Issue: 03, e-ISSN: 2395-0056, p-ISSN: 2395-0072.

Wassen E. and Thiele, F. (2010), *'Simulation of active separation control on a generic vehicle'*, In at 5th AIAA flow control conference, Chicago, USA.

W. Seibert, M. Lanfrit, B. Hupertz, and L. Kruger (2002), 'A best practice for high-resolution aerodynamics simulation around a production car shape', Fourth MIRA International Vehicle aerodynamics conference in Warwick, UK.

Wilcox D. C. (2003), Turbulence modeling for CFD', La Canada, California: DCW Industries.

Wilcox, D. C. (2008), 'Formulation of the k-omega turbulence model revisited', American Institute of Aeronautics and Astronautics 11, 2823.

Y. Cengel and J. M. Cimbala (2017), *'Fluid Mechanics-Fundamentals and Applications'*, McGraw-Hill Education, Nevada, Reno.

Yakhot, V. and Orszag, S. A. (1986), *'Renormalization group analysis of turbulence: Basic theory'*, Journal of scientific computing, 1(1):1-51.

Yuvraj P. Pawar and Swapnil D. Chaware (2017), Improvement in fuel efficiency of bus using a roof fairing', *Journal of Emerging Technologies and Innovative Research (JETIR)*, ISSN-2349-5162, Volume 4, Issue 11.

APPENDIX

Appendix A: SolidWorks Modelling

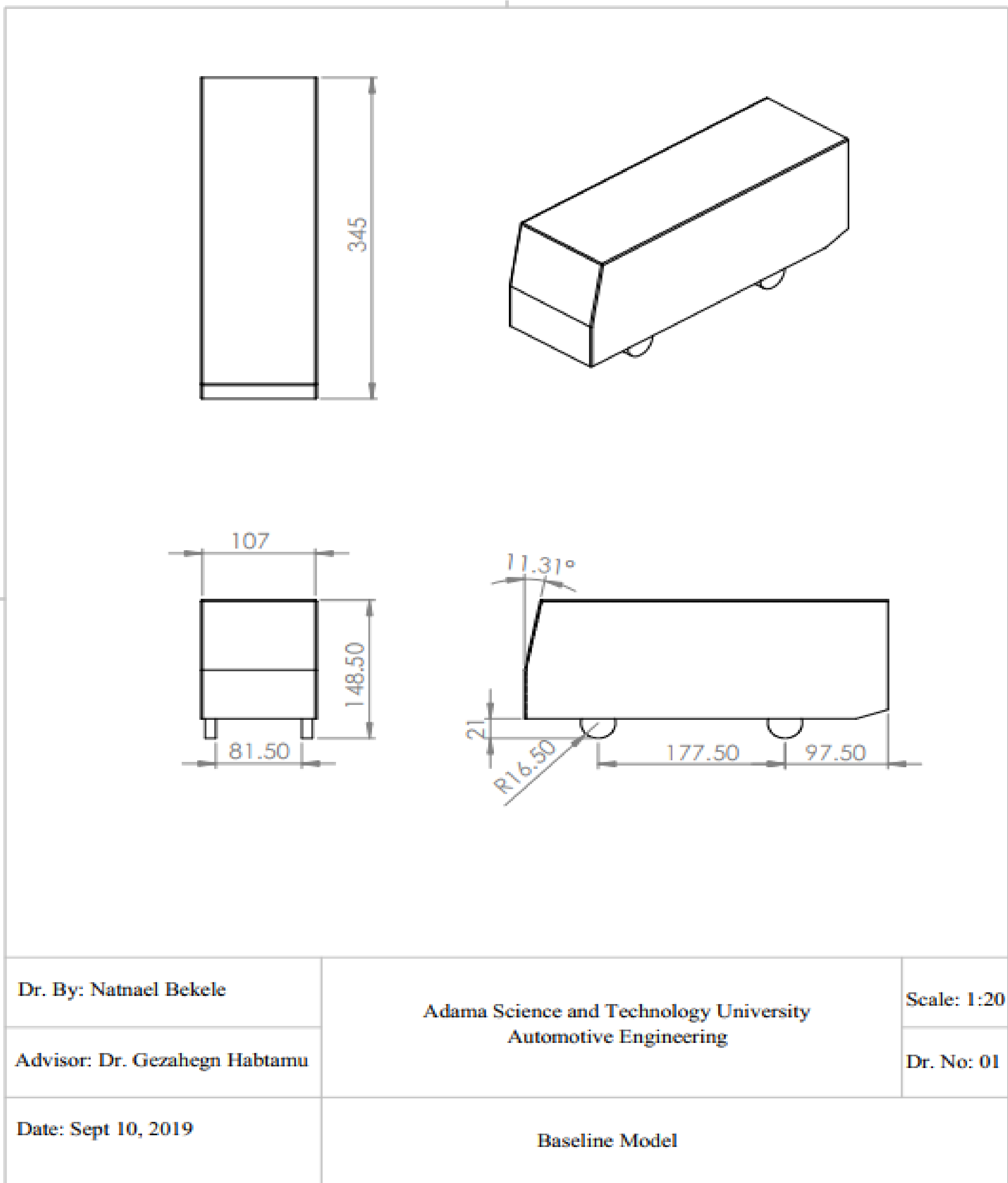

Figure A- 1: Baseline Model Multiview

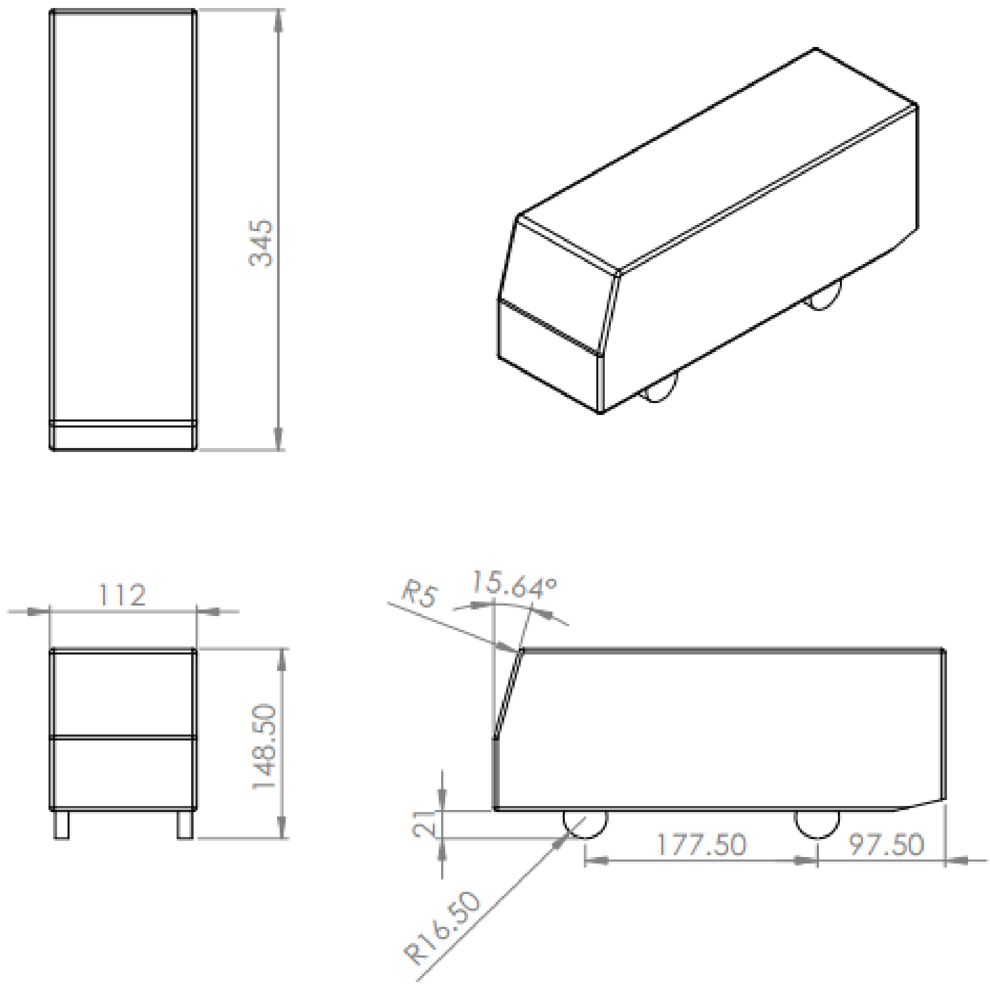

Dr. By: Natnael Bekele	Adama Science and Technology University Automotive Engineering	Scale: 1:20
Advisor: Dr. Gezahegn Habtamu		Dr. NO: 02
Date: Sept 10, 2019	Model One	

Figure A- 2: Model I Multiview

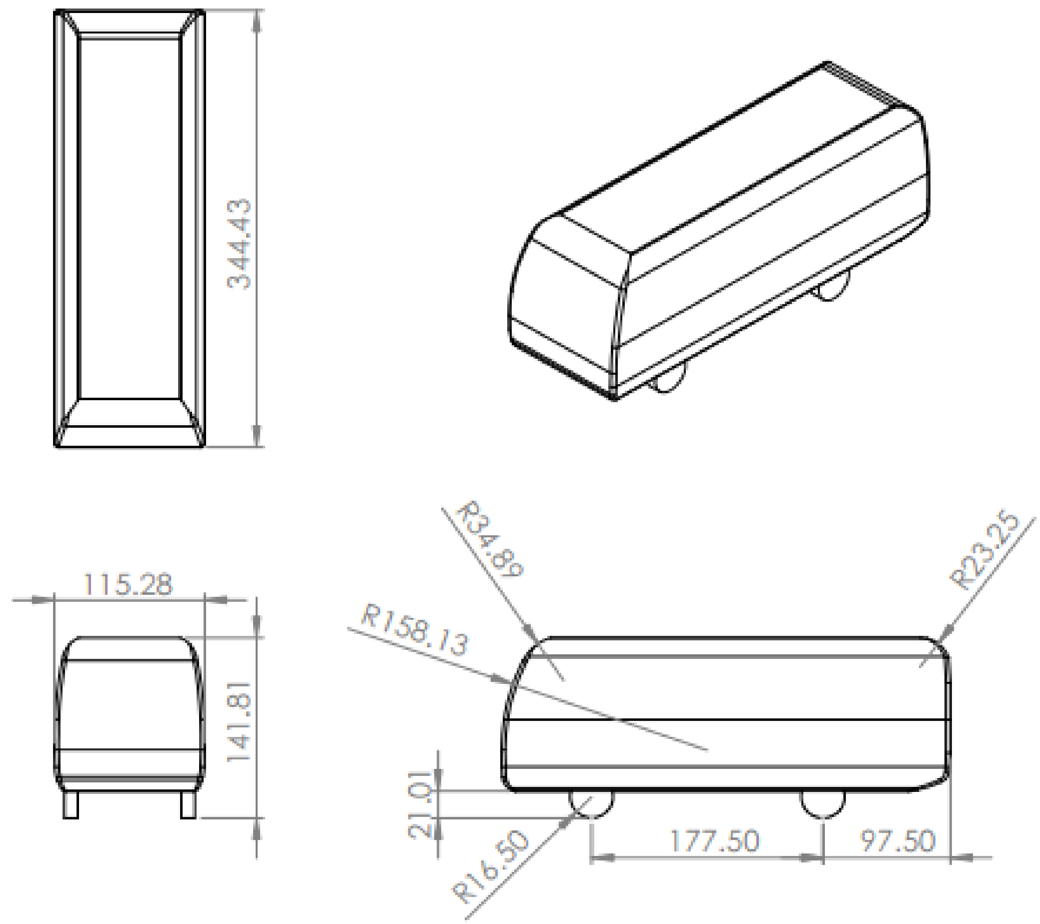

Dr. By: Natnael Bekele	Adama Science and Technology University Automotive Engineering	Scale: 1:20
Advisor: Dr. Gezahegn Habtamu		Dr. No: 03
Date: Sept 10, 2019	Model Two	

Figure A- 3: Model II Multiview

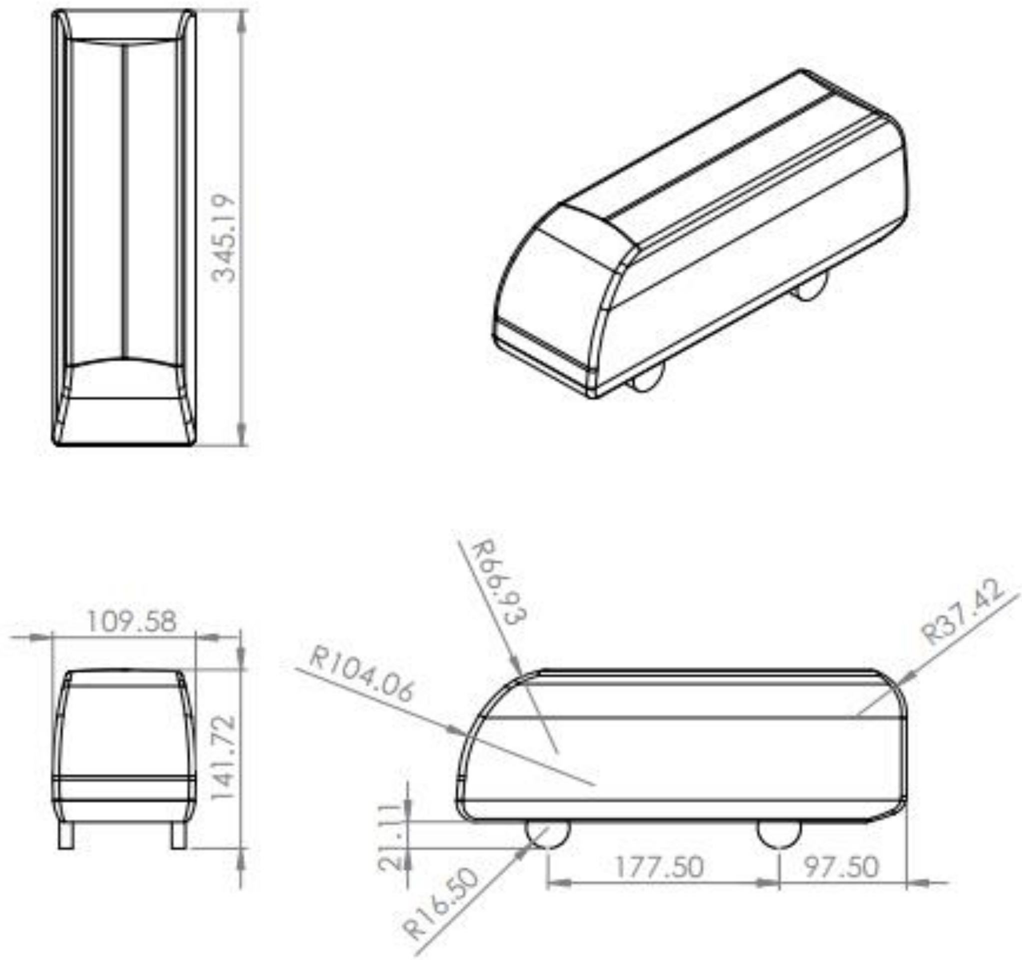

Dr. By: Natnael Bekele	Adama Science and Technology University Automotive Engineering	Scale: 1:20
Advisor: Dr. Gezahegn Habtamu		Dr. No: 04
Date: Sept 10, 2019	Model Three	

Figure A- 4: Model III Multiview

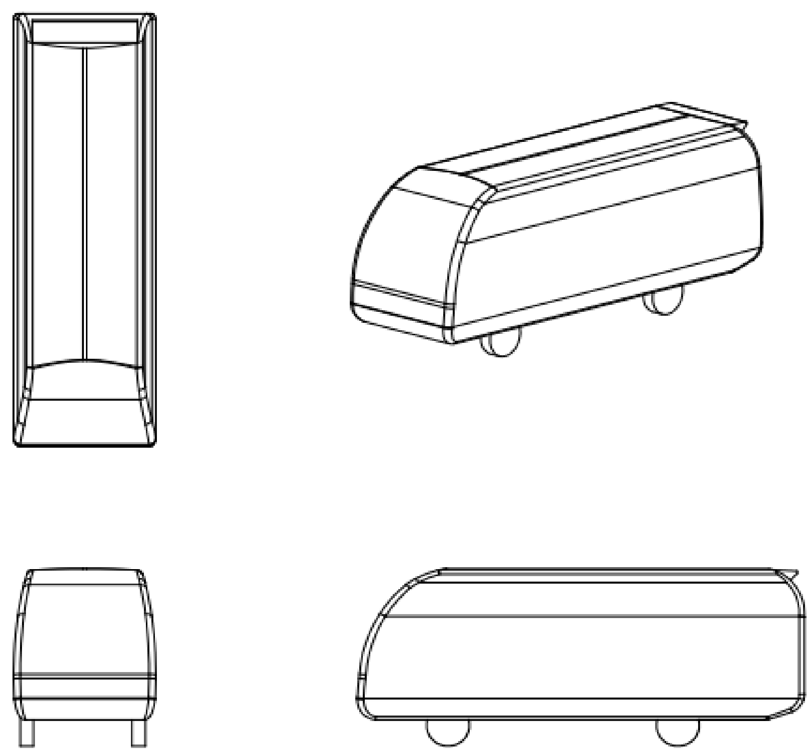

Dr. By: Natnael Bekele	Adama Science and Technology University Automotive Engineering	Scale: 1:20
Advisor: Dr. Gezahegn Habtamu		Dr. No: 05
Date: Sept 10, 2019	Model Four	

Figure A- 5: Model IV Multiview

Appendix B: Models Inside the Enclosure and After Meshing

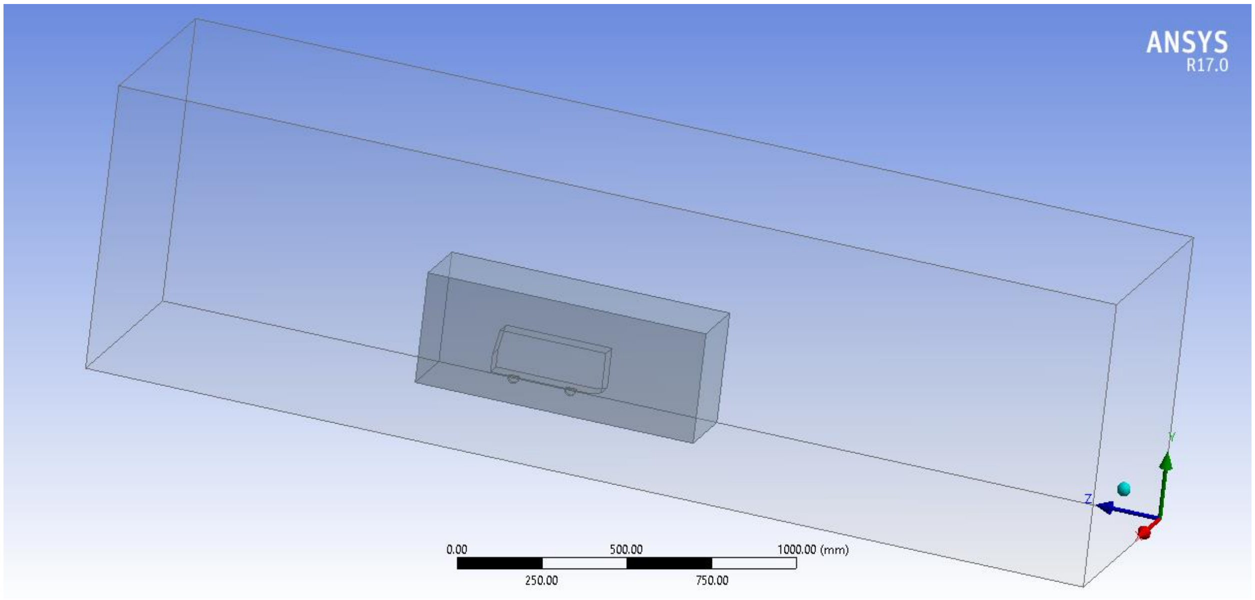

Figure B- 1: Baseline model inside the enclosure box

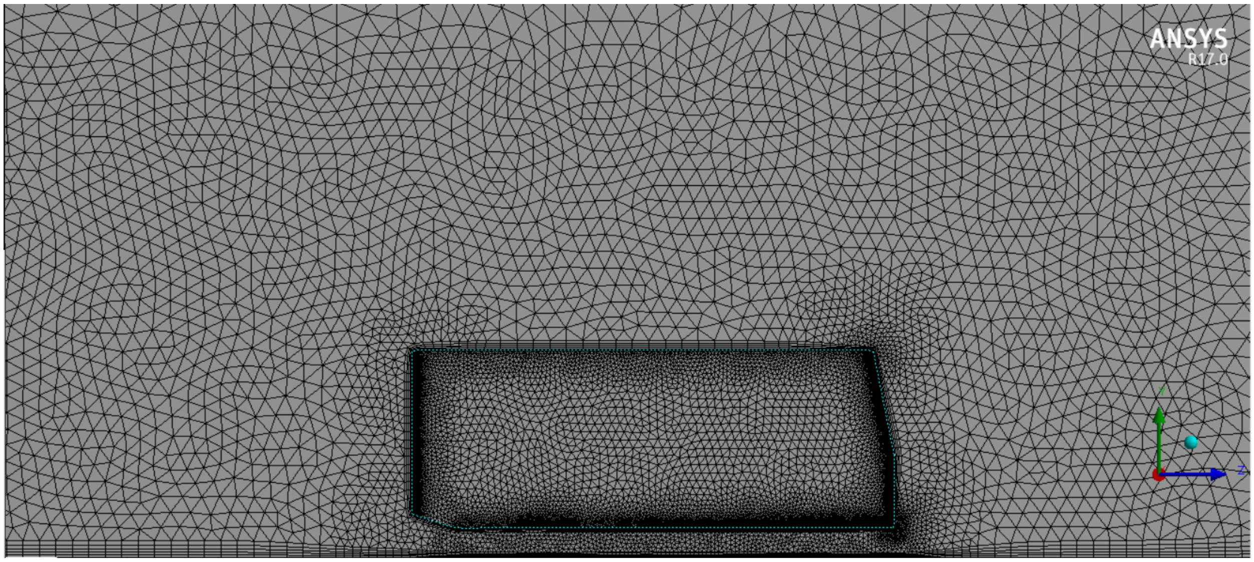

Figure B- 2: Baseline model after meshing

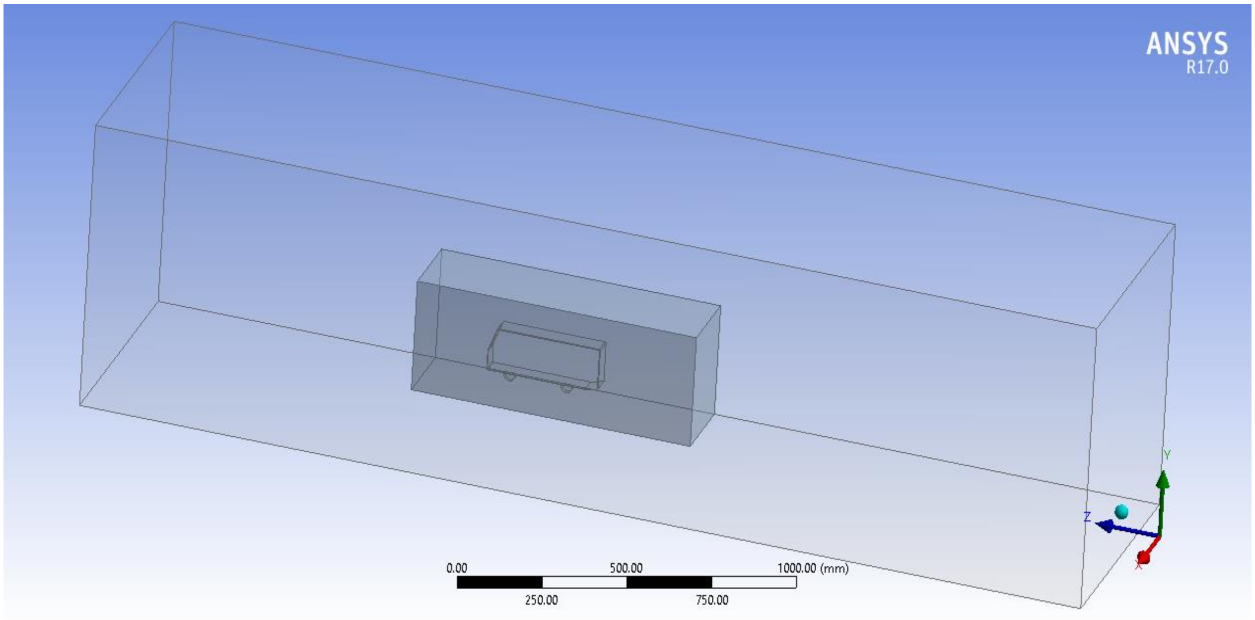

Figure B- 3: Model I inside the enclosure box

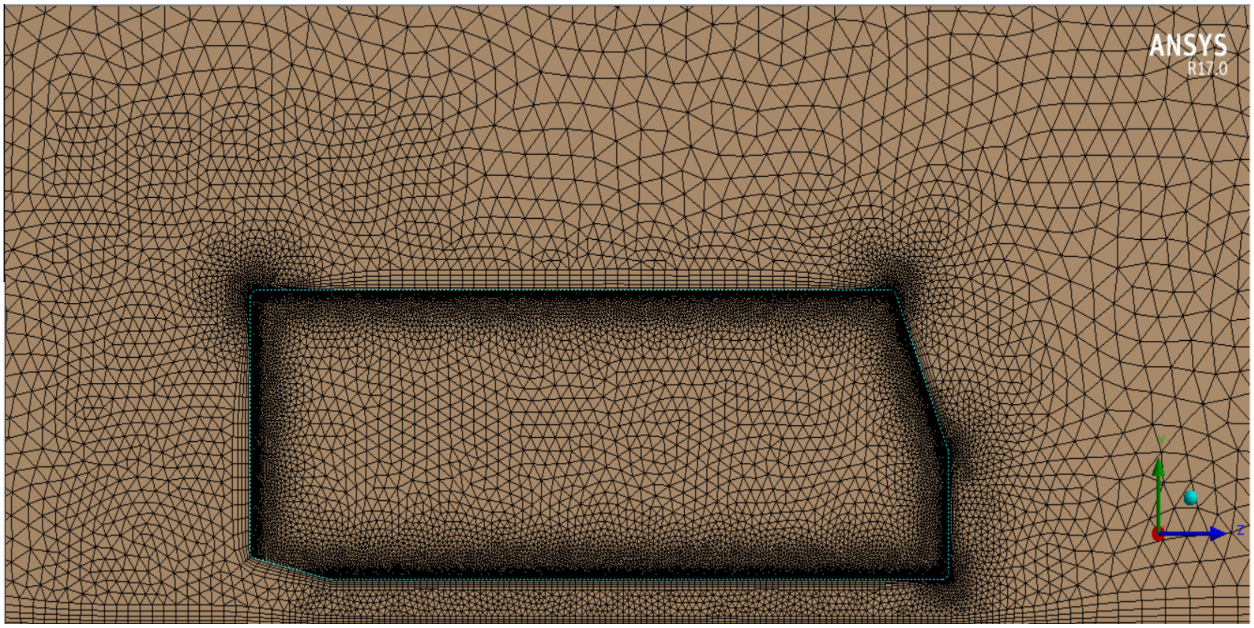

Figure B- 4: Model I after meshing

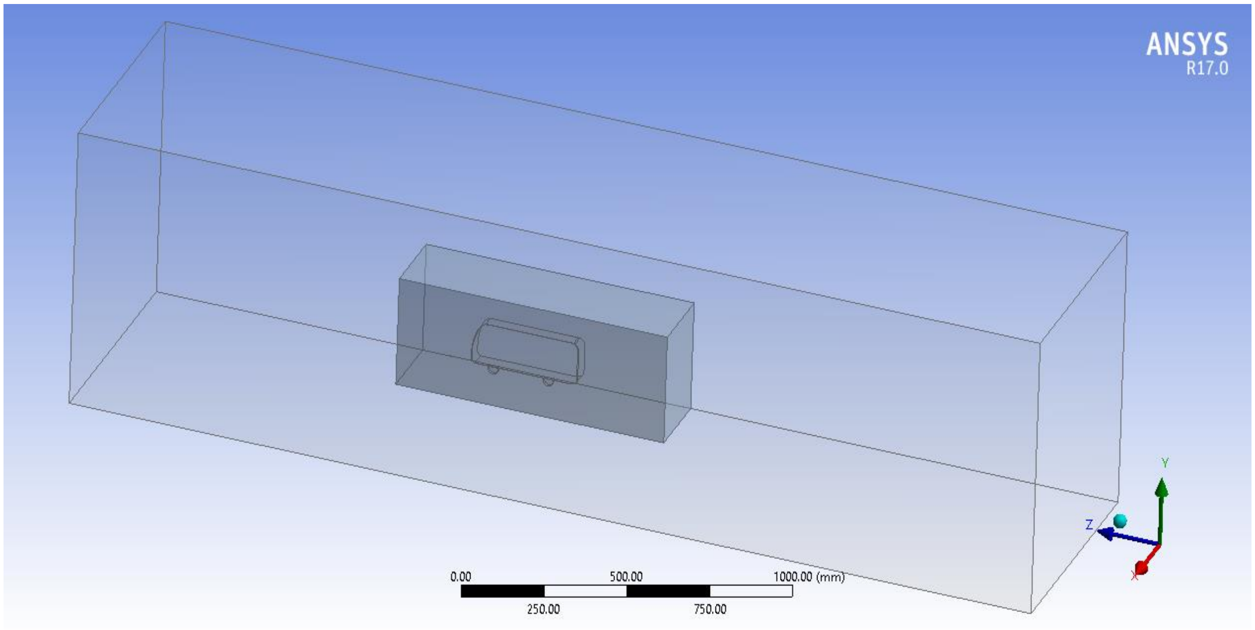

Figure B- 5: Model II inside the enclosure box

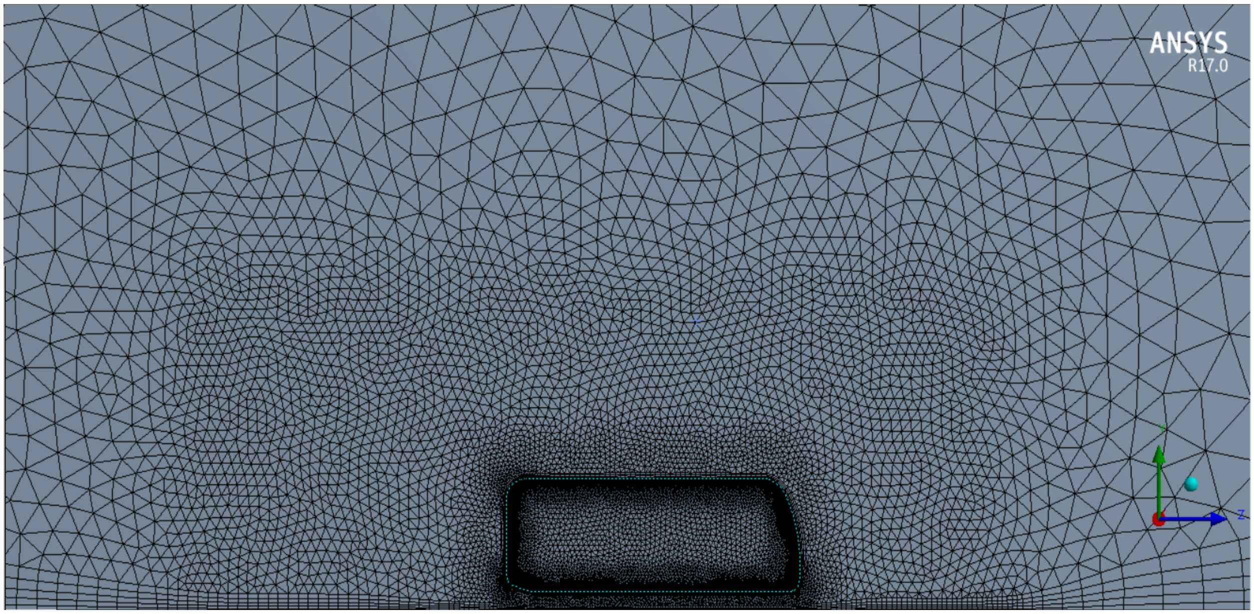

Figure B- 6: Model II after meshing

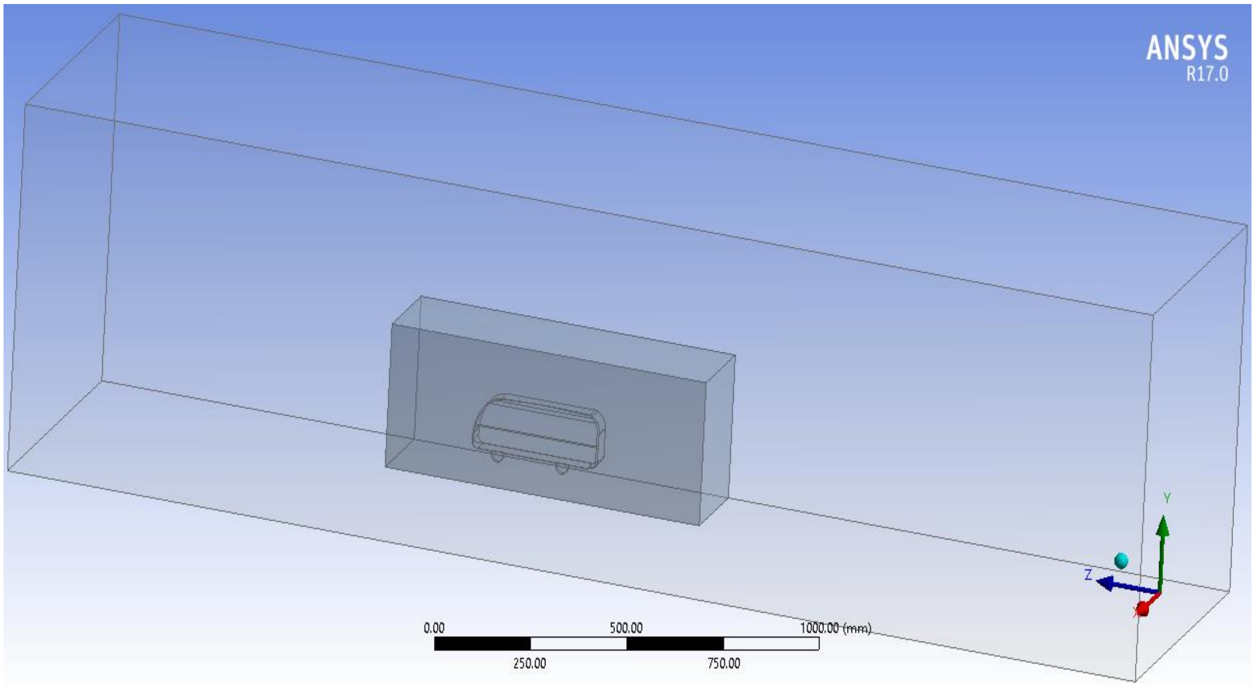

Figure B- 7: Model III inside the enclosure box

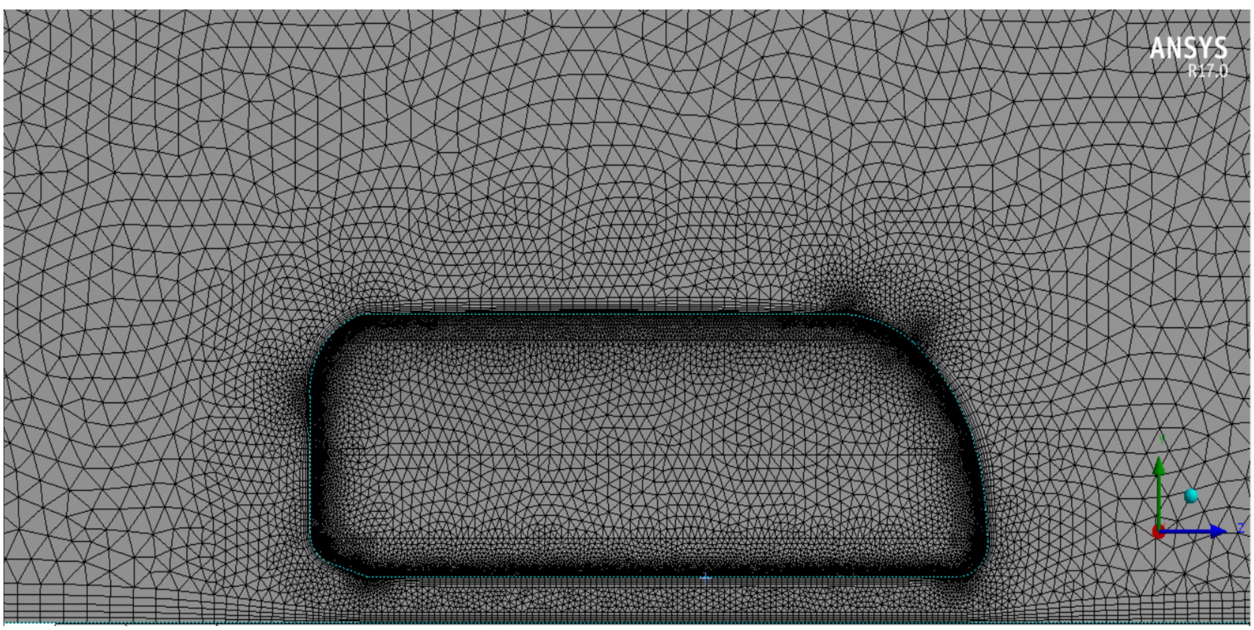

Figure B- 8: Model III after meshing

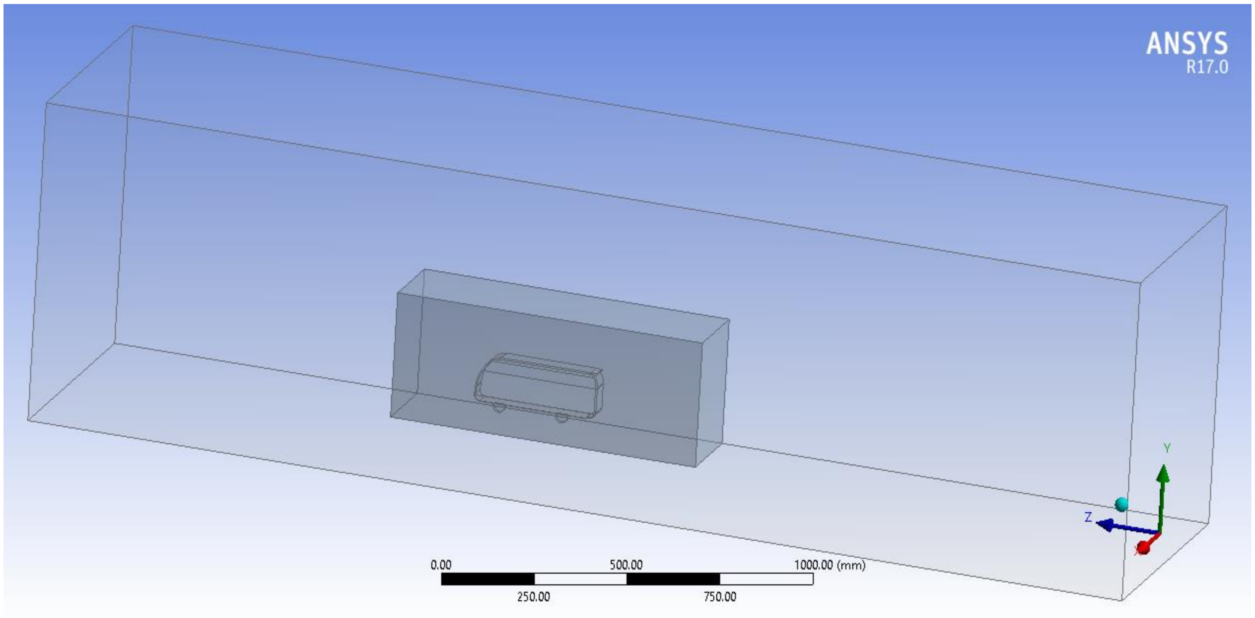

Figure B- 9: Model IV inside the enclosure box

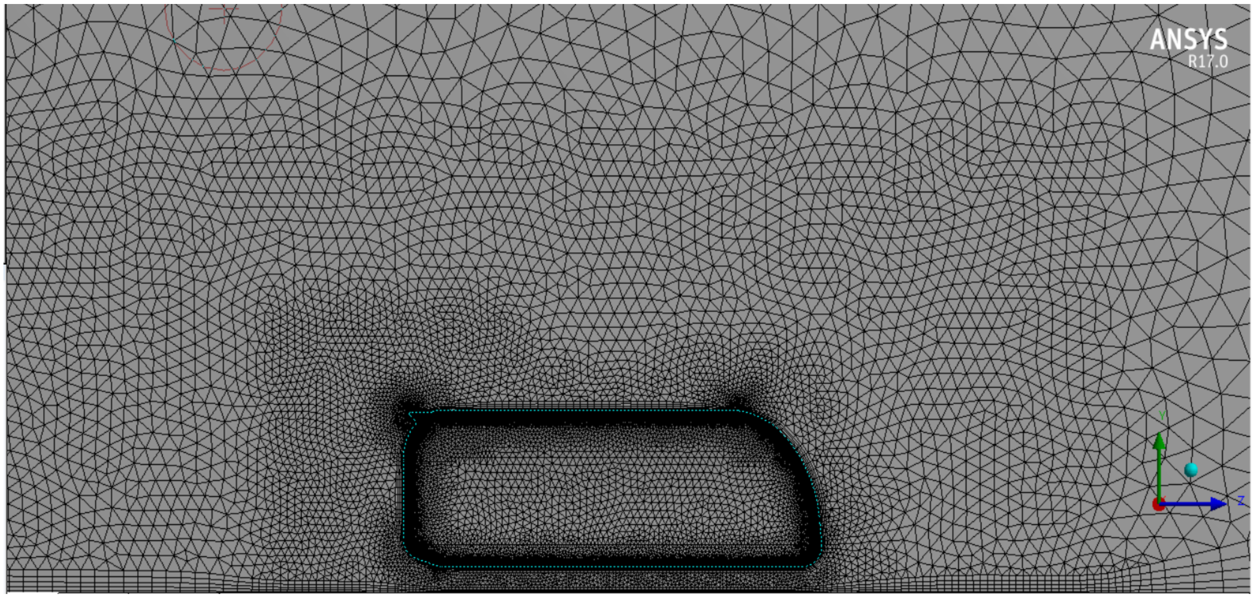

Figure B- 10: Model IV after meshing

Appendix C: Mesh Details

Table C- 1: Baseline Model Mesh Detail Element Size 8 mm

Object Name	*Mesh*
State	Solved
Display	
Display Style	Body Color
Defaults	
Physics Preference	CFD
Solver Preference	Fluent
Relevance	0
Export Format	Standard
Sizing	
Size Function	Proximity and Curvature
Relevance Center	Fine
Smoothing	High
Curvature Normal Angle	12.0 °
Num Cells Across Gap	5
Proximity Size Function Sources	Edges
Min Size	Default (0.753190 mm)
Proximity Min Size	Default (0.753190 mm)
Max Tet Size	Default (96.4090 mm)
Growth Rate	Default (1.20)
Minimum Edge Length	1.19190 mm
Inflation	
Use Automatic Inflation	Program Controlled
Inflation Option	Smooth Transition
Transition Ratio	0.272
Maximum Layers	5
Growth Rate	1.2
View Advanced Options	No
Assembly Meshing	
Method	Tetrahedrons
Feature Capture	Program Controlled
Tessellation Refinement	Program Controlled
Intersection Feature Creation	Program Controlled
Advanced	
Number of CPUs for Parallel Part Meshing	Program Controlled
Statistics	
Nodes	457386
Elements	2003496
Mesh Metric	None

Table C- 2: Baseline Model Mesh Detail Element Size 9 mm

Object Name	*Mesh*
State	Solved
Display	
Display Style	Body Color
Defaults	
Physics Preference	CFD
Solver Preference	Fluent
Relevance	0
Export Format	Standard
Sizing	
Size Function	Proximity and Curvature
Relevance Center	Fine
Smoothing	High
Curvature Normal Angle	12.0 °
Num Cells Across Gap	5
Proximity Size Function Sources	Edges
Min Size	Default (0.753190 mm)
Proximity Min Size	Default (0.753190 mm)
Max Tet Size	Default (96.4090 mm)
Growth Rate	Default (1.20)
Minimum Edge Length	1.19190 mm
Inflation	
Use Automatic Inflation	Program Controlled
Inflation Option	Smooth Transition
Transition Ratio	0.272
Maximum Layers	5
Growth Rate	1.2
View Advanced Options	No
Assembly Meshing	
Method	Tetrahedrons
Feature Capture	Program Controlled
Tessellation Refinement	Program Controlled
Intersection Feature Creation	Program Controlled
Advanced	
Number of CPUs for Parallel Part Meshing	Program Controlled
Statistics	
Nodes	400991
Elements	1673645
Mesh Metric	None

Table C- 3: Baseline Model Mesh Detail Element Size 10 mm

Object Name	*Mesh*
State	Solved
Display	
Display Style	Body Color
Defaults	
Physics Preference	CFD
Solver Preference	Fluent
Relevance	0
Export Format	Standard
Sizing	
Size Function	Proximity and Curvature
Relevance Center	Fine
Smoothing	High
Curvature Normal Angle	12.0 °
Num Cells Across Gap	5
Proximity Size Function Sources	Faces and Edges
Min Size	Default (0.753190 mm)
Proximity Min Size	Default (0.753190 mm)
Max Tet Size	Default (96.4090 mm)
Growth Rate	Default (1.20)
Minimum Edge Length	1.19190 mm
Inflation	
Use Automatic Inflation	Program Controlled
Inflation Option	Smooth Transition
Transition Ratio	0.272
Maximum Layers	5
Growth Rate	1.2
View Advanced Options	No
Assembly Meshing	
Method	Tetrahedrons
Feature Capture	Program Controlled
Tessellation Refinement	Program Controlled
Intersection Feature Creation	Program Controlled
Advanced	
Number of CPUs for Parallel Part Meshing	Program Controlled
Statistics	
Nodes	338621
Elements	1403239
Mesh Metric	None

Table C- 4: Baseline Model Mesh Detail Element Size 11 mm

Object Name	*Mesh*
State	Solved
Display	
Display Style	Body Color
Defaults	
Physics Preference	CFD
Solver Preference	Fluent
Relevance	0
Export Format	Standard
Sizing	
Size Function	Proximity and Curvature
Relevance Center	Fine
Smoothing	High
Curvature Normal Angle	12.0 °
Num Cells Across Gap	5
Proximity Size Function Sources	Edges
Min Size	Default (0.753190 mm)
Proximity Min Size	Default (0.753190 mm)
Max Tet Size	Default (96.4090 mm)
Growth Rate	Default (1.20)
Minimum Edge Length	1.19190 mm
Inflation	
Use Automatic Inflation	Program Controlled
Inflation Option	Smooth Transition
Transition Ratio	0.272
Maximum Layers	5
Growth Rate	1.2
View Advanced Options	No
Assembly Meshing	
Method	Tetrahedrons
Feature Capture	Program Controlled
Tessellation Refinement	Program Controlled
Intersection Feature Creation	Program Controlled
Advanced	
Number of CPUs for Parallel Part Meshing	Program Controlled
Statistics	
Nodes	309746
Elements	1245052
Mesh Metric	None

Table C- 5: Baseline Model Mesh Detail Element Size 12 mm

Object Name	*Mesh*
State	Solved
Display	
Display Style	Body Color
Defaults	
Physics Preference	CFD
Solver Preference	Fluent
Relevance	0
Export Format	Standard
Sizing	
Size Function	Proximity and Curvature
Relevance Center	Fine
Smoothing	High
Curvature Normal Angle	12.0 °
Num Cells Across Gap	5
Proximity Size Function Sources	Edges
Min Size	Default (0.753190 mm)
Proximity Min Size	Default (0.753190 mm)
Max Tet Size	Default (96.4090 mm)
Growth Rate	Default (1.20)
Minimum Edge Length	1.19190 mm
Inflation	
Use Automatic Inflation	Program Controlled
Inflation Option	Smooth Transition
Transition Ratio	0.272
Maximum Layers	5
Growth Rate	1.2
View Advanced Options	No
Assembly Meshing	
Method	Tetrahedrons
Feature Capture	Program Controlled
Tessellation Refinement	Program Controlled
Intersection Feature Creation	Program Controlled
Advanced	
Number of CPUs for Parallel Part Meshing	Program Controlled
Statistics	
Nodes	293078
Elements	1146716
Mesh Metric	None

Table C- 6: Model One Mesh Detail Element Size 10 mm

Object Name	*Mesh*
State	Solved
Display	
Display Style	Body Color
Defaults	
Physics Preference	CFD
Solver Preference	Fluent
Relevance	0
Export Format	Standard
Sizing	
Size Function	Proximity and Curvature
Relevance Center	Fine
Smoothing	High
Curvature Normal Angle	12.0 °
Num Cells Across Gap	5
Proximity Size Function Sources	Faces and Edges
Min Size	Default (0.75310 mm)
Proximity Min Size	Default (0.75310 mm)
Max Tet Size	Default (96.3970 mm)
Growth Rate	Default (1.20)
Minimum Edge Length	0.715530 mm
Inflation	
Use Automatic Inflation	Program Controlled
Inflation Option	First Aspect Ratio
First Aspect Ratio	5.
Maximum Layers	5
Growth Rate	1.2
View Advanced Options	No
Assembly Meshing	
Method	Tetrahedrons
Feature Capture	Program Controlled
Tessellation Refinement	Program Controlled
Intersection Feature Creation	Program Controlled
Advanced	
Number of CPUs for Parallel Part Meshing	Program Controlled
Statistics	
Nodes	442964
Elements	1791101
Mesh Metric	None

Table C- 7: Model Two Mesh Detail Element Size 10 mm

Object Name	*Mesh*
State	Solved
Display	
Display Style	Body Color
Defaults	
Physics Preference	CFD
Solver Preference	Fluent
Relevance	0
Export Format	Standard
Sizing	
Size Function	Proximity and Curvature
Relevance Center	Fine
Smoothing	High
Curvature Normal Angle	12.0 °
Num Cells Across Gap	5
Proximity Size Function Sources	Faces and Edges
Min Size	Default (0.752690 mm)
Proximity Min Size	Default (0.752690 mm)
Max Tet Size	Default (96.3440 mm)
Growth Rate	Default (1.20)
Minimum Edge Length	0.241660 mm
Inflation	
Use Automatic Inflation	Program Controlled
Inflation Option	First Aspect Ratio
First Aspect Ratio	5.
Maximum Layers	5
Growth Rate	1.2
View Advanced Options	No
Assembly Meshing	
Method	Tetrahedrons
Feature Capture	Program Controlled
Tessellation Refinement	Program Controlled
Intersection Feature Creation	Program Controlled
Advanced	
Number of CPUs for Parallel Part Meshing	Program Controlled
Statistics	
Nodes	371945
Elements	1477729
Mesh Metric	None

Table C- 8: Model Three Mesh Detail Element Size 10 mm

Object Name	*Mesh*
State	Solved
Display	
Display Style	Body Color
Defaults	
Physics Preference	CFD
Solver Preference	Fluent
Relevance	0
Export Format	Standard
Sizing	
Size Function	Proximity and Curvature
Relevance Center	Fine
Smoothing	High
Curvature Normal Angle	12.0 °
Num Cells Across Gap	5
Proximity Size Function Sources	Faces and Edges
Min Size	Default (0.752860 mm)
Proximity Min Size	Default (0.752860 mm)
Max Tet Size	Default (96.3660 mm)
Growth Rate	Default (1.20)
Minimum Edge Length	2.301e-002 mm
Inflation	
Use Automatic Inflation	Program Controlled
Inflation Option	First Aspect Ratio
First Aspect Ratio	5.
Maximum Layers	5
Growth Rate	1.2
View Advanced Options	No
Assembly Meshing	
Method	Tetrahedrons
Feature Capture	Program Controlled
Tessellation Refinement	Program Controlled
Intersection Feature Creation	Program Controlled
Advanced	
Number of CPUs for Parallel Part Meshing	Program Controlled
Statistics	
Nodes	397867
Elements	1578266
Mesh Metric	None

Table C- 9: Model Four Mesh Detail Element Size 10 mm

Object Name	*Mesh*
State	Solved
Display	
Display Style	Body Color
Defaults	
Physics Preference	CFD
Solver Preference	Fluent
Relevance	0
Export Format	Standard
Sizing	
Size Function	Proximity and Curvature
Relevance Center	Fine
Smoothing	High
Curvature Normal Angle	12.0 °
Num Cells Across Gap	5
Proximity Size Function Sources	Faces and Edges
Min Size	Default (0.752790 mm)
Proximity Min Size	Default (0.752790 mm)
Max Tet Size	Default (96.3570 mm)
Growth Rate	Default (1.20)
Minimum Edge Length	5.1325e-003 mm
Inflation	
Use Automatic Inflation	Program Controlled
Inflation Option	First Aspect Ratio
First Aspect Ratio	5.
Maximum Layers	5
Growth Rate	1.2
View Advanced Options	No
Assembly Meshing	
Method	Tetrahedrons
Feature Capture	Program Controlled
Tessellation Refinement	Program Controlled
Intersection Feature Creation	Program Controlled
Advanced	
Number of CPUs for Parallel Part Meshing	Program Controlled
Statistics	
Nodes	459272
Elements	1938500
Mesh Metric	None